Title
High-Z Nanoparticle/Polymer Nanocomposites for Gamma-Ray Scintillation Detectors

Author
Liu, Chao

Publication Date
2017

Peer reviewed|Thesis/dissertation

UNIVERSITY OF CALIFORNIA

Los Angeles

High-Z Nanoparticle/Polymer Nanocomposites for Gamma-Ray Scintillation Detectors

A dissertation submitted in partial satisfaction of the requirements for the degree Doctor of Philosophy in Materials Science and Engineering

by

Chao Liu

2017

ABSTRACT OF THE DISSERTATION

High-Z Nanoparticle/Polymer Nanocomposites

for Gamma-Ray Scintillation Detectors

by

Chao Liu

Doctor of Philosophy in Materials Science and Engineering

University of California, Los Angeles, 2017

Professor Qibing Pei, Chair

An affordable and reliable solution for spectroscopic gamma-ray detection has long been sought after due to the needs from research, defense, and medical applications. Scintillators resolve γ energy by proportionally converting a single high-energy photon into a number of photomultiplier-tube-detectable low-energy photons, which is considered a more affordable solution for general purposes compared to the delicate semiconductor detectors. An ideal scintillator should simultaneously exhibit the following characteristics: 1) high atomic number (**Z**) for high gamma stopping power and photoelectron production; 2) high light yield since the energy resolution is inversely proportional to the square root of light yield; 3) short emission decay lifetime; and 4) low cost and scalable production. However, commercial scintillators made from either inorganic single crystals or plastics fail to satisfy all requirements due to their intrinsic material properties and fabrication limitations.

The concept of adding high-Z constituents into plastic scintillators to harness high Z, low cost, and fast emission in the resulting nanocomposite scintillators is not new in and of itself. Attempts have been made by adding organometallics, quantum dots, and scintillation nanocrystals into the plastic matrix. High-Z organometallics have long been used to improve the Z of plastic scintillators; however, their strong spin-orbit coupling effect entails careful triplet energy matching using expensive triplet emitters to avoid severe quenching of the light yield. On the other hand, reported quantum dot- and nanocrystal-polymer nanocomposites suffer from moderate Z and high optical loss due to aggregation and self-absorption at loadings higher than 10 wt%, limiting their potential for practical application.

This dissertation strives to improve the performance of nanoparticle-based nanocomposite scintillators. One focus is to synthesize transparent nanocomposites with higher loadings of high-Z inorganic nanoparticles. A facile single-precursor method is first developed to synthesize HfO_2 nanoparticles, the highest-Z simple oxide with band gap larger than polyvinyltoluene, with uniform size distribution around 5 nm. A nanoparticle-surface-modification protocol is then developed for the fabrication of transparent nanocomposite monoliths with high nanoparticle loadings (up to 40 wt%). Using this method, transparent HfO_2-loaded blue-emitting nanocomposite scintillators (2 mm thick, transmittance at 550 nm >75%) have been fabricated capable of producing a full energy photopeak for 662 keV gamma rays, with the best deconvoluted photopeak energy resolution < 8%, representing a significant improvement over previous nanoparticle-based nanocomposite scintillators.

Although the HfO_2 work represents a great improvement over previous reports, it is also found in this system that the light yield deteriorates at higher nanoparticle loadings. This is attributed to the trapping of fast electron energy deposited in the non-emitting nanoparticles. To overcome this deterioration issue, a revisit to the previously proposed quantum-dot-loaded nanocomposite scintillator is made with significant improvements. Transparent, ultra-high-loading (up to 60 wt%) $Cd_xZn_{1-x}S/ZnS$ core/shell quantum dot/polymer nanocomposite monoliths are first synthesized by in situ copolymerization of the partially mathacrylate-functionalized quantum dots in a monomer solution. With efficient Förster resonance energy transfer from the high-atomic-number quantum dots to lower-band-gap organic dyes, quantum-dot-borne excitons are extracted for photon production. The resulting nanocomposites thus exhibit unprecedented simultaneous enhancements in both light yield (visible photons produced per MeV of gamma photon energy) and gamma attenuation power. In a best demonstration, a 60 wt% quantum-dot nanocomposite scintillator exhibits a light yield of 9255 photons/MeV and a photopeak resolution of 9.8% under 662 keV Cs-137 gamma irradiation, demonstrating the potential of this model system for future high-performance low-cost spectroscopic gamma detectors.

The dissertation of Chao Liu is approved.

Yang Yang

Yunfeng Lu

Yong Chen

Qibing Pei, Committee Chair

University of California, Los Angeles

2017

Dedicated to my parents
for their unconditional love and support

Table of Contents

List of Figures and Tables

Acknowledgements

First and foremost, I would like to express my sincere gratitude to my advisor, Professor Qibing Pei, for his guidance and generous support over the past five years. The completion of this dissertation would not be possible without his insight and mentorship.

I would also like to thank Professor Yang Yang, Professor Yong Chen, and Professor Yunfeng Lu for serving on my committee. Their instruction and guidance are indispensable for the completion of this dissertation.

I am grateful for the help received from past and current Pei lab members. To my fellow Rm. 2021N occupants, Tibor Jacob Hajagos, David Kishpaugh, Dr. Yi Chen, and Zhou Li – I will miss the moments doing synthesis with you guys. I would also like to extend my gratitude to Dr. Jiajie Liang, Dr. Lu Li, Dr. Chaokun Gong, Dr. Xiaofan Niu, Dr. Haizheng Zhong, Dr. Fangchao Zhao, and Dr. Xiaofeng Liu for their discussion and help during my PhD.

From other research groups and facilities, I am indebted to Dr. Noah Bodzin of the UCLA Nanolab, Dr. Ignacio Martini, Dr. Saeed Khan, and Dr. Xin Cong from the UCLA Molecular Instrumentation Center, Dr. Sergey Prikhodko from the Materials Science department, Dr. Ivo Atanasov of the Electron Imaging Center for Nanomachines, and Dr. Stephen Payne and Dr.

Nerine Cherepy from the Lawrence Livermore National Laboratory for their generous help and guidance.

The following institutions/programs are acknowledged for providing financial supports for the projects involved in this dissertation: the Defense Threat Reduction Agency (HDTRA1-14-0032), National Science Foundation (ECCS-1348403), and the University of California Lab Fees Research Program (UCOP Grant 12-LR-237678). I would also like to acknowledge the use of instruments at the Electron Imaging Center for NanoMachines supported by NIH (1S10RR23057 to ZHZ) and CNSI at UCLA. Chapter Two is reprinted (adapted) with permission from *Liu, C.; Hajagos, T. J.; Kishpaugh, D.; Jin, Y.; Hu, W.; Chen, Q.; Pei, Q. Facile single-precursor synthesis and surface modification of HfO_2 nanoparticles for nanocomposite γ ray scintillators. Adv. Funct. Mater., 2015(25): 4607-4616.* Copyright 2015, John Wiley & Sons. Chapter Three is reprinted (adapted) with permission from *Liu, C.; Hajagos, T. J.; Chen, D.; Chen, Y.; Kishpaugh, D.; Pei, Q. Efficient one-pot synthesis of colloidal zirconium oxide nanoparticles for high refractive index nanocomposites. ACS Appl. Mater. Interfaces, 2016(8): 4795-4802*. Copyright 2016, American Chemical Society. Chapter Four is a version of *Liu, C.; Li, Z.; Hajagos, T. J.; Kishpaugh, D.; Chen, D.; Pei, Q. Transparent ultra-high-loading quantum dot/polymer nanocomposite monolith for gamma scintillatio*n. *Submitted for publication*. Prof. Qibing Pei is the director for all projects involved in these segments.

Special thanks are dedicated to Dr. Qi Chen, Dr. Huanping Zhou, Dr. Wei Hu, Huier Gao, Dr. Zhi Ren, Dr. Yongjia Li, Enbo Zhu, Dr. Dustin Chen, Kwing Tong, Suki Zhang, Charlotte Chou, and Song Luo – thanks guys, UCLA would have meant so much less without you.

To Q.T. – many, many thanks for your understanding and company. You are the best.

And finally to my parents – words can't express my gratitude for your unfaltering love. Thank you.

Vita

2012 B.S., Macromolecular Materials and Engineering, Fudan University, Shanghai, China

2013 M.S., Materials Science and Engineering, University of California, Los Angeles, Los Angeles, CA

2016 Summer Consultant, The Boston Consulting Group, Shanghai, China

SELECTED PUBLICATIONS (6 out of 12)

[1] **Liu, C.**; Li, Z.; Hajagos, T. J.; Kishpaugh, D.; Chen, D.; Pei, Q.* Transparent ultra-high-loading quantum dot/polymer nanocomposite monolith for gamma scintillation. Submitted for publication.

[2] **Liu, C.**; Hajagos, T. J.; Chen, D.; Chen, Y.; Kishpaugh, D.; Pei, Q.* Efficient one-pot synthesis of colloidal zirconium oxide nanoparticles for high refractive index nanocomposites. ***ACS Appl. Mater. Interfaces***, 2016(**8**): 4795.

[3] **Liu, C.**; Hajagos, T. J.; Kishpaugh, D.; Jin, Y.; Hu, W.; Chen, Q.; Pei, Q.* Synthesis of transparent nanocomposite monoliths for gamma scintillation. ***Proc. SPIE***, DOI:10.1117/12.2189664.

[4] **Liu, C.**; Hajagos, T. J.; Kishpaugh, D.; Jin, Y.; Hu, W.; Chen, Q.; Pei, Q.* Facile single-precursor synthesis and surface modification of HfO_2 nanoparticles for nanocomposite γ ray scintillators. ***Adv. Funct. Mater.***, 2015(**25**): 4607.

[5] **Liu, C.**; Guo, W.; Zhao, F.; Sun, X.; Yang, Z.; Chen, T.; Chen, X.; Qiu, L.; Hu, X.; Peng, H.* A Novel Electromechanical Actuation Mechanism of a Carbon Nanotube Fiber. ***Adv. Mater.***, 2012(**24**): 5739. (Co-First Author)

[6] Chen, Y.; **Liu, C.**; Jin, Y.; Hajagos, T. J.; Kishpaugh, D.; Zhuang, Q.; Pei, Q.* Ytterbium fluoride loaded plastic scintillators for γ-ray spectroscopy. ***Proc. SPIE***, DOI:10.1117/12.2238336.

PATENT

[1] Peng, H.; Guo, W.; **Liu, C.**; Sun, X.; Yang, Z. Oriented carbon nanotube/macromolecular composite fibers and preparation method thereof. CN102220696B. Granted.

CONFERENCE PRESENTATIONS

[1] Ytterbium fluoride loaded plastic scintillators for γ-ray spectroscopy. Oral presentation at SPIE Optics and Photonics 2016, San Diego, CA, August 28 – September 1, 2016.

[2] Facile synthesis and surface modification of HfO_2 nanoparticles for nanocomposite γ-ray scintillators. Oral presentation at the 250th American Chemical Society National Meeting & Exposition, Boston, MA, August 16-20, 2015.

Chapter 1. Introduction

1.1 Background on gamma ray

The discovery of gamma (**γ**) radiation dates back to the year of 1900 when Paul Villard, a French chemist and physicist, was studying the radiation from radium. This highly penetrating, extremely high-energy radiation was named *gamma ray* by Ernest Rutherford in 1903, following his previous discovery of *alpha* (He^{2+}) and *beta* (high speed electron or positron from radioactive decay of an atomic nucleus) rays. Albeit being named after the charged high-energy particles of alpha and beta, in its nature, γ ray actually has more in common with x-ray, another high-energy, highly penetrating electromagnetic radiation.[1] Previously the distinction between γ and x-ray had been based on the energy differences of the two, as γ ray was long considered having a higher energy than x-ray.[1,2] However, recent advances in synchrotron and accelerator technologies facilitate the production of x-rays with extremely high energy (4-25 MeV), whose energy can be even higher than that of γ ray (100 keV – 10 MeV) produced by the decay of radioactive isotopes.[1] Therefore, nowadays the distinction between γ ray and x-ray are mostly drawn based on their origins, where x-ray is produced by the change of electron energy, and gamma ray is produced by the change of nucleus energy or by other particle decay and annihilation events.[1] It should be noted that in astronomy, gamma ray and x-ray is still distinguished based on the energy, since events such as a supernova burst produce "γ ray" of energy higher than that can be achieved via radioactive decay.[3]

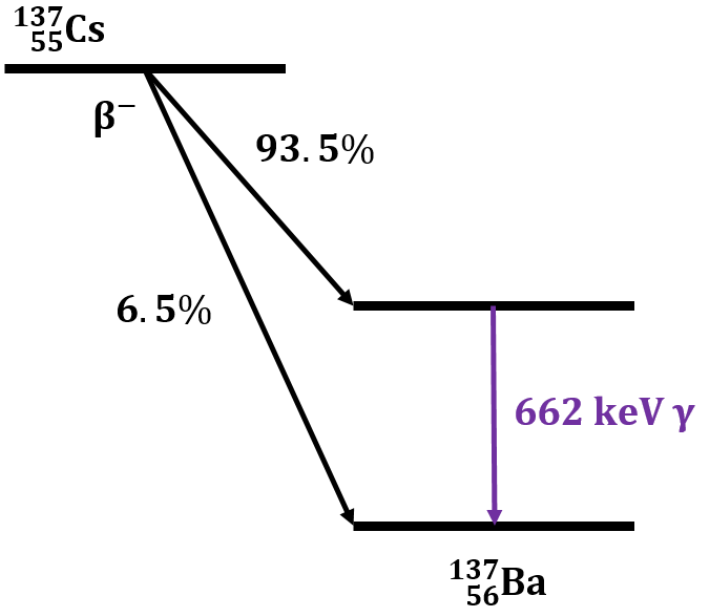

Figure 1.1 Decay scheme of Cs-137, a commonly used gamma source.

The most common source of γ ray is the radiative decay of an excited nucleus which is often a product of other processes such as nuclear reactions (nuclear fission, nuclear fusion, and neutron capture), and alpha or beta decay of a parent radionuclide.[1] **Figure 1.1** shows an example of Cs-137, a commonly used gamma source with a half-life of 30.17 years, producing a γ photon of 662 keV energy following its beta decay. The half-life of 30.17 years comes mainly from the low beta decay rate of the relatively stable Cs-137, since the excited state of the daughter Ba-137 is much more unstable (with a half-life of picoseconds or less) and quickly de-excites through the emission of a γ photon. Energy of the γ photon is then determined by the energy difference between the initial and final nuclear states. Due to the well-defined energies of nuclear states, the gamma photons emitted via such inter-state transition have energy specific to the nucleus in excited states, and can often also be treated as nearly mono-energetic due to their small line widths (except for the case when the nucleus has high velocity, where Doppler effect may cause line broadening). In

addition, the energy differences between nuclear states are much greater than the electron states, which explains why typical γ photons have higher energies than x-rays.

Besides the decay of radionuclides, another important source of gamma ray is via annihilation reaction, where a positron and an electron annihilate to produce a pair of oppositely directed γ photons each with 511 keV energy. The positron-electron annihilation is in fact a reversed process of pair-production, a form of interaction between high-energy gamma and matter, which will be discussed in detail in the following section.

The high-energy γ photons have numerous applications in areas such as astrophysics, high-energy physics, industrial sensing, sterilization, medical treatment, biomedical imaging, and in the promotion of nuclear non-proliferation.[1–7] For example, the detection of gamma rays with space telescopes such as the Fermi Gamma-ray Space Telescope provides information of astronomical objects such as pulsar, quasar, neutron star, and black hole.[8] Moreover, not only a subject for study in particle physics, γ rays are also used to calibrate and test detectors used in the high-energy physics facilities. Furthermore, the highly penetrating nature of γ photons is utilized for the detection of construction defects in industry. Unlike neutron, objects irradiated by γ photons do not become radioactive. Therefore, high-energy γ ray is also widely used to sterilize food and medical equipment.[6] With a similar idea, concentrated γ photons aimed from different angles are also used in cancer therapy under a well-known name of gamma-knife surgery.[7] In another aspect, by utilizing radioisotope-labeled reagents which emit γ photons or positrons, γ rays are also used in bio-imaging and diagnostics techniques such as positron emission tomography (known as PET) and single-photon emission computed tomography (known as SPECT).[4] As a final example, the

combination of γ photon's radionuclide-specific nature and great penetrating capability renders it a perfect target to be focused on when searching for potential nuclear threats for homeland security purposes.

All these applications cannot be implemented without an efficient γ detector. Moreover, many of the mentioned applications require not only detection of the presence of γ photons, but also information about the γ photon's energy. For this reason, the development of efficient detectors for γ photon spectroscopy has always been an important topic in the nuclear engineering community.[1,2,9–11] To date, several kinds of detectors have been developed for the spectroscopic detection of γ photons, each with its own advantages and disadvantages. The following sections will elaborate on the characteristics of these detectors, with special focus on the development of conventional and novel nanocomposite γ scintillators, which is deemed the focus of research for this dissertation due to the recent advancements in nanotechnology.

1.2 Gamma-matter interaction

Before diving into the subject of γ photon detection, it is necessary to first cover some background on the interactions between γ photons and matter. In addition, since all γ-matter interactions involve fast electron as a major product, the second portion of this section is devoted to the interactions between fast electron and matters.

1.2.1 Gamma-matter interaction

Although a large number of possible mechanisms are already known for γ photons to interact with matter, for detection purposes the interaction between γ photons and matter has to involve some

sort of energy exchange. There are three major types of interactions that involve γ-matter energy exchange: *photoelectric absorption, Compton scattering, and pair production*, which will be elaborated in the following discussion.

1.2.1.1. Photoelectric absorption

The photoelectric absorption is one of the most general and important mechanism for interactions between an electromagnetic wave and matter, which also led to the Nobel Prize in Physics awarded to Albert Einstein in 1921. As a kind of electromagnetic waves, γ rays show no difference in interacting with matter through the photoelectric effect. As illustrated in **Figure 1.2a**, in a photoelectric absorption process, a γ photon interacts with an atom and disappears, where an electron is given all energy of the γ photon and becomes capable of overcoming the binding energy from the nucleus. The powerful *photoelectron* is then ejected from the atom with an energy of:

$$E_{photoelectron} = E_{\gamma} - E_{binding} \tag{1.1}$$

where $E_{photoelectron}$, E_{γ}, and $E_{binding}$ denote the photoelectron energy, incident γ photon energy, and binding energy of the photoelectron, respectively. It should be noted that the photoelectric absorption is an "all or none" process, meaning that the γ photon must transfer all its energy to the creation of a single photoelectron. Therefore, photoelectric absorption is the most desired γ-matter interaction mode for the detection of full energy of the incident γ photon. For γ photons with sufficient energy to overcome the required binding energy, the most probable source of photoelectron is the inner-most K shell electrons of the atom. Therefore, following the ejection of photoelectron, the vacancy in K shell will be quickly filled by an electron from the outer shells, resulting in the production of a characteristic K-shell x-ray (**Figure 1.2b**) or Auger electron, with Kα x-ray being the dominant product. For high-Z absorbers, the characteristic Kα x-ray can be as

powerful as 50-70 keV. Since elements have significantly weakened capability of absorbing their own Kα x-rays (known as the *x-ray absorption edge*), the high-energy characteristic x-ray often escapes detectors with limited volumes, resulting in the detection of an *escape peak* whose energy is lower than the full incident γ energy by the gap of Kα x-ray energy. In contrast, when the energy in both photoelectron and the Kα x-ray is absorbed by the detector, the detection of a *photopeak* which represents the full energy of the incident γ photon is facilitated.

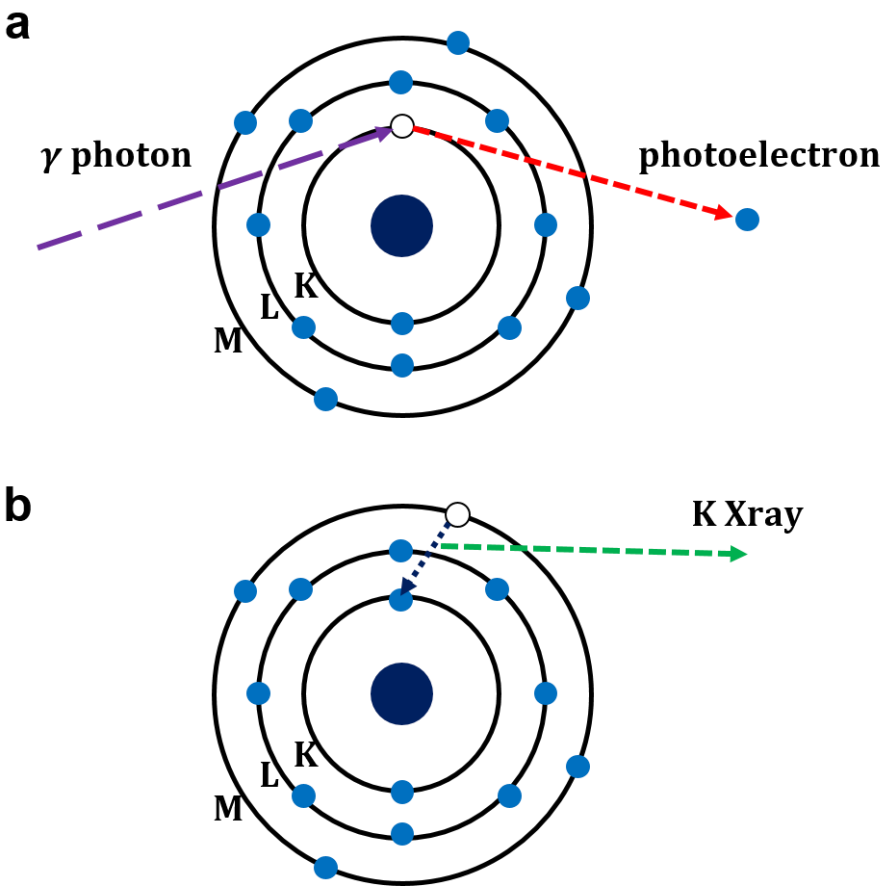

Figure 1.2 Schematic illustration of the photoelectric absorption process (**a**) and the production of K x-ray (**b**).

The photoelectric absorption is the dominating interaction mechanism for γ photons with relatively low energies (a few hundred keV). Increasing Z of the absorber has been shown to increase the

photoelectric absorption cross-section significantly. A rough estimation exists for the cross-section of photoelectric absorption ($\sigma_{photoelectric}$):[1]

$$\sigma_{photoelectric} \propto \frac{Z^n}{E_\gamma^{3.5}} \tag{1.2}$$

where n is a constant varying between 4 to 5. As a result of this strong dependence of Z, a major goal in developing spectroscopic γ detectors is to improve their Z.

1.2.1.2 Compton scattering

Another important mechanism of γ-matter interaction is the Compton scattering of γ photons. As shown in **Figure 1.3**, the incident γ photon is inelastically scattered by an electron in the absorbing material. The scattered γ photon transfers part of its energy to the electron and is deflected from its original path due to conservation of momentum. The electron originally at rest is given momentum and becomes a *recoil electron*. For Compton scattered γ photons, the energy detected by the detector is essentially the portion transferred to the recoil electron, if no other process with energy deposition takes place.

Energy of the recoil electron can be derived by solving simple equations obeying the conservation of energy and momentum. Using the symbols defined in **Figure 1.3**, the relationship between the recoil electron's energy ($E_{Compton\ electron}$) and scattering angle of the γ photon (θ) can be derived as:

$$E_{Compton\ electron} = E_\gamma \times \left[1 - \frac{1}{1 + \frac{E_\gamma}{m_0 c^2}(1 - \cos\theta)}\right] \tag{1.3}$$

where m_0c^2 and E_γ are the rest-mass energy of an electron (0.511 MeV), and energy of the incident γ photon, respectively. It can be seen that for incident γ photons with a fixed energy, the energy

deposited in the material via Compton scattering is only determined by the scattering angle of the γ photon. In addition, the highest energy that can be deposited via Compton scattering (in a 180° scattering) is characteristic of the incident γ photon's energy.

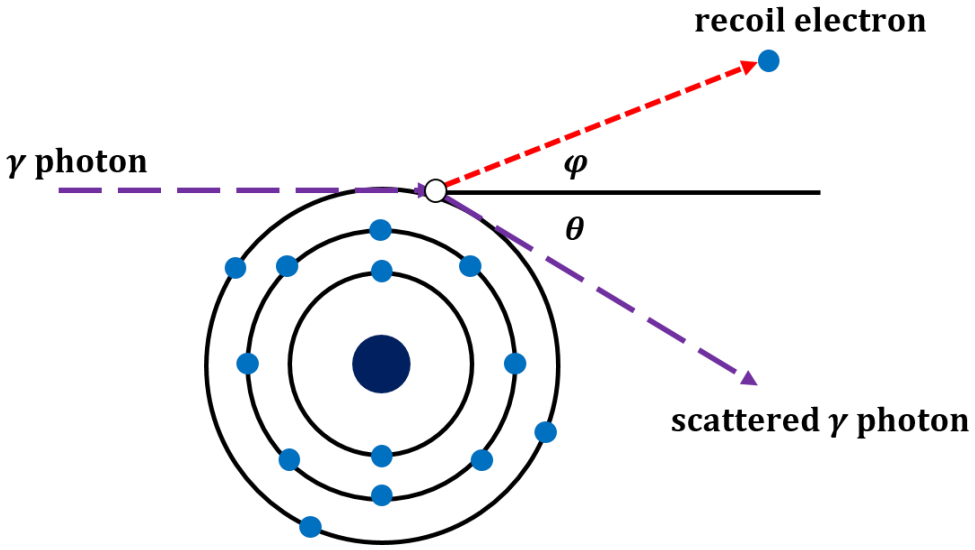

Figure 1.3 Schematic illustration of a Compton scattering process.

The probability of Compton scattering per absorbing atom depends on the number of electrons in the absorber and therefore increases linearly with Z. For materials with low-Z and γ photons with medium energy, Compton scattering is the dominant γ-matter interaction route. If the detector is large enough, the incident γ photon can go through multiple Compton scatters and finally be fully absorbed, essentially producing the same result as the photoelectric absorption. However, for detectors with limited volume and small photoelectric cross-section, single Compton scattering dominates, and the scattered photon often escapes the detector. As a result, the detected energy profile is a continuum from 0 to the highest recoil electron energy (**Figure 1.4**). This continuum, called the *Compton continuum*, usually decreases sharply to zero at the highest recoil electron energy, creating a *Compton edge*. The Compton edge is a useful feature in calibrating low-Z

detectors whose photoelectric cross-section is too low to produce a significant photopeak, since the Compton edge energy is fixed when the energy of the calibrating γ source is known.

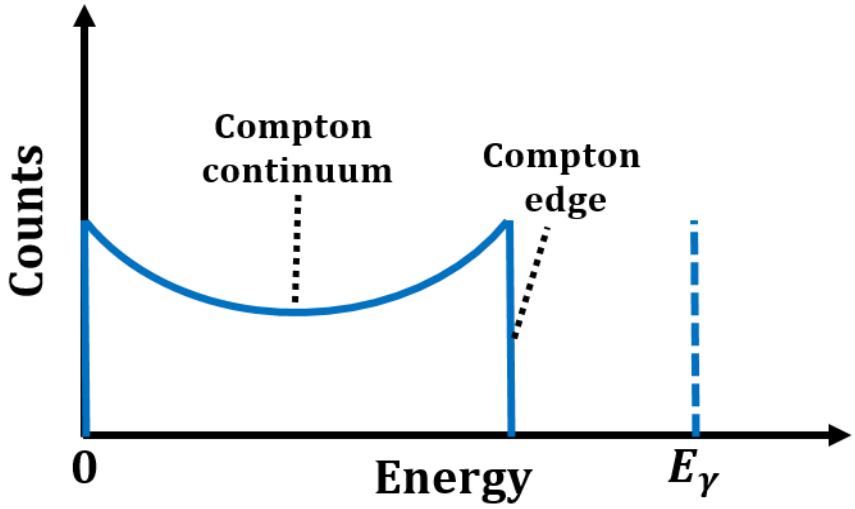

Figure 1.4 Schematic illustration of the Compton continuum and Compton edge detected by a low-Z detector, where no full γ photon energy can be resolved.

1.2.1.3 Pair production

When the γ photon's energy is larger than 1.02 MeV, twice of the rest-mass energy of an electron, a third type of γ-matter interaction comes into play. The process of *pair production* refers to the creation of an electron-positron pair by a γ photon in proximity to a nucleus. As shown in **Figure 1.5**, the γ photon disappears in the strong electric field created by the nucleus, with its energy being used to create the particles with a total rest-mass energy of 1.02 MeV. Any γ photon energy in excess of this amount is converted into kinetic energy shared by the pair. The electron and positron then deposit their kinetic energy on their path, as will be discussed in the next section. However, as the positron loses its kinetic energy, it will annihilate with an electron to produce two annihilation γ photons with 511 keV energy each. These annihilation photons will then go through other processes as mentioned before to deposit their energy in the medium. However, it is also

possible that either one or both of the two 511 keV photons escape the detector, resulting in the detection of a single (511 keV lower than incident γ energy) or double escape peak (1.02 MeV lower than incident γ energy), respectively.

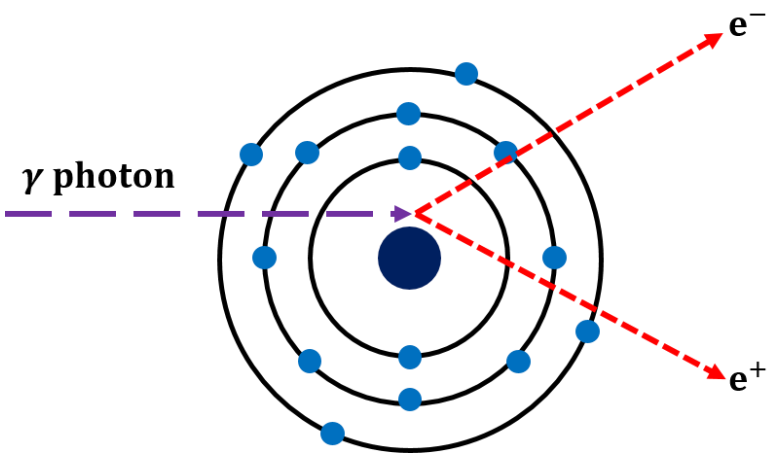

Figure 1.5 Schematic illustration of a pair production process.

The possibility of pair production varies roughly as Z^2 and increases significantly with the incident γ photon's energy. Therefore, it is the dominant interaction mode in the high-energy region.

1.2.2 Fast electron-matter interaction

As discussed before, fast electrons are the main product of all major γ-matter interactions that involve energy exchanges. Since fast electrons carries most of the converted γ photon energy, the detection of γ photon energy is essentially further converting the energy carried by fast electrons into readable signals, i.e. lower energy charge carriers or photons. Therefore, it is essential to develop a solid understanding of the interactions between fast electron and matter.

Unlike a gamma photon which tends to deposit its energy in a sudden and abrupt manner with only one atom or electron, charged particles such as the fast electron deposit their energy in a much

more continuous way with numerous atoms on its trajectory. The strong Coulomb interaction between fast electron and the orbital electrons resting in the material slows the fast electron continuously, while the kinetic energy of the fast electron can be either deposited in the electrons it has "collided" with on its path, or be converted into electromagnetic waves via radiative routes. The collisional energy deposition of a fast electron can be divided into two ways: *ionization* and *excitation*. Ionization happens when a fast electron deposit a large amount of kinetic energy in an orbital electron, resulting in the production of an ion as the orbital electron is ejected as a secondary electron. In cases when the secondary electron has enough energy to induce more ionizations on its own path, the secondary electron is named a *δ ray*. In addition, incident fast electrons with high energy often interact most strongly with K-orbital electrons, whose ejection is most likely followed by the production of a Kα x-ray. On the other hand, excitation happens when the orbital electron only receives a limited amount of energy to be excited to a higher energy level, where the excited electron is still bound to the atom or molecule. This creates an electron-hole pair bound by Coulomb attraction, i.e. an *exciton*. The specific energy loss of fast electrons due to collisional energy exchange ($-(dE/dx)_c$) is derived by Bethe as:[1]

$$-\left(\frac{dE}{dx}\right)_c = \frac{2\pi e^4 NZ}{m_0 v^2}\left(\ln\frac{m_0 v^2 E}{2I^2(1-\beta^2)} - (\ln 2)\left(2\sqrt{1-\beta^2} - 1 + \beta^2\right) + (1-\beta^2) + \frac{1}{8}\left(1-\sqrt{1-\beta^2}\right)^2\right) \quad (1.4)$$

where N, m_0, v, and I are the number density of the absorber atom, rest mass of electron, velocity of fast electron, and the average excitation and ionization potential of the absorber, respectively, whereas $\beta \equiv v/c$ with c being the speed of light.

When the fast electron is decelerated by Coulomb interactions in the medium, its lost kinetic energy can also be converted into electromagnetic waves called *Bremsstrahlung*. In contrast to the characteristic x-rays, Bremsstrahlung does not have a specific energy but represents a continuum in spectrum. Its generation can take place anywhere on the fast electron's trajectory. Low-energy Bremsstrahlung is reabsorbed by the medium with new fast electrons or excitons being produced. However, like characteristic x-rays, high energy Bremsstrahlung can also escape small detectors and thus influence their response.

The similar mass between a fast electron and orbital electron means that the fast electron is continuously deflected as it moves through the medium. In addition to the effect from Coulomb deceleration which produces Bremsstrahlung, a fast electron shall experience numerous deflections and have an overall tortuous path in matter. Typical range of a fast electron, which is defined as the thickness of matter required to reduce transmission of a fast electron to zero, is around 2 mm per MeV of fast electron energy for low-density materials such as plastics, whereas for moderate- to high-density materials, this range can be reduced to 1 mm or less.

1.3 Spectroscopic gamma detectors

1.3.1 Background in spectroscopic gamma detection

Since the discovery of γ ray, various methods have been devised for the detection of γ photons.[1,2,9,10,12] The basic idea behind all γ detectors is to convert the energy deposited in the detector into detectable signals such as charge carriers and lower energy photons. These signals are then further converted by corresponding instruments to form electrical signals (charges), which are collected, amplified, shaped and finally read out by the electronics. Since the energy deposition

process is usually very fast (typically on the orders of nanoseconds for gas detectors and picoseconds for solid-state detectors), the temporal response of a detector is mainly determined by the total time used on converting the deposited energy into charges, which is denoted as t_c, the charge collection time.[1,2] Based on the relative length of t_c compared to the interval between two consecutive γ photons, three general modes of detection exists: *current mode, mean-square-voltage mode,* and *pulse mode*. The first two modes are used when t_c is longer than the interval between incoming γ photons, i.e. under high flux of γ photons, where individual γ events cannot be resolved. Due to Compton scattering and various escape processes described above, for typical detectors with limited size, a large proportion of γ photons are unable to deposit their full energy in the detector. In addition, the ratio between the deposited energy to full energy of a γ photon also varies for different γ energies and detector sizes. As a result, detectors working under current mode and mean-square-voltage mode are unable to resolve the absolute energy of incoming γ photons. However, the energy deposited by radiation (or absorbed dose, mean energy deposited per unit mass of matter) is useful in predicting the radiation damage to materials or biological tissues. Therefore, these detectors, mostly gas-filled high-voltage ionization chambers such as the Geiger-Müller counters, are also widely used as radiation dosimeters for various applications with the advantages of great portability and low cost in materials and electronics.

When t_c is shorter than the interval between γ events, the energy deposited by a single γ photon can be converted into electrical charges and collected. The release of collected charges produces a single pulse whose height is proportional to the energy deposited by the gamma photon, which is why this detection mode is called the pulse mode. By recording the occurrence of pulses with

different heights in a histogram called a *pulse height spectrum*, a distribution of energy deposited by an ensemble of γ photons can be drawn.

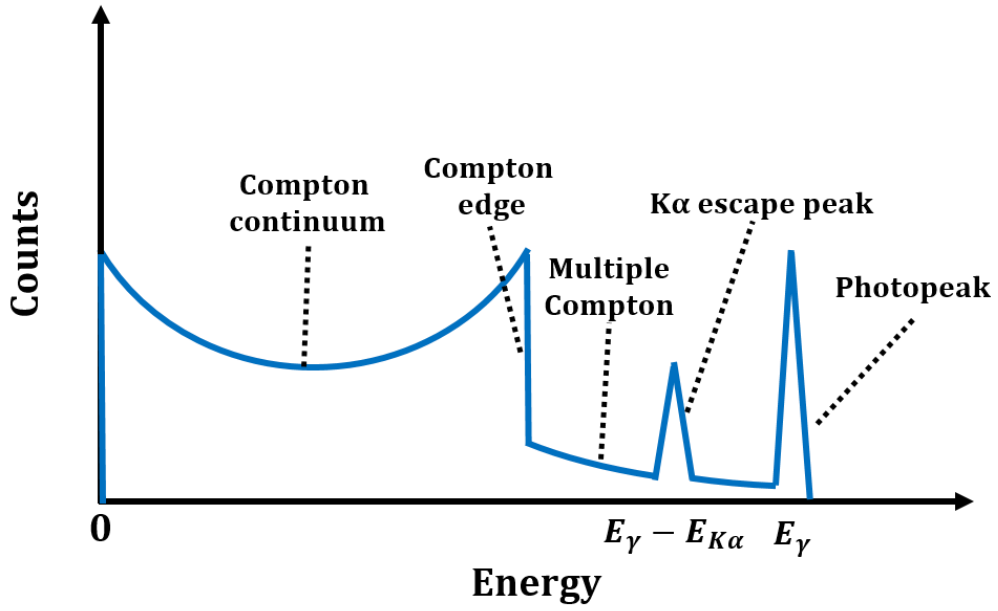

Figure 1.6 Schematic drawing of a simplified pulse shape spectrum obtained using a small-volume, high-Z detector for a single γ source (E_γ < 1 MeV).

Figure 1.6 shows a simplified pulse height spectrum obtained using a limited-volume, high-Z detector for a single γ source (E_γ < 1 MeV), which contains several essential features that will be frequently revisited during the rest of this dissertation. As can be seen, although a substantial amount of γ photons fail to deposit their full energy, which lead to the presence of Compton continuums, Compton edge, multiple Compton continuum, and Kα escape peak, those who succeed in doing so can still produce a photopeak that indicates the full energy of incident γ photons. For high-Z detectors with a substantially large volume, photopeak will be the dominating feature as most escaping high-energy photons will eventually be captured by the detector. Therefore, working in pulse mode, the energies of different γ photons can be resolved on the pulse

height spectrum, realizing spectroscopic detection of the γ photons. The two most important types of spectroscopic detectors, semiconductor detectors (which converts γ energy into charge carriers), and scintillators (which converts γ energy into low energy visible photons) will be discussed in the following sections.

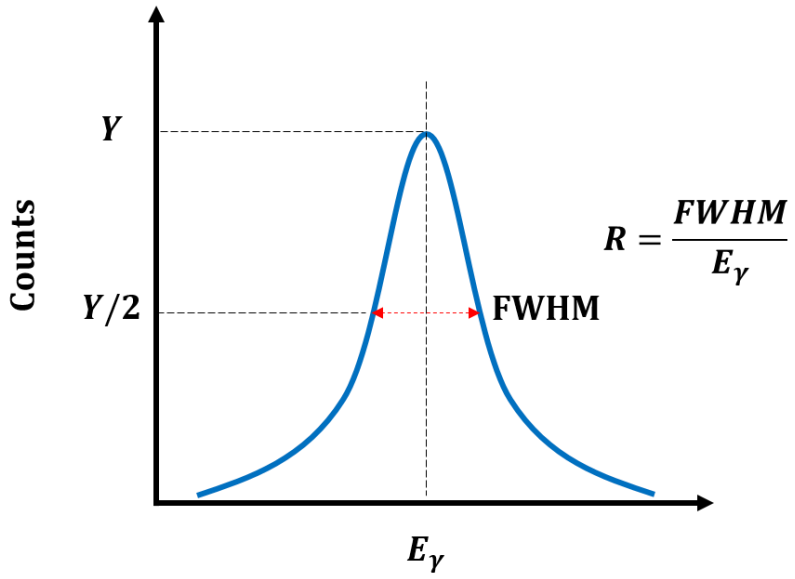

Figure 1.7 Definition of the energy resolution of detector.

Before the discussion of different detectors for γ spectroscopy, it is necessary to take a first look at the spectroscopic energy resolution. Even though the energy of a monochromatic beam of γ photons may be represented by a single photopeak on the pulse height spectrum, the peak can be significantly broadened due to fluctuations within the detector. Such peak broadening may result in overlapped peaks and thus unresolved energies if multiple γ sources are present. Therefore, the detector's capability of producing narrow peaks for monochromatic γ photons becomes an important factor for evaluating its performance. The energy resolution *R* is then used as a quantifying factor. As illustrated in **Figure 1.7**, the energy resolution of a detector is defined as the full width at half maximum divided by the location of the peak detected under a monochromatic

beam of γ photons, where any background is either negligible or has already been subtracted from the curve. The smaller the R value is, the better the detector performs, or the higher the resolution is. A typical energy resolution for semiconductor detectors is smaller than 1%, whereas for scintillators it is 3-10%.[1,2]

There are various reasons behind the broadening of peaks such as performance drifting of the detector, random noise in instrumentation, and statistical noise from the signal itself.[1,2] With the electronics used nowadays, for most detectors, the energy resolution is limited by the third type of noise which is inherent to the random fluctuating nature of discrete signals. Assuming the formation of each charge signal (charge carrier or photoelectron generated by low energy photons in the photodetector) in a single γ event follows a Poisson process, the signals obtained for many γ events should have a Poisson distribution. Assuming the average number of total signals formed in a γ event is *N*, as N is large, the Poisson distribution can be written in a Gaussian form:

$$G(x) = \frac{A}{\sigma\sqrt{2\pi}} \exp\left(-\frac{(x-x_0)^2}{2\sigma^2}\right) \tag{1.5}$$

where σ, A, and x_0 are the standard deviation, area, and centroid (or average pulse height) of the distribution curve, respectively. Assuming the detector responds linearly to the generated signal N with a proportional factor K, the average pulse height x_0 is then KN, and the standard deviation σ is $KN^{0.5}$. Since the FWHM in a Gaussian distribution is equal to 2.35σ, the Poisson limiting resolution is then

$$R_{Poisson\ limit} = \frac{FWHM}{x_0} = \frac{2.35K\sqrt{N}}{KN} = \frac{2.35}{\sqrt{N}} \tag{1.6}$$

As can be seen from Eq. 1.6, the resolution is in fact limited by the intensity of signal generated in the detector. Therefore, increasing the capability of generating charge signals (charge carriers for

semiconductor detectors, or light yield as photons/MeV for scintillators) has become a major goal in γ detector development, as would be discussed later on.

It has been found that for semiconductor detectors, the resolution can be lower by a factor of around 3 compared to the Poisson limit.[1,10] Such enhanced resolution has been ascribed to a less independent charge signal formation process in these detectors. The *Fano factor*, *F*, is then introduced to account for the differences between the observed variances and Poisson dictated variances (σ^2):

$$F \stackrel{\text{def}}{=} \frac{observed\ variances}{\sigma^2} \tag{1.7}$$

Then the statistical limit in resolution is given by:

$$R_{statistical\ limit} = \frac{2.35\sigma\sqrt{F}}{x_0} = \frac{2.35K\sqrt{N}\sqrt{F}}{KN} = 2.35\sqrt{\frac{F}{N}} \tag{1.8}$$

The Fano factor is significantly smaller than 1 for semiconductor detectors. However, for most scintillators, the Fano factor is still close to unity.

1.3.2 Scintillators

With the capability of converting radiation energy into visible photons, scintillators are one of the oldest materials used by mankind to detect radiation.[2] Although the utilization of scintillating ZnS screens had already been demonstrated by Ernest Rutherford in his detection of scattered alpha particles for the elucidation of atom structure as early as in 1911, it was not until the developments of high-precision photon-counting equipment and large-size scintillation crystals that the spectroscopic detection of γ photons could be carried out with scintillators.[1,2,13] **Figure 1.8** shows a schematic illustration of the detection process of a γ photon using scintillator coupled to

photomultiplier tube (**PMT**). The γ photon first deposits its energy as excitons in the scintillator following processes introduced in section 1.2. The excitons further recombine to form visible photons. With the assistance of reflective coatings, the as-formed visible photons were out-coupled into a PMT. The negatively charged photocathode in the PMT made of low work-function materials is capable of producing photoelectrons after absorbing the visible photons, which typically has a peak quantum efficiency of around 0.3 in the most sensitive blue spectral region.[1,2] Under the high-vacuum environment inside PMT, the photoelectron is accelerated by the voltage difference between the photocathode and the first dynode and gains significant kinetic energy. The accelerated photoelectron then strikes the dynode and produces multiple electrons that are further accelerated towards the second dynode under electric field. This process is typically repeated for more than 10 times depending on the number of dynodes, with the original photoelectron being substantially "multiplied" into millions of electrons. These electrons have sufficient charges to create a readable signal and are finally collected by the anode for further signal amplification and processing. The great sensitivity (single photon detectable) and fast response (response time around a few nanoseconds) of PMT enable the detection of extremely weak photon pulses (typically around 10^3 to 10^4 photons/MeV of γ energy) produced by a single γ event in the scintillator, which facilitates the spectroscopic detection of γ rays in the pulse mode as described before.

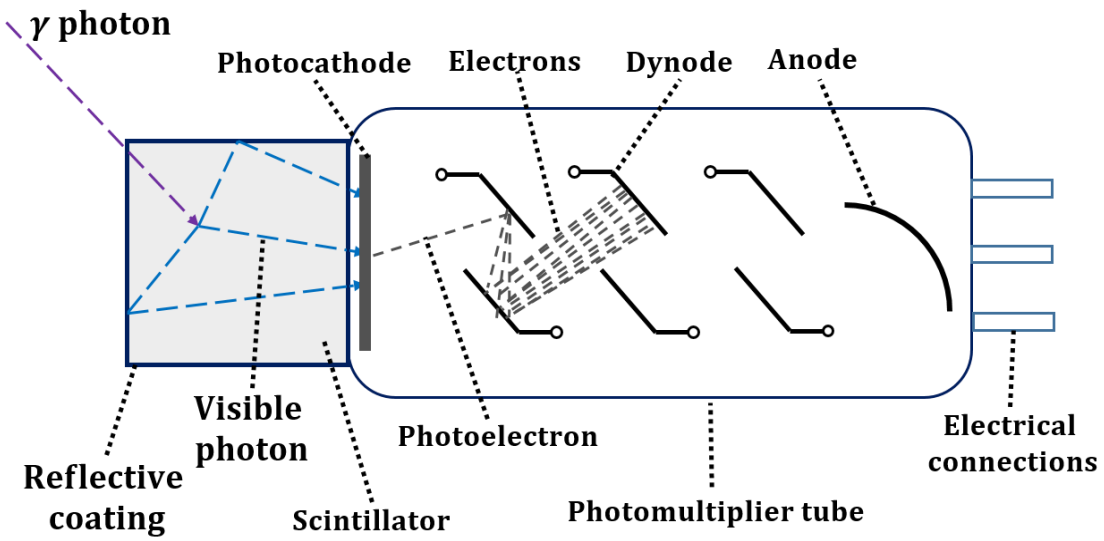

Figure 1.8 Schematic illustration of the detection of γ photon using a scintillator coupled to a photomultiplier tube.

To date, a great variety of scintillator materials have been developed and commercialized for the detection of γ photons.[1,2,9,11,12,14] Based on the materials used, the scintillators can be generally categorized into organic scintillators and inorganic scintillators. Typically, inorganic scintillators consist of a bulk single-crystalline inorganic matrix doped with luminescent activator atoms (around 10^{-3} mol%), whereas organic scintillators comprise a plastic or single-crystalline organic matrix with conjugated structures containing a small amount of fluorescent dye molecules (1-3 % by weight of matrix). The different materials and structures lead to different γ photon responses obtained by these scintillators, which will be discussed further in detail in section 1.4.1, but typically, inorganic scintillators perform better in energy resolution and γ photopeak detection, whereas organic scintillators have faster emission, better neutron response, and lower costs.

An ideal scintillator for γ spectroscopy should have the following characteristics:

1) High Z, since the photopeak cross-section is strongly dependent on the material's Z;

2) High light yield (number of photons produced per MeV of γ photon energy), since the scintillator's energy resolution is inversely proportional to the square root of photoelectrons produced by the photomultiplier tube;
3) Good optical transparency at the wavelength of emitted photons to reduce loss of photons due to excessive absorption;
4) Good spectral match of the emission spectrum to the PMT's spectral range of peak sensitivities;
5) Fast decay of fluorescence to reduce pulse pile-up for detection under high γ photon influxes;
6) Linear scintillation response proportional to the energy of incident γ photon;
7) Capability of being fabricated at large scales with low cost; mechanically rugged and chemically stable (e.g. non-hygroscopic).

As will be discussed later, no conventional scintillators can achieve all of these requirements due to limitations in their intrinsic material properties and fabrication requirements. As the recent advancement in nanotechnologies brings new techniques in the fabrication of nanomaterials with novel properties, the fabrication of nanocomposite scintillators comprising a plastic matrix and dispersed high-Z nanomaterials has been proposed for the integration of strengths from both the organics and inorganics. Although a number of attempts have already been made for this purpose, so far there has not been much success due to limited knowledge in the fabrications and energy transfer schemes in these systems. The current status of development for the nanocomposite scintillators will be briefly reviewed in section 1.4.2, after the introduction of traditional scintillators.

1.3.3 Semiconductor detectors

Semiconductor detectors are another important class of spectroscopic γ detectors.[1,9,10] Unlike scintillators, semiconductor detectors convert the energy of γ photons into charge carriers, and the collection and detection of these charge carriers give the energy information on the incident γ photons. The biggest advantage of semiconductor detector over scintillators is their greatly improved resolution. Such advantage can be ascribed to two factors: 1) Semiconductor detectors is capable of producing much more information carriers (charge carriers) than scintillators (photocathode photoelectrons), which can be ascribed to the much lower energy required for the production of a charge carrier (around 3 eV) compared to that for a scintillation photon (tens of eV); and 2) the Fano factors for semiconductor detectors are usually much smaller than 1, compared to the near unity Fano factor for scintillators. As a result, for applications requiring high precision in energy resolutions (< 3%), semiconductor detector is often the only choice.

However, compared to scintillators, semiconductor scintillators are much more expensive to fabricate and operate. The high fabrication cost results from the requirement of a large detector with extremely high purity, which is necessary for the centimeters-thick detectors to work under a fully depleted mode.[1,10] For a germanium detector with depletion region of 10 mm under a reversed bias less than 1000 V, the impurity concentration required is approximately $10^{10}/cm^3$, which is less than 1 part per trillion.[1] Such level of purity in bulk materials can thus far only be achieved on germanium, which is probably the purest material ever produced in commercial volumes. In addition to the cost from fabrication, the operation of *high-purity germanium* (HPGe) detectors can also be quite costly, as these detectors have to be cooled to liquid-nitrogen temperature (77 K)

to avoid significant thermal fluctuations due to the small band-gap of germanium (0.75 eV at 0 K). Although a number of new materials such as CdTe, $Cd_{1-x}Zn_xTe$, HgI_2, and organo- or cesium-lead halide perovskites have been proposed and studied in recent years as the higher-Z, room-temperature substitutes of HPGe detectors, their performance is still substantially inferior to the HPGe, mainly due to the difficulties in achieving a high purity level at large detector sizes.[1,9–11,15,16]

1.4 Overview of gamma scintillators

The study and development of scintillation materials have continued for decades, with only a handful of successes leading to commercial products.[1,2,9,11–14,17–20] Therefore, before digging into the topics of nanocomposite scintillators, it is essential to take a first look at the achievements and findings in the development of conventional scintillators. Section 1.4.1 will provide a brief review on the important inorganic and organic scintillators developed thus far, and the mechanisms of photon generation in both systems will also be stressed. Then the current status of nanocomposite scintillator development will be introduced in section 1.4.2, which shall provide the background needed for further discussions in the rest of this dissertation.

1.4.1 Conventional scintillators

1.4.1.1 Inorganic scintillators

The discovery of outstanding scintillation response of thallium doped sodium iodide crystal by Robert Hofstadter in 1948 allowed for the first time the spectroscopic detection of γ photons by small-size compact detectors.[1,2,13] Since that, inorganic scintillators have always been the focus of scintillation γ photon detection.[1,2,9,11,12,14,17,18,20–23] Typical inorganic scintillators are made of

single crystals of large band-gap salts of halides or oxoanions, which is further doped with activator atoms with appropriate energy states. Normally at least one element constituting the salt will have a high Z of at least 50. Such high Z and high density give the inorganic scintillator high attenuation power and high photoelectric cross-section of γ photons, facilitating the spectroscopic detection of γ ray. Commercial single-crystal scintillators of around 3×3×3 $inch^3$ can be produced by melt crystallization and zone-refining, which have exceptional optical clarity and good γ stopping power. However, the production and purification process is time- and energy-consuming, and the size of single crystal is limited by the ingot used. In addition, the fact that most salts used are hygroscopic also results in the requirement of careful packaging for the product scintillator. These factors together result in a high price of inorganic single-crystal scintillators, which limits their wide deployment where large volumes are needed.

The scintillation mechanism for an inorganic single-crystal scintillator is shown in **Figure 1.9**. The excitation process mentioned in section 1.2 excites a valence band electron to the conduction band, leaving a hole in the valence band of the crystal matrix. The electron and hole then diffuse in the crystal on their respective energy band and get captured by an activator atom. The electron sitting on the excited state of activator radiatively de-excites and recombines with the hole on the activator's ground state, which generates a visible photon for detection. The lower energy gap for activator states compared to the matrix lead to a great matrix transparency to the emitted photons. Typical light yields for good inorganic single-crystal scintillators are in the range of 30000 to 80000 photons/MeV, which is much higher than that of the organic scintillators (up to 17000 photons/MeV). The higher light yield of inorganic scintillators is typically ascribed to a lower

ionization energy for exciton generations; however, the exact reasons behind this lower ionization energy are still unclear.

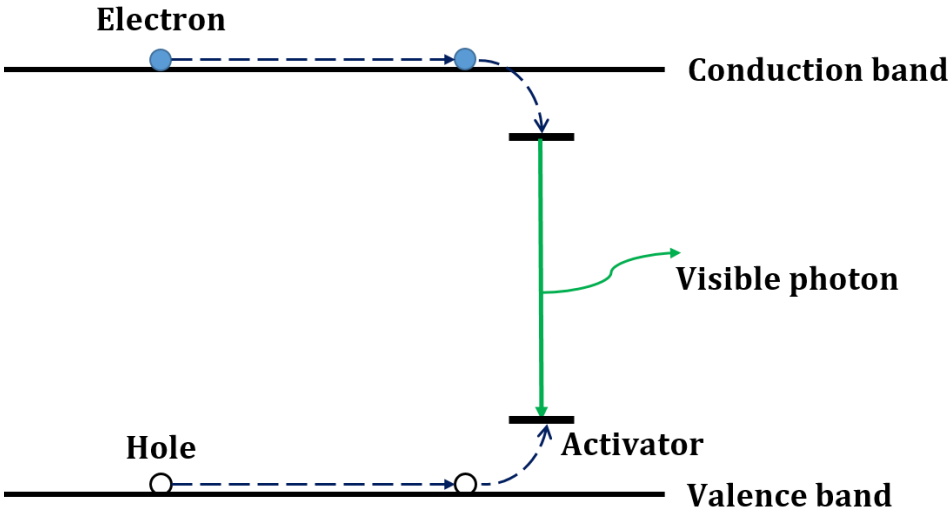

Figure 1.9 Scintillation mechanism of an inorganic single-crystal scintillator.

One great shortcoming of the inorganic scintillators is their slow fluorescence decay. The decay lifetimes of fluorescence for inorganic scintillators are determined by the activator's property and can range from tens to thousands of nanoseconds. In addition, most single crystals also contain certain shallow trap states below the conduction band due to defects and impurities. Electrons trapped in these states may be excited back onto the conduction band by thermal energy. Activator captures of these electrons can result in the production of undesirable fluorescence with long, non-exponential decay lifetimes, which is called an *afterglow*.

The properties of some commercially available inorganic and organic scintillators are summarized in **Table 1.1**. The most widely used inorganic scintillator, NaI(Tl), still serves as a good standard for scintillators nowadays due to its good light yield of 38000 photons/MeV, decent Z and density, and great spectral match with PMT (emission at 415 nm). Long decay constants and hygroscopicity

are common disadvantages of inorganic scintillators. For most inorganic scintillators whose light yields are higher than NaI(Tl), they suffer either from poor spectral match with PMT such as CsI(Tl), or extremely long decay time and afterglow like SrI_2(Eu). One of the few newly developed scintillators with exceptional performance is $LaBr_3$(Ce), which boasts both significantly improved light yield and decay lifetime while retaining a good spectral match with PMT.[19] The biggest shortcoming of this great scintillator is its astonishingly high price (> 2000 Euro/in^3) due to high costs from raw materials and processing, which severely restricts its widespread usage.

Table 1.1 Properties of common inorganic and organic scintillators

	Light yield (photons/MeV)	**Decay constant (ns)**	**λ_{max} (nm)**	**Density (g/cm^3)**	**Hygro-scopic?**	**Other**
NaI(Tl)	38,000	230	415	3.67	Y	
CsI(Tl)	65,000	680 (64%), 3340 (36%)	540	4.51	Y	
BGO	8,200	300	480	7.13	N	Highest Z
$LaBr_3$(Ce)	63,000	26	380	5.29	Y	
SrI_2(Eu)	85,000	1200	435	4.6	Y	
BC400	10,000	2.4	423	1.032	N	
BC452	4,900	2.1	424	1.080	N	Lead, 5%
BC454	7,380	2.2	425	1.026	N	Boron, 5%

1.4.1.2 Organic scintillators

Organic scintillators are another important class of scintillation detectors.[1,2,5,9,12,24,25] There are two classes of organic scintillators: single crystals and amorphous, with the latter consisting both liquid scintillators and plastic scintillators. Organic single-crystal scintillators have been made from pure anthracene or stilbene. These single crystals have the highest light yields (up to 17000 photons/MeV) among organic scintillators; however, the sheer difficulty to grow large-size crystals and their poor mechanical endurance prevent widespread applications of these scintillator. Instead, plastic and liquid scintillators become the mainstream organic scintillators due to their

great advantage in large-scale production. The structures of these two kinds are virtually the same, with plastic scintillator being a "solid solution" version of the liquid scintillator.

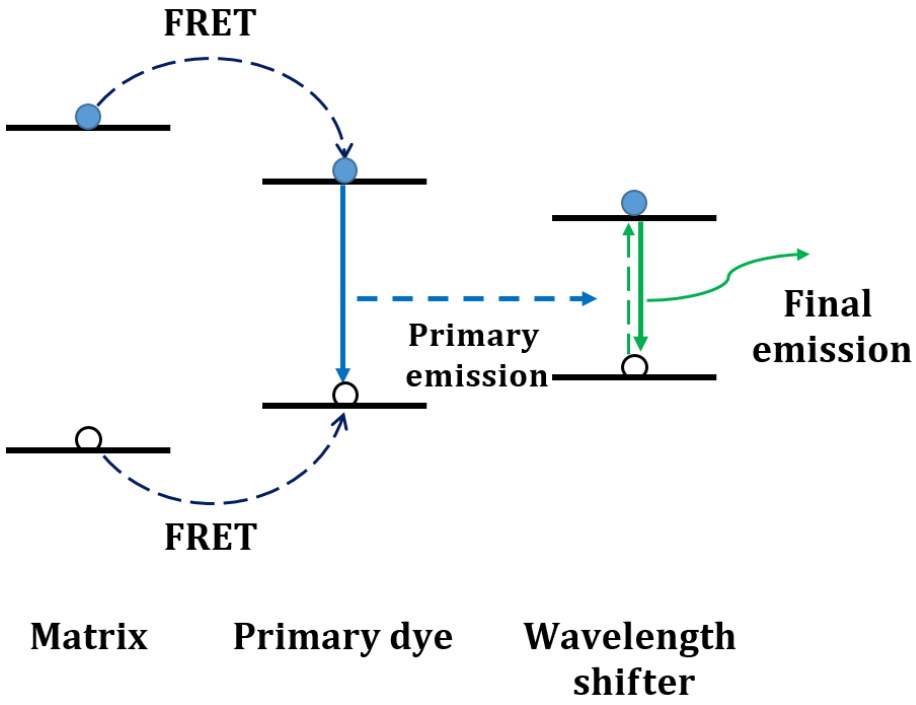

Figure 1.10 Scintillation mechanism of an organic scintillator.

A typical plastic scintillator consists of a polymer matrix with conjugated structures such as polystyrene and polyvinyltoluene (or toluene, xylene, and pseudocumene for liquid scintillators), a primary dye at a relatively high loading (1-3% by weight), and a secondary dye, or wavelength shifter at a much lower loading (0.01-0.1% by weight). **Figure 1.10** shows the scintillation processes involved in a plastic scintillator. Most excitons are generated in the matrix following the interactions described in section 1.2. Matrix material with conjugated structures are preferred as the excited conjugated π electrons have lower energy states and can form excitons, unlike σ electrons whose excitation often causes ionization and bond breaking. Since typical matrix polymers have relatively low fluorescence quantum efficiency (less than 10%), a highly

fluorescent organic dye whose absorption matches well with the matrix emission is added to facilitate exciton transfer via Förster resonance energy transfer (**FRET**).[2,26,27] The non-radiative FRET process proceeds via dipole-dipole coupling and is effective within a donor-acceptor distance of 1 to 10 nm. Another non-radiative process called the Dexter energy transfer which is basically direct exciton diffusion can also help exciton transfer.[26,28] However, Dexter energy transfer can only occur at distances within 1 nm and therefore is only a minor component in exciton transfer. At a primary dye loading of 1-3% by weight, FRET is very efficient, and most matrix excitons shall be transferred to the primary dye sites. Radiative recombination of excitons then happens at the dye site, producing a primary emission characteristic of the primary dye. In many cases, in order to reduce self-absorption by primary dye when the scintillator volume is large and to shift the primary emission to match PMT's peak sensitivity spectral region, a high-quantum-efficiency wavelength shifter will also be added at very low concentrations of 0.01% to 0.1% by weight. At this concentration, the donor-acceptor distance is much greater than 10 nm, rendering FRET an unlikely process. Wavelength shifting is then primarily carried out as the wavelength shifter absorbs the primary emission and re-emits lower-energy photons. Commonly used primary dyes include polyphenyls and oxazole derivatives such as n-terphenyl (PPP), 2,5-diphenyloxazole (PPO) and 2-phenyl-5-(4-biphenylyl)-1,3,4-oxadiazole (PBD), with their emission peaking at around 340-370 nm.[2,29] The most commonly used wavelength shifters include 1,4-di-(5-phenyl-2-oxazolyl)-benzene (POPOP) and 2,5-bis(4-biphenyl)oxazole (BBO), with their emission peaking at around 420 nm.[2,29]

One key advantage of organic scintillators is their fast emission dictated by the nature of singlet's short lifetime. A fluorescence decay lifetime of only a few nanoseconds is typical for most organic

scintillators, which renders them a great candidate for high count rate applications.[2] In addition, the good responses of organic scintillators to alpha particle, beta particle, and fast/slow neutrons (with boron doping, see **Table 1.1**) provide more versatile applications compared to the inorganic scintillators.[2,12,24,30] Moreover, the feasibility of large-scale production of plastic/liquid scintillators also facilitates their deployment as large-size portal detectors or for other specific purposes.[5] However, one big disadvantage of organic scintillators is their very low Z (< 6) compared to the inorganic scintillators. As a result, it becomes almost impossible to perform spectroscopic detection of γ photons using organic scintillators. Although the addition of inorganic constituents such as Pb has been tried to improve the Z of organic scintillators, other adverse effects such as decreased light yields also take place (**Table 1.1**).[2,31,32] The development of high-Z loaded plastic-based nanocomposite scintillators will be reviewed in the following section, where the influence from various factors such as light yield, scattering, and band structures of nanocomposites will also be discussed.

1.4.2 Nanocomposite scintillators

1.4.2.1 Nanocomposite scintillators with organometallics

The addition of high-Z constituents has long been sought after as a solution to improve the stopping power and photoelectric cross-section of organic scintillators. The addition of organometallic compounds of bismuth, lead and mercury was initially studied in the 1950-1960s.[2,29,31–34] However, the addition of these high-Z organometallics nonetheless caused severe quenching of light yield. As can be seen from the commercialized BC-452 scintillator, with only 5% by weight of Pb, the light yield decreases to about 50% of the original plastic. After fruitless explorations for nearly

two decades, no further development was made for a long period of time, with very few products successfully commercialized.

The recent development in high-efficiency organic phosphorescence light emitting devices provides a profound understanding of the triplet photophysics and their utilization for photon production, which also helped the studies in high-Z organometallic nanocomposite scintillators.[28,35–37] It has been found that the severe quenching of light yield is a result of the strong spin-orbit coupling induced by the high-Z organometallics, which converts emissive singlet states into the commonly non-emissive triplet states.[2,33,34] Recently, Payne *et al.* have demonstrated that, by matching the triplet energy level of high-Z triphenylbismuth to that of a polyvinylcarbazole (PVK) matrix, triplets generated on the triphenylbismuth site can be transferred to matrix.[38] The further addition of bis[2-(4,6-difluorophenyl)pyridinato-C^2,N](picolinato)iridium(III) (FIrpic), a triplet emitter that is capable of converting both singlets and triplets into photons, facilitates the conversion of matrix triplets into visible photons. Due to the appropriate arrangement of triplet energy levels, the addition of triphenylbismuth did not adversely affect the light yield in this case, and a photopeak with 6.8% resolution has been obtained. However, as efficient Dexter energy transfer requires the addition of at least 3% by weight of the costly iridium-based triplet emitters, the fabrication of large-scale γ detectors using this recipe will be very expensive, limiting their wide deployment. Recent studies by Feng and van Loef *et al.* indicate that the addition of tetra-alkyl tin compounds may avoid the use of triplet emitters due to the weaker spin-orbit coupling effect by the lower-Z tin.[39–41] However, the moderate Z and low absolute loadings of Sn achievable due to the large alkyl groups still limit the application of this system.

1.4.2.2 Nanocomposite scintillators with nanoparticles

The past two decades have witnessed significant advances in the development of new nanostructures. A wide range of high-Z nanoparticles such as BaF_2, HfO_2, rare earth fluorides and oxides, and II-VI semiconducting quantum dots have been synthesized.[42–57] At a time like this, another idea of fabricating nanocomposite scintillators using these high-Z nanoparticles instead of organometallics have been formed. Due to strong excluded volume effect and high melting point of typical scintillation polymers (polyvinyltoluene, polystyrene, etc.), direct mixing of polymer and nanoparticles is impractical in producing transparent nanocomposites.[58,59] Therefore, most works discussed here used in situ polymerization for the fabrication of nanoparticle/polymer nanocomposites.

The first report from Vasil'chenko and Solov'ev in 2003 used mechanically ground particles of 10 μm diameter with BC-600 epoxy adhesive for the fabrication of composite scintillator.[60] However, the large size of these nanoparticles caused severe optical loss and therefore poor performance of the result nanocomposite. In 2006, Campbell and Crone proposed the mixing of quantum dot with semiconducting polymer for the fabrication of scintillation detectors.[61] They claim that the light yield can be improved by adding quantum dots into the organic matrix due to the lower ionization energy of quantum dots. However, only the fabrication of a thin film was presented, rendering this work of little practical interest. Following this work, the fabrication of bulk nanocomposites containing quantum dots has been carried out by several separate groups.[62–64] However, the quantum dot loadings for transparent nanocomposites reported in these papers are all very low (< 0.5% by weight), which is due to the aggregation of quantum dots at high loadings as attempted by Lawrence *et al*.[64] Considering the moderate Z of quantum dots, such low loadings have very

limited effect in Z improvement. Furthermore, the quantum dots used in these reports all have long emission (> 510 nm), to which the commercial PMTs all have very low sensitivity. As a result, no good pulse height spectra were obtained in these works.

Since a good PMT response is important for light yield, many researchers focused on the fabrication of nanocomposites using large-band-gap nanoparticles or nanoparticles of conventional inorganic scintillation materials, such as Ce doped BaF_2 and LaF_3 nanoparticles.[65–67] McKigney *et al.* reported the fabrication of nanocomposite scintillators made of LaF_3:Ce dispersed in polymer matrix with an emission at 350 nm.[65] However, the aggregation of nanoparticles caused the nanocomposite to be translucent at a thickness of only a few mm, rendering this nanocomposite unsuitable for large-size detectors. A follow-up work by Feller *et al.* demonstrated the large-scale synthesis of LaF_3:Ce nanoparticles and the use the viscous oleic acid as a matrix for hosting nanoparticles.[66] Their LaF_3:Ce/oleic acid nanocomposites reportedly contains 20-60% by weight of LaF_3:Ce nanoparticles and is still somewhat transparent at a thickness of 1 cm. However, this "nanocomposite" is essentially a gooey solution of extremely high concentration LaF_3:Ce in oleic acid, which lacks the mechanical robustness to be shaped and polished. In addition, the light yield of this nanocomposite was also measured to be quite low, of only around 1600 photons/MeV. Other than the work on LaF_3:Ce, a paper by Kang *et al.* in 2011 reported on the synthesis of epoxy nanocomposite containing BaF_2:Ce nanoparticles as a nanophosphor.[67] By matching the refractive index between epoxy and BaF_2:Ce, they achieved a good transparency of around 40% at 550 nm for a 3-mm-thick nanocomposite which contains roughly 10% by weight of BaF_2:Ce nanoparticles. However, the nanocomposite was not transparent to its own emission at 350 nm, rendering it of little use as a practical scintillator. There have also been a large number of papers on the

development of doped emissive high-Z nanophosphors; however, there are much fewer reports on the incorporation of these nanophosphors into a polymer matrix, primarily due to the lack of a good way to resolve the issue of severe nanoparticles aggregation in polymer.[43,68–70]

A recent work by Pei *et al.* made a breakthrough on the fabrication of transparent high-loading nanoparticle/polymer nanocomposite scintillators.[71] By grafting methacrylate groups onto the surface, the nanoparticles can be covalently bonded onto the growing polymer chain. *In situ* polymerization of a monomer solution containing these methacrylate-grafted nanoparticles then produced highly transparent nanocomposite monoliths containing up to 20% by weight of Gd_2O_3 nanoparticles. With the addition of a green fluorescent dye, the detection of a 662 keV γ photopeak with 11.4% resolution was demonstrated using their transparent Gd_2O_3–loaded nanocomposite. However, this resolution is still far from the 6% resolution of NaI(Tl), and the loading and Z achieved for this system also have a big room for improvement.

1.5 Motivation and research scope of the dissertation

As stated before, conventional scintillators suffer from either high price, limited scale, slow decay for the inorganic single crystals, or from poor light yield and low gamma attenuation power for the plastic scintillators. While the concept of mixing inorganic high-Z nanoparticles into plastic matrix has been proposed to leverage high Z of the inorganics with the fast emission and low cost of plastics, current progress in its development is still in the nascent stage, with only proof-of-concept prototypes presented whose composition and performance are both far from ideal. Major obstacles at the current stage of development are:

a) Limited methods in synthesizing uniformly distributed small-size (<10 nm diameter) high-Z nanoparticles with good solubility in low-polarity organic solvents;
b) Difficulty in preventing nanoparticle aggregation during the formation of nanocomposites, be it either via direct mixing or by in situ polymerization, which has limited the loadings of nanoparticles and thus the possible improvements in Z;
c) Limited studies and understandings of the energy transfer processes involved in the nanocomposites, which results in the poor choice of materials with inappropriate photophysical characteristics.

Acknowledging the current shortcomings in nanocomposite scintillators, the focus of this dissertation is then leveraging the understandings in chemical synthesis, surface chemistry, polymer chemistry, and photophysics to tackle these problems and improve the performance of nanocomposite scintillators. In a more specific way, the subjects studied are:

1) Explore new ways of synthesizing novel small-size, highly soluble high-Z nanoparticles;
2) Search for solutions to alleviate or prevent aggregations of nanoparticles. Here the focus is to develop proper surface modification protocols of nanoparticles to prevent them from being excluded during polymerization.
3) Study the photophysics and energy transfer processes in nanocomposites to help design systems with an improved light yield.

Based on the work completed during my PhD study, this dissertation is divided into five chapters:

Chapter 1, the current chapter, provides an overview of the research topic covered in the dissertation, which includes a brief introduction on gamma ray, basic knowledges on the physics of gamma-matter interactions, a summary of currently available spectroscopic gamma detection methods with a special focus on scintillators, followed by research motivation and layout of the dissertation.

Chapter 2 presents the development of HfO_2-nanoparticle-based nanocomposite scintillators. Subjects covered include the development of a novel synthesis and surface modification protocol for HfO_2 nanoparticles, and the fabrication, photophysics study and performance characterization of the high-loading, transparent nanocomposite scintillator. The influence of added nanoparticles on light yield is carefully studied. Based on the observation and analysis, a mechanism on energy trapping and photon scattering by nanoparticles is proposed to account for the change in light yield.

Chapter 3 shows an extended work based on Chapter 2. The single-precursor synthesis protocol for HfO_2 nanoparticles is extended to all group IVB metal oxides (ZrO_2 and TiO_2). Reaction mechanism for the nanoparticle formation is studied and discussed, followed by a demonstration of these nanoparticles' application in high refractive index nanocomposites.

Chapter 4 continues the exploration on nanocomposite scintillators. The use of quantum dots in nanocomposite scintillators is proposed to circumvent the light yield deterioration issue induced by energy trapping of the non-emissive nanoparticles. The fabrication of ultra-high-loading quantum dot/polymer nanocomposite scintillators is presented, and the photophysics and energy transfer from quantum dots are studied and discussed. Simultaneous improvements in both Z and

light yield are demonstrated using the as-fabricated ultra-high-loading quantum dot/polymer nanocomposite scintillators.

Finally, **Chapter 5** summarizes the work and provides an outlook for future research.

Chapter 2. Hafnium oxide nanoparticle/polymer nanocomposite scintillator

2.1 Introduction

Polymer nanocomposites, usually prepared by dispersing nanomaterials within a continuous polymeric matrix, have been widely utilized in applications such as energy harvesting,[58,72,73] smart materials,[74,75] and novel structural materials[76] due to their potential for multi-functionalization and property enhancement. In contrast to phase-separated macro-composites or molecularly dissolved solutions, nanocomposites attain nanometer-scale mixing to retain certain condensed-state properties of the individual components, e.g. band structures and photoluminescent characteristics, while exhibiting other important properties characteristic of amorphous solid solutions, such as good optical transparency.[58,71–77] However, due to the high specific surface area and surface energy of nanomaterials, conventional mixing technique usually results in severe aggregation and phase separation within the nanocomposite, thus diminishing its uniformity and transparency.[58] Although strategies such as *in situ* formation of nanophase, and nanoparticle surface modification have been employed to suppress aggregation, fabrication of bulk-size nanocomposite with high loading of nanomaterials and decent transparency still poses a significant challenge.[71,78–81]

Spectroscopic detection of γ-rays is desirable for high energy physics study, nuclear medical imaging and nuclear non-proliferation.[1,2,4] However, the detection efficiency is intrinsically

limited by the high penetration power of high energy photons.[1,9,10] Other than the high-cost delicate semiconductor detectors, scintillators are the most viable solution to resolve gamma energy by, in the most ideal case, proportionally converting the radiation energy into countable visible photons.[1,9] Conventional scintillators generally fall under the categories of inorganic single-crystal scintillators and organic scintillators.[12,25] The former, typically with effective atomic numbers (effective **Z**) greater than 50, usually exhibits much better gamma stopping power than their organic counterparts (effective Z around 6), as the probability of depositing all energy of a gamma photon into a single fast electron (known as the photoelectric effect) is proportional to the fourth to fifth power of the material's atomic number.[1,25] In addition, the energy resolutions of inorganic single-crystal scintillators are also usually better than the organics due to higher light yield.[1] However, the demanding processes of growing large-size single crystals result in high cost for inorganic scintillators and thus hinder their widespread deployment.[9,17] Recently, high-Z loaded composite systems utilizing quantum dots, scintillation nanocrystals, and high-Z organometallic compounds have been proposed to increase the γ-stopping power and photoelectric cross-section for plastic scintillators.[38,42,61,62,64–68] However, reported quantum dot- and nanocrystal-polymer nanocomposites suffer from high optical loss due to aggregation and self-absorption at nanoparticle loadings higher than 10 wt%. In addition, the moderate effective Z (around 30 to mid-50's) of these nanoparticles limits their efficiencies in γ energy deposition. Moreover, the reported nanocomposites emit in the long-wavelength range of the visible spectrum, which limits photon detection by the commonly used commercial photomultiplier tubes (**PMT**) with peak sensitivity in deep blue and result in poor energy resolution.[61–64,66,67] Composites with high-Z organometallic compounds such as triphenylbismuth have demonstrated enhanced gamma stopping power. However, the poor thermal stability and relatively low band gap of triphenylbismuth (4.1 eV as

compared to 4.2 eV for polyvinyltoluene (**PVT**), a common matrix for blue-emitting plastic scintillators) can result in substantial exciton quenching and thus a diminished light yield. In addition, molecularly dispersed high-Z compounds can also effect significant spin-orbit coupling, reducing the population of singlet excitons available to be emitted by the singlet-only emitters used in most organic scintillators.[2,38] Although a phosphorescent system comprising poly(9-vinylcarbazole) and bis[2-(4,6-difluorophenyl)pyridinato-C^2,N](picolinato)iridium(III) has recently been reported to match triphenylbismuth's band gap and triplet energy level in order to harvest both singlet and triplet and thus achieve high light yield, its application potential could still be limited due to the system's long phosphorescence decay lifetime and high cost of organo-iridium compound.[38] Pei *et al.* have previously reported a large-band-gap, high-Z Gd_2O_3/polymeric matrix/fluorescent dye tertiary system for γ-ray scintillation, which is capable of producing a photoelectric peak (photopeak) with 11.4% energy resolution for 662 keV γ radiation.[71]

Figure 2.1 illustrates the photoelectric process in the tertiary nanocomposite system. Ideally, the high-Z nanoparticle converts all energy of an incident gamma photon into a single photoelectron. The photoelectron then undergoes energy cascade by colliding with other electrons on its path to produce a number of excitons within the matrix. Through Förster resonance energy transfer (**FRET**, which is the main energy transfer process in plastic scintillator), the excitons transfer to fluorescent dyes from which visible photons are generated.[2] The progressively decreasing band gaps going from high-Z nanoparticles (> 5 eV) to the PVT matrix (4.2 eV), and then to the dyes (< 3 eV, typically at concentrations of a few percent) allow for efficient uni-directional exciton energy transfer to the dyes with little quenching. Moreover, the surface modified Gd_2O_3 (Z_{Gd} = 64)

nanoparticles can be added at a net weight percentage of about 20% without severe optical loss at thicknesses of a few mm, endowing the nanocomposites with higher stopping power as compared with the quantum dot/polymer nanocomposites in which the loading of high-Z ingredient is much lower.[71] However, the modestly high Z of Gd still limits the γ detection efficiency of this system, while the nanocomposite's green emission additionally limits its energy resolution for spectroscopic applications due to spectral mismatch with commercial PMTs.

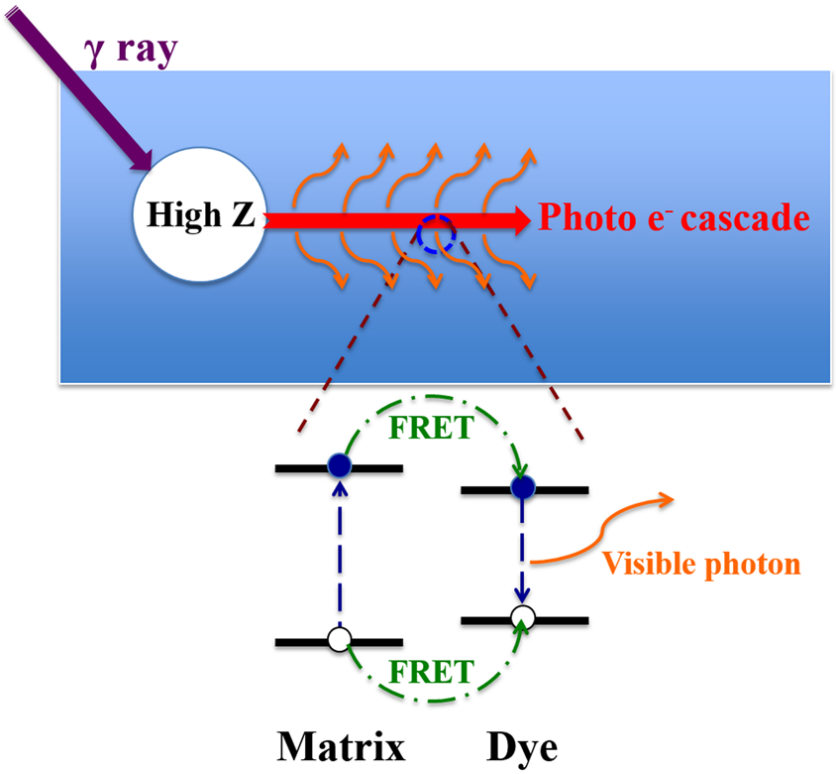

Figure 2.1 Gamma scintillation mechanism in a nanocomposite monolith loaded with high Z nanoparticles.

HfO_2 has been intensively investigated in the recent years as a promising high-κ dielectric.[82] With a Z-value of 72 for Hf and reported band gaps of 5.3 – 6.0 eV, HfO_2 has the highest effective Z amongst all simple oxides with band gaps exceeding the 4.2 eV for PVT.[83,84] Although rare earth doped HfO_2 have also been investigated as luminescent scintillation materials, there is limited

success due to the resulting materials' poor photophysical properties, especially the long decay time.[43,69] Thus far, the syntheses of HfO_2 nanoparticles have been reported through a handful of methods such as hydrolysis,[85,86] solvothermal synthesis,[87,88] and non-aqueous sol-gel synthesis.[53,89] nanoparticles produced by the first two methods tend to aggregate and precipitate in normal non-polar solvents and are thus deemed unsuitable for fabricating uniform nanocomposites with low-polarity polymers such as PVT. While the sol-gel method can produce soluble HfO_2 nanoparticles by condensation between $HfCl_4$ and $Hf(OCH(CH3)_2)_4$ in the presence of trioctylphospine oxide,[53] the air- and light-sensitive nature of $Hf(OCH(CH3)_2)_4$ along with the high melting point of trioctylphospine oxide renders the reaction protocol rather complex and therefore limits its wider applications.

This chapter focuses on the synthesis and surface modification protocol of HfO_2 nanoparticles for fabricating blue-emitting nanocomposite γ-ray scintillators. Using a single precursor of $Hf(CF_3COO)_4$ in oleylamine, highly soluble HfO_2 nanoparticles are synthesized at multi-gram scales with yield typically around 90%. The as-synthesized nanoparticles are then modified with bis(2-(methacryloyloxy)ethyl) phosphate (**BMEP**) to endow it with surface vinyl groups, which provides bonding between the nanoparticles and matrix during polymerization and therefore improves dispersion uniformity of the resulting nanocomposites. Based on the commonly used matrix/primary dye/wavelength shifter recipe of PVT/2-(4-*tert*-butylphenyl)-5-(4-biphenylyl)-1,3,4-oxadiazole (**PBD**)/1,4-bis(5-phenyl-2-oxazolyl)benzene (**POPOP**),[90] highly transparent nanoparticle/PVT/PBD/POPOP nanocomposite scintillators have been synthesized by *in situ* polymerization of vinyltoluene (**VT**) solutions containing surface-modified HfO_2 nanoparticles, PBD and POPOP. The resulting nanocomposite monoliths exhibited high optical transparency at

high nanoparticle loading. With the nanocomposite scintillator, a full energy photopeak was detected with energy resolution < 8% for the 662 keV Cs-137 γ radiation.

2.2 Experimental Section

2.2.1 Materials

Hafnium(IV) tetrachloride (99%, 80 mesh) and 1,1-di-(*tert*-butylperoxy)-3,3,5-trimethylcyclohexane (Luperox-231, 75% solution in aromatic free mineral spirit) were purchased from Acros Organics. Oleylamine (Technical grade, 70%), bis(2-(methacryloyloxy)ethyl) phosphate (BMEP), methylstyrene (commonly referred to as vinyltoluene, VT, 99%), 2-(4-*tert*-butylphenyl)-5-(4-biphenylyl)-1,3,4-oxadiazole (PBD, 99%), and 1,4-bis(5-phenyl-2-oxazolyl)benzene (POPOP) were purchased from Sigma Aldrich. Trifluoroacetic acid (99%) was purchased from EMD. Excluding chloroform (HPLC grade), all other solvents used were of ACS grade. Tetrahydrofuran was distilled from sodium benzylphenone ketyl prior to use. VT was purified by a mini column packed with inhibitor removers to remove *tert*-butylcatechol before use. An Eljen-212 general-purpose plastic scintillator was obtained from Eljen Technology and was polished into a disk with dimensions 10 mm in diameter and 2 mm thickness to serve as the standard for scintillation measurements. All other materials were used as received.

2.2.2 Synthesis and fabrication

$Hf(CF_3COO)_4$ was synthesized following the protocol for $Zr(CF_3COO)_4$ previously described by Sartori *et al.*[91] Trifluoroacetic acid (50.0 mL, *ca.* 650 mmol) was slowly added to $HfCl_4$ (30 mmol, 9.60 g) under stirring. The mixture was stirred at 40 ^oC for 5 hours and then dried by rotary

evaporation and high vacuum to obtain $Hf(CF_3COO)_4$ in the white solid form. Typical yield of the reaction is > 96%.

The high-temperature synthesis of HfO_2 nanoparticles from $Hf(CF_3COO)_4$ was carried out under inert gas protection. In a typical reaction, $Hf(CF_3COO)_4$ (4 mmol, 2.52 g) was mixed with oleylamine (52.6 mL, *ca.* 160 mmol) and stirred under vacuum for 30 min at 110 ^oC. The resulting transparent solution was then heated to 330 ^oC for 1 hour under Ar, after which the nearly-colorless transparent solution was cooled to room temperature. White HfO_2 nanoparticles were flocculated by adding 150 mL acetone, collected by centrifugation, and washed (re-dissolving and flocculating with toluene and ethanol, respectively) three times. Finally, the nanoparticles were dissolved in 20 mL toluene to form a stable colorless stock solution of around 45 mg/mL (weight concentration includes surface ligand), corresponding to a yield of about 90% after accounting for the 82% net inorganic weight as determined through thermogravimetric analysis.

Surface modification of the nanoparticles was carried out by admixing the as-prepared HfO_2 with a predetermined amount of BMEP in chloroform and stirring overnight. The resulting solution was first concentrated using rotary evaporation, then washed three times with hexane and acetone following the similar redissoving-flocculating procedure described above. The washed nanoparticles were dissolved in a nanocomposite precursor solution composed of 2 wt% PBD, 0.01 wt% POPOP and 1 vol% Luperox-231 in purified VT. The clear solution was placed in 10 mm diameter glass vials and cured (100 ^oC, 24 hours) in a nitrogen protected glove box. After curing, the resulting monoliths were removed from the glass vials and polished for further characterizations.

2.2.3 Characterization

Transmission electron microscopy (**TEM**) was performed on an FEI T12 Quick CryoEM and CryoET microscope operated at 120 keV. High resolution TEM images were taken on an FEI Titan S/TEM operated at 300 keV. The nanocomposite thin-film TEM samples were prepared by focused ion beam etching of the monolith using an FEI Nova 600 SEM/FIB system. Powder X-ray diffraction (**XRD**) data was obtained using a Panalytical X'Pert Pro X-ray powder diffractometer with Cu Kα radiation. Fourier transform infrared (**FTIR**) spectra were obtained using a Jasco 420 FTIR spectrophotometer with KBr pelletized samples. Dynamic light scattering was performed on a Coulter Beckman N4 Plus Dynamic Light Scattering Analyzer. UV-visible tests were carried out on a Shimadzu UV-1700 spectrophotometer. Homemade masks were applied to reduce the light path variations for monolith transmittance tests. Photoluminescence spectra were obtained with a PTI QuantaMaster 30 spectrofluorometer. Thermogravimetric analysis (**TGA**) was performed on a Perkin Elmer Diamond Thermogravimetric/Differential Thermal Analyzer. The sample was first stabilized at 100 ^{o}C for 10 min to remove residue solvents and water before being heated to 850 ^{o}C in air at a ramping rate of 15 ^{o}C/min, after which it was kept at 850 ^{o}C for another 10 min to ensure complete decomposition. Energy dispersive X-ray (**EDX**) spectroscopy was performed on an FEI Nova Nano 230 scanning electron microscope operated at 10 keV. The EDX samples were first dispersed in corresponding solvents and drop-casted onto Cu tape, followed by high-vacuum drying.

2.2.4 Gamma pulse height analysis of the monoliths

Gamma pulse height analysis was performed with a home-built system in a dark box as shown in **Figure 2.2**, where a Cs-137 source (662 keV characteristic γ energy) of 4.68 μCi activity (1.7 x 10^5 disintegrations/second) was placed right in front of the nanocomposite monolith coupled to a Hamamatsu R878 PMT using optical grease. A set of customized Teflon reflector ring and back-reflector disk was used to optimize the light collection by PMT and to exclude the influence of concomitantly emitted β rays from the Cs source. The PMT was equilibrated for 30 min after sealing the dark box. Typical acquisition live time was set to one hour unless specified otherwise. The signal was read out by a Canberra multichannel analyzer with rise and flat top times set to 1 μs and 0.5 μs, respectively.

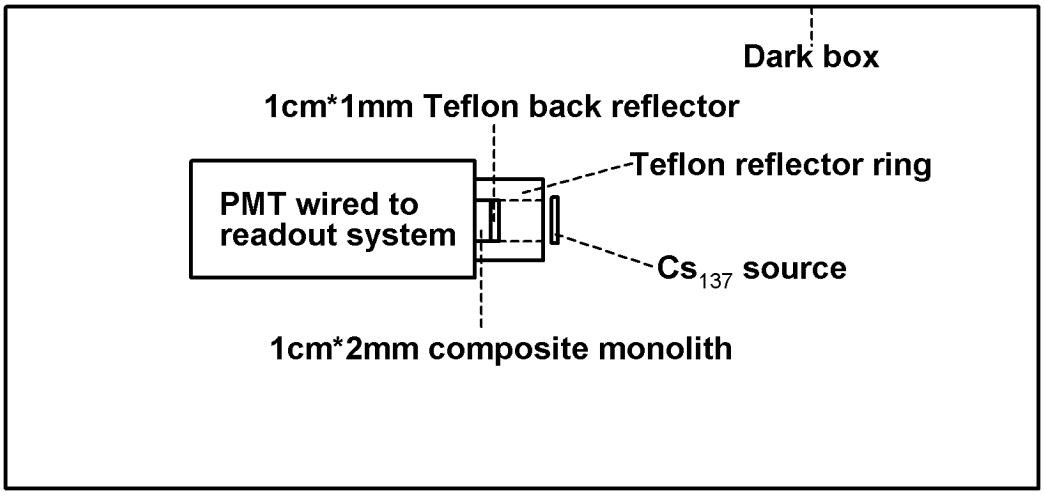

Figure 2.2 Gamma pulse height analysis apparatus.

2.3 Results and Discussion

2.3.1 Synthesis and surface modification of HfO_2 nanoparticles

HfO_2 nanoparticles have been synthesized in a single-precursor reaction as schematically shown in **Figure 2.3**. The precursor, $Hf(CF_3COO)_4$, was first synthesized following the protocol as previously described for $Zr(CF_3COO)_4$.[91] The similar chemical properties of Hf and Zr due to Lanthanide contraction allow these reactions to proceed in virtually the same way.[92] Owing to the high reactivity of $HfCl_4$, the reaction proceeded almost stoichiometrically, producing white $Hf(CF_3COO)_4$ with yields in excess of 96%. Structure of the as-synthesized $Hf(CF_3COO)_4$ has been confirmed by FTIR (**Figure 2.4**). In addition to the C-O and C-F vibration peaks at 1200 and 1150 cm^{-1}, the peaks at 1662, 1455 and 1483 cm^{-1} also showed a good match with the bidendate COO^- anti-symmetric and symmetric vibrations of $Zr(CF_3COO)_4$ reported by H. Sutcliffe *et al*.[93] In addition, EDX shows Hf, C, O, and F signals but no Cl, confirming a complete reaction between $HfCl_4$ and CF_3COOH. The precursor is stable in air, and can be stored for months in a sealed flask without obvious signs of degradation.

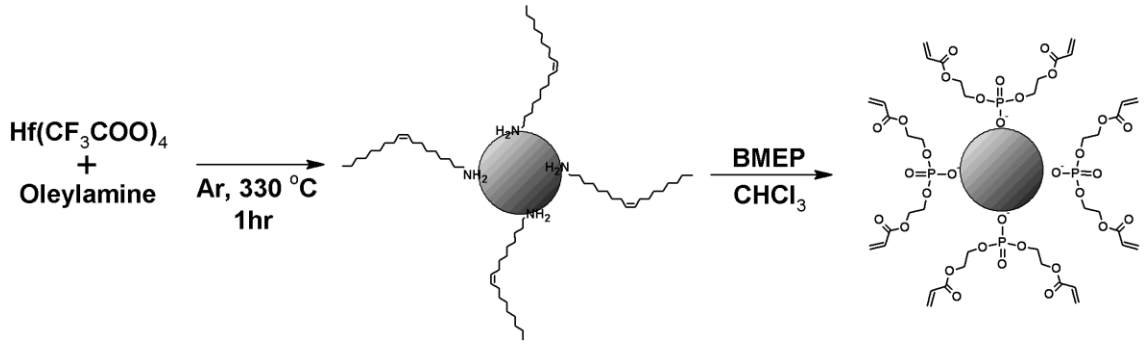

Figure 2.3 Schematic of single-precursor synthesis and surface modification processes of HfO_2 nanoparticles.

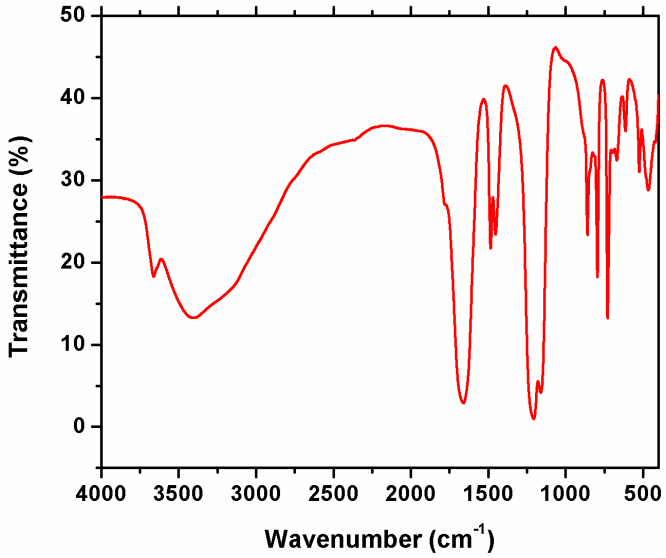

Figure 2.4. FTIR spectrum of $Hf(CF_3COO)_4$ in KBr pellet.

The as-synthesized $Hf(CF_3COO)_4$ was then used to synthesize HfO_2 nanoparticles capped with oleylamine in an air-free setup resembling a number of other high-temperature nanoparticle syntheses.[44,48] The reaction yield has been determined to be around 90%, indicative of the high efficiency of this single-precursor method. TEM image of the as-synthesized HfO_2 nanoparticles shows a quite uniform size distribution around 5 nm, with most nanoparticles having nearly round shape (**Figure 2.5**). This size distribution is further confirmed by the dynamic light scattering results of a 45 mg/mL nanoparticle solution in toluene. X-ray diffraction (**XRD**) pattern of the dried HfO_2 nanoparticles (**Figure 2.5**) matched well with the JCPDS profile 00-006-0318 for monoclinic HfO_2, confirming the crystallinity of HfO_2 nanoparticles. It is well known that nano-sized crystals can cause line broadening in the XRD pattern, and the Scherrer equation can be used to calculate crystallite size from line broadening:

$$\tau = \frac{K\lambda}{\beta \cos\theta} \tag{2.1}$$

where $\boldsymbol{\tau}$, $\boldsymbol{K}$, $\boldsymbol{\lambda}$, $\boldsymbol{\beta}$ and $\boldsymbol{\theta}$ are crystallite size, shape factor (typically around 0.9), wavelength of the X-ray (0.154 nm for Cu Kα1), full-width-half-maximum (**FWHM**) of the broadened line, and the Bragg angle for the diffraction peak, respectively. After stripping the Cu Kα2 signal from the spectrum and accounting for the instrumental broadening of 0.07°, crystallite sizes were calculated to be 6.0 nm and 5.3 nm for the (-111) and (111) planes, respectively, showing a close match to results obtained from the TEM images.

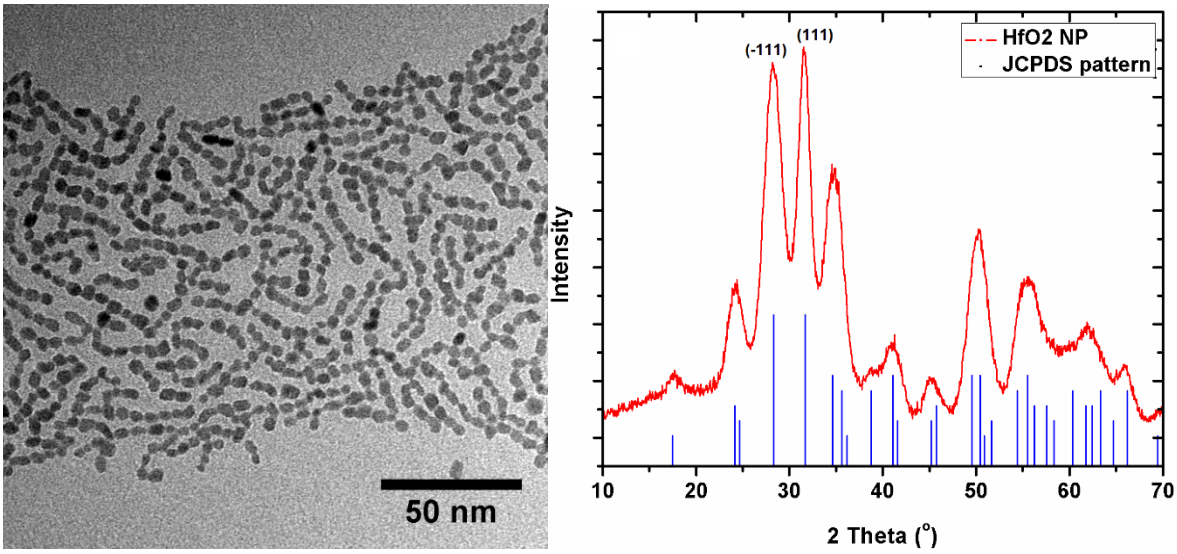

Figure 2.5 TEM image **(left)** and powder XRD pattern **(right)** of HfO_2 nanoparticles.

To determine the mechanism behind HfO_2 nanoparticle formation, a series of synthetic tests were performed under various concentrations of $Hf(CF_3COO)_4$. As shown in **Figure 2.6**, the product HfO_2 nanoparticles show no obvious crystallinity differences at $Hf(CF_3COO)_4$/oleylamine molar ratios of 1:40 and 1:20, whereas the crystallinity decreased slightly for the 1:160 reaction, most likely due to an insufficient supply of precursors. For the $Hf(CF_3COO)_4$/oleylamine = 1:20 experiment, the viscosity of reaction mixture drastically increased at around 290 °C, leading to a gel-like appearance. Moreover, upon further increasing the temperature to 330 °C, the mixture eventually achieved the characteristic colorless, low-viscosity solution typical of the reaction. This

observation indicates that the reaction may follow a sol-gel process where oleylamine first attacks the trifluoroacetate ligand to form Hf-OH, followed by condensation to form HfO_2 nanoparticles. The initial increase of viscosity at 290 ^oC could be ascribed to the formation of partially condensed loose networks of Hf-O-Hf, which is incapable of dissolving in limited amounts of oleylamine, and merely swells to form a gel. Further increasing the degree of condensation led to the formation of suspended dense nanoparticles, thus reducing the viscosity. This mechanism can be further corroborated by the failed reactions using oleic acid instead of oleylamine. Since the formation of Hf-OH was prevented in the first place by the acidic environment in oleic acid, no crystals could be obtained, but a yellow oil was produced. A detailed study on the formation mechanism of HfO_2 nanoparticles will be presented in Chapter 3, along with studies on ZrO_2 and TiO_2.

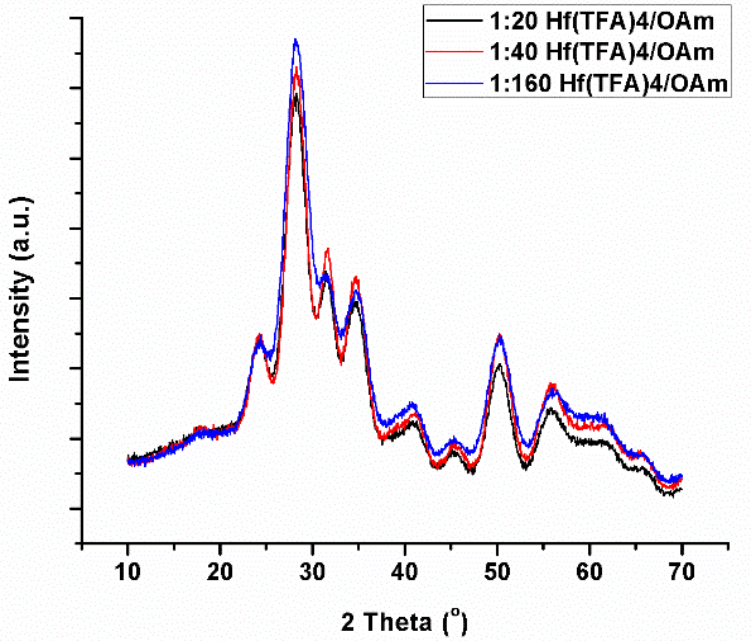

Figure 2.6 XRD patterns of HfO_2 obtained with different molar ratios between $Hf(CF_3COO)_4$ and oleylamine.

The as-synthesized nanoparticles were assumed to be coated by a layer of oleylamine due to their excellent solubility in low-polarity solvents, which was confirmed by the FTIR spectrum of

unmodified HfO_2 nanoparticles shown in **Figure 2.7**. The peaks at 1620 cm^{-1} and 3001 cm^{-1} can be ascribed to the C=C and vinyl C-H vibrations for oleylamine, respectively.[94] The N-H bending vibrations at 1514 cm^{-1} and stretching band at around 3200 cm^{-1} also indicate the presence of oleylamine, whereas the lack of peaks at 1000 – 1250 cm^{-1} excludes the possibility of remaining carboxylic acid bonding to the surface.

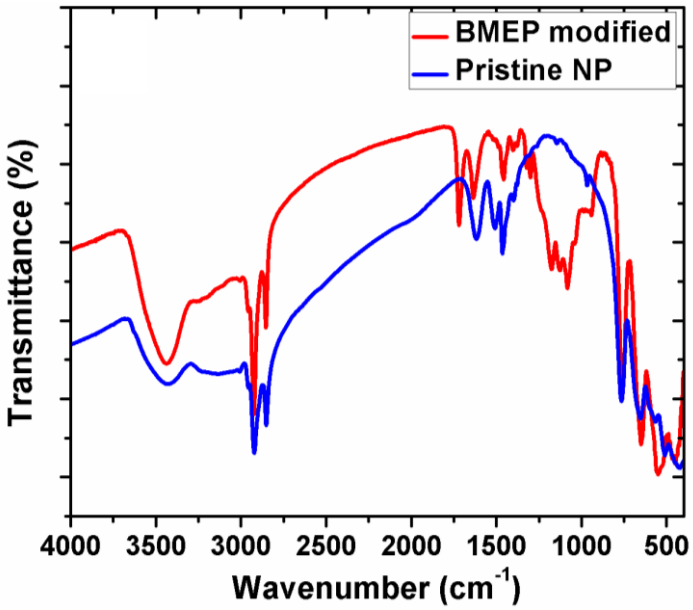

Figure 2.7 FTIR spectra of HfO_2 nanoparticles before and after BMEP exchange.

The oleylamine ligands bound on nanoparticle surface have unsaturated C=C bonds. These vinyl groups are relatively unreactive and cannot be readily co-polymerized with vinyl monomers such as VT to provide bonding between the nanoparticles and a PVT matrix. Therefore, direct curing of VT solutions containing oleylamine-capped nanoparticles resulted in severe phase separations and thus transmittance loss due to exclusion of nanoparticles during polymerization. Since the visible photons generated within the scintillator monolith need to transmit through the bulk and be detected by PMT, it is crucial to reduce phase separation and transmittance loss to improve the detection efficiency. BMEP was then used to introduce methacrylate monomer groups onto the

nanoparticle surface to promote copolymerization with the matrix.[71] The suitable reactivity ratios (ratios between possibilities of one monomer reacting to itself vs. to the other in a binary copolymerizing system) of 0.52 and 0.46 for styrene and methyl methacrylate, respectively, promise a good chance of copolymerization between VT and the methacrylate-containing BMEP, rendering BMEP a suitable surface modifier.[59] Strong bonding between hafnium and phosphate guarantees a strong anchoring of BMEP surface layer, while the acid-inert nature of bulk HfO_2 assured an intact crystallinity of HfO_2 nanoparticles after ligand exchange.[92] **Figure 2.7** compares the FTIR spectra of pristine HfO_2 nanoparticles and fully BMEP-exchanged HfO_2 nanoparticles. The previously described spectral features of oleylamine coated HfO_2 nanoparticles disappeared after BMEP exchange. Instead, a set of new peaks appeared at 1716 cm^{-1}, 1633 cm^{-1}, 1173 cm^{-1}, 1114 cm^{-1}, and 1078 cm^{-1}, corresponding to the C=O, C=C, C-O and P-O stretching absorptions.[71] These obvious changes in spectral features confirm the effectiveness of surface modification using BMEP.

Due to the strong bonding between hafnium and phosphate, the reaction between BMEP and HfO_2 nanoparticles should be able to proceed almost stoichiometrically.[92] This has been confirmed by the FTIR and TGA results of pristine and BMEP-modified HfO_2 nanoparticles at different BMEP-exchange ratios (**Figure 2.8**). The FTIR results show that, as the BMEP content increases, the N-H bending and stretching absorptions at 1514 cm^{-1} and 3200 cm^{-1} decrease and eventually disappear at an excess amount of 28 mg BMEP / 100 mg nanoparticle, indicating a gradual replacement of oleylamine by BMEP. Moreover, a decrease in weight loss with an increasing degree of ligand exchange is observed in TGA, which is consistent with the smaller organic content in BMEP (total: 322.25 g/mol; PO_4 excluded: 226.27 g/mol) than oleylamine (267.49 g/mol). In

addition, the measured weight losses after BMEP modification also match well with the weight losses calculated under the estimation of stoichiometric BMEP exchanges (**Table 2.1**). It should be noted that using an excess amount of BMEP would not result in more BMEP attachment than that limited by the available surface states, indicating a good stability of HfO_2 nanoparticles against corrosion by acids, which is further confirmed by the unchanged XRD pattern after BMEP modification (**Figure 2.9**). Therefore, the degree of surface modification can be controlled by varying the amount of BMEP used. The solubility of BMEP-exchanged nanoparticles in VT was found to decrease with an increasing degree of BMEP exchange, likely due to the higher polarity of BMEP than oleylamine. However, excessively low percentages of BMEP exchange would result in insufficient bonding between the matrix and nanoparticle and thus lead to phase segregation and transmittance loss. HfO_2 nanoparticles exchanged with 50% BMEP (1:1 molar ratio of oleylamine/BMEP on the modified nanoparticles) were found to be optimal in balancing between the solubility and surface monomer density; this percentage would be used in all nanocomposite fabrications thereafter.

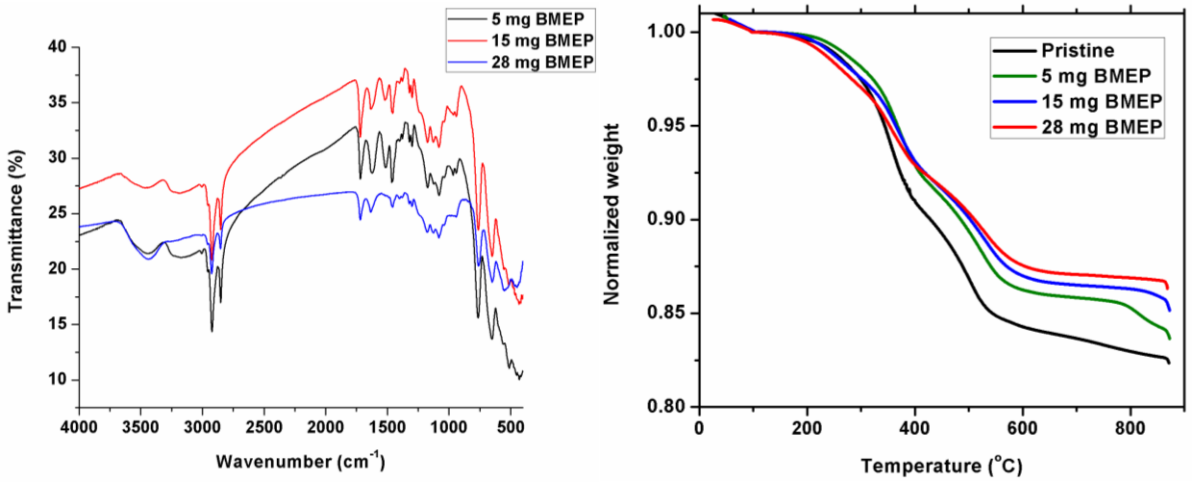

Figure 2.8 FTIR spectra (**left**) and TGA curves (**right**) of pristine and BMEP-modified nanoparticles. The modification reactions were carried out using 100 mg HfO_2 nanoparticles and different amounts of BMEP.

Table 2.1 TGA and calculated weight losses of pristine and BMEP-modified HfO_2 nanoparticles.

BMEP Weight / mg	Mol. Equiv.	Calc. Weight Loss	Exp. Weight Loss
0 (Pristine)	-	-	0.178
5	0.233	0.167	0.165
15	0.699	0.150	0.149
28 (All BMEP attached)	1.304	0.178	0.138
28 (No further attachment beyond 1 equiv.)	1	0.145	0.138

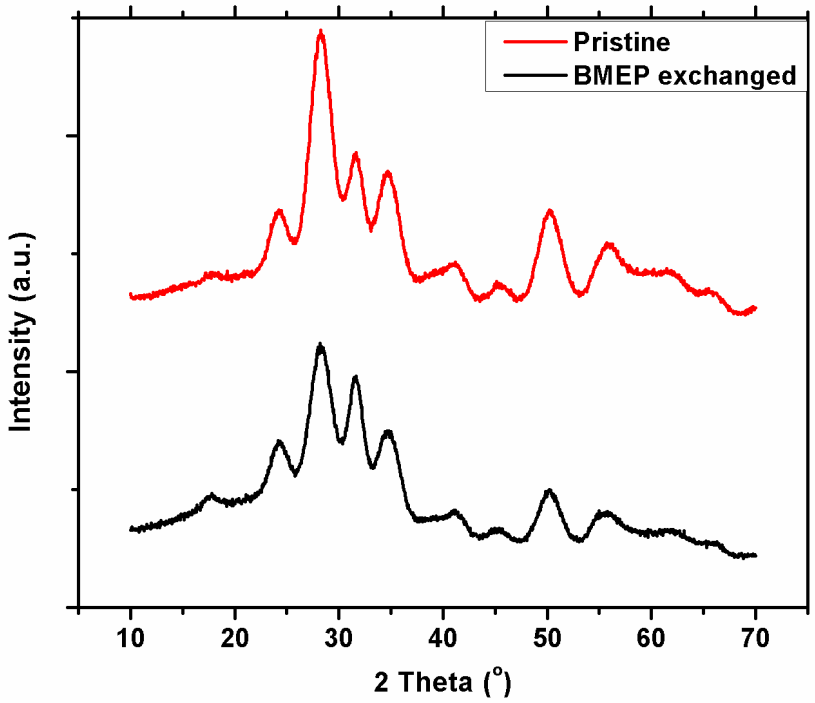

Figure 2.9 XRD patterns for pristine and BMEP-modified HfO_2 nanoparticles.

As stated above, an important reason for choosing HfO_2 as the high-Z component is that its large band gap prohibits matrix-to-nanoparticle exciton energy transfer, thus avoiding excess exciton quenching. To confirm HfO_2's large band-gap, optical absorbance of both pristine and BMEP-

modified HfO_2 nanoparticles were tested using UV-visible spectroscopy. Due to the decreased solubility of BMEP-modified nanoparticle in hexane, distilled tetrahydrofuran (no optical absorption at > 210 nm) was used to dissolve both samples for the spectroscopic measurement. **Figure 2.10** shows the absorption spectra of these nanoparticles at concentration of 0.5 mg/mL. The absorption peak at 240 nm for pristine nanoparticles is consistent with the reported absorption for oleylamine,[95] whereas the absorption onset at 230 nm for BMEP-modified nanoparticles matched well with the measurement of a 0.05 mg/mL BMEP solution. No other strong absorption was observed above 215 nm for both nanoparticles, indicating a band gap of at least 5.7 eV, which would be more than sufficient to prevent exciton transfer from PVT to nanoparticles. The 50%-BMEP-modified HfO_2 nanoparticles showed no obvious degradation of solubility in VT compared to the pristine nanoparticles, as indicated by the colorless transparent solutions of 20 wt% pristine and modified nanoparticles in VT (see inset of **Figure 2.10**).

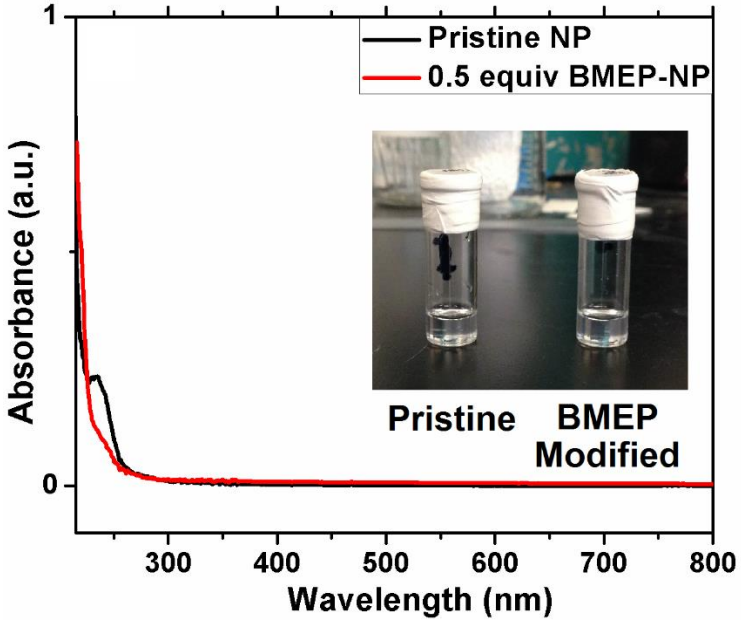

Figure 2.10 UV-vis absorption spectra of pristine and BMEP-exchanged HfO_2 nanoparticles in dry tetrahydrofuran (Inset: a picture of 20 wt% pristine and BMEP exchanged HfO_2 nanoparticle solutions in VT prior to curing).

2.3.2 Synthesis of HfO_2-nanoparticle-based nanocomposite scintillator

Using the highly soluble BMEP-modified HfO_2 nanoparticles, nanoparticle/PVT/PBD/POPOP nanocomposite monoliths were fabricated using a thermally-initiated bulk polymerization process.[71] **Figure 2.11A** shows the TGA curve of a 20 wt% nanoparticle composite tested in air (all nanoparticle concentrations are wt% including the organic ligand content henceforth, if not specified). The remnant of 16.5% matches well with the estimation of 20% * (1-0.16) = 16.8%, where 20% is the initial nanoparticle loading, with the organic ligand content of nanoparticles being 16% as determined previously. The nanoparticle nanocomposites displayed high transparency after curing. **Figure 2.11B** shows the transmittance curves and photos of a 2-mm 20% nanoparticle nanocomposite along with its nanoparticle-free counterpart. No obvious transparency differences are evident from visual inspection. On the spectra, the sharp drop at 400 nm is due to POPOP absorption. The 20% nanoparticle nanocomposite showed a slightly lower transmittance compared to its nanoparticle-free counterparts above 400 nm. Compared with the relatively flat curve for nanoparticle-free composite ($T_{550\ nm}$ = 90.9%, $T_{415\ nm}$ = 88.6%), transmittance of the nanoparticle nanocomposite degraded faster with decreasing wavelength ($T_{550\ nm}$ = 83.7%, $T_{415\ nm}$ = 72.9%). This can be attributed to an intensified Rayleigh scattering induced by the presence of nanoparticles, as the transmittance loss due to scattering is strongly wavelength dependent ($\propto \exp(-C/\lambda^{-4})$, where C is a material property related constant).[78,81] Moreover, it is suspected that the nanoparticles could still aggregate, but to a smaller extent, during polymerization, since the gradual formation of polymer network would still lead to some degree of nanoparticle exclusion. To confirm this, TEM images were obtained on a thin-film sample (about 50 nm thick) of the 20% nanoparticle nanocomposite prepared using focused ion beam. As shown in **Figure 2.11C**,

although the nanoparticle dispersion was fairly uniform within the polymer matrix, some nanoparticles aggregate into clusters of about 20 to 30 nm sizes, which could be the major source of scattering-induced transmittance loss. It should be noted that the thin film of 50 nm could contain several layers of nanoparticles, which might lead to some degree of overestimation on the aggregation effect due to the possibility of overlapped nanoparticles in the TEM image.

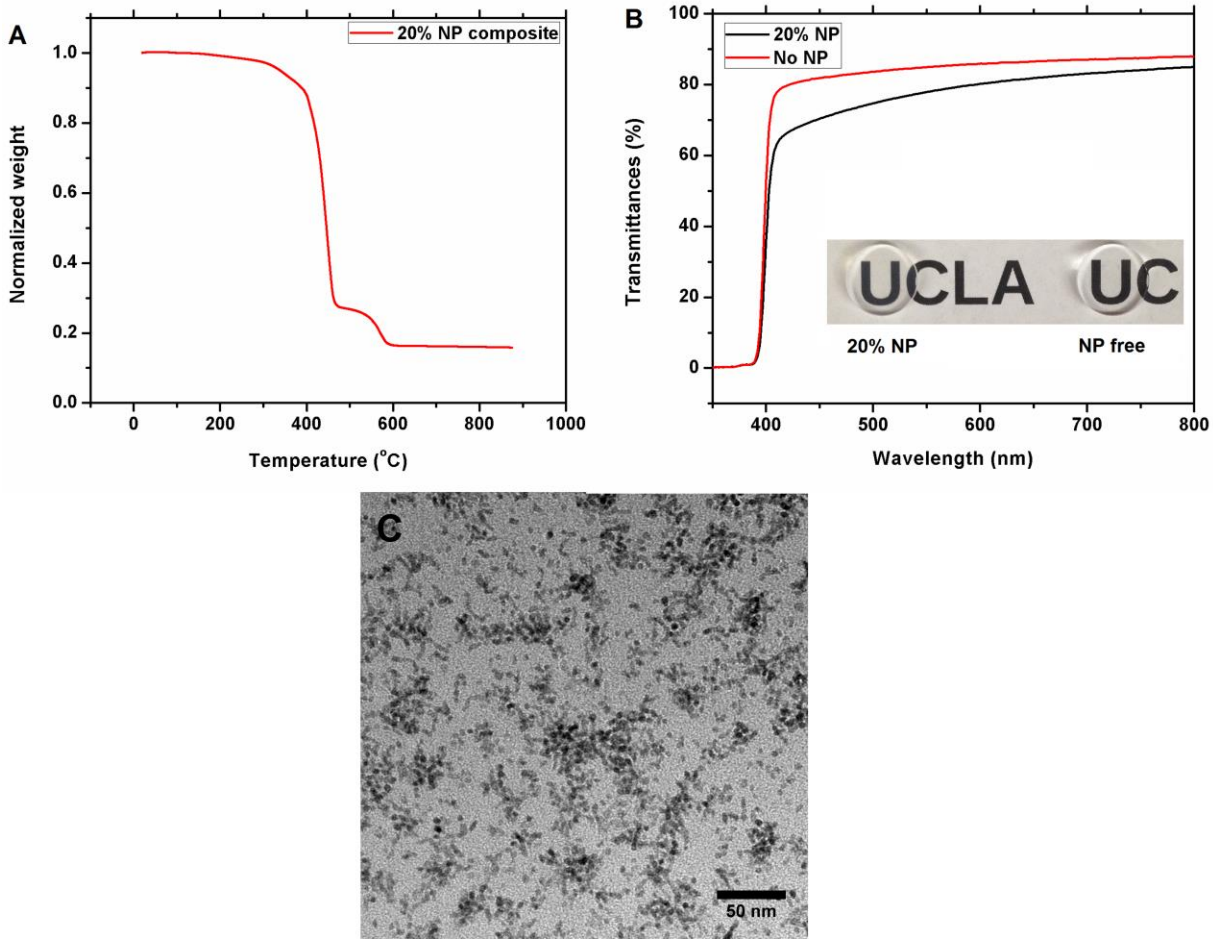

Figure 2.11 TGA curve **(A)** of a 20% nanoparticle/PVT/PBD/POPOP composite monolith; UV-vis transmittance curves **(B)** and pictures of 2-mm-thick nanoparticle-free and 20% nanoparticle/PVT/PBD/POPOP composite monoliths; and TEM image **(C)** of an FIB-etched thin film of 20% nanoparticle composite.

2.3.3 Photophysics characterization of nanocomposite scintillators

As mentioned before, HfO_2 nanoparticles in the nanocomposite will serve as high-Z component to convert an incident γ photon into a single photoelectron with all energy in the original γ photon. The high-energy photoelectron then undergoes energy cascade within the PVT matrix by colliding with other electrons on its decay path, where a number of excitons are produced in proportion to the photoelectron energy. Through fluorescence resonance energy transfer (FRET), these excitons will migrate to the PBD dye sites and be converted into visible photons for detection. This energy transfer process needs to be highly efficient to maximize light yield (number of photons generated per MeV of γ energy), since the fluorescence quantum efficiency of PVT is very low. In addition to the primary dye of PBD, POPOP is used as a wavelength shifter at very low concentration (0.01%) to further shift PBD's emission in order to reduce self-absorption.[2,25,90] The combination of PVT/2% PBD/0.01% POPOP has been widely reported to have a good light yield and therefore was used for the nanocomposite scintillators in this work.[25,90]

To confirm the aforementioned energy transfer processes, a photophysics study was performed using photoluminescence spectroscopy. **Figure 2.12** shows the photoluminescence spectra of a monolith of neat PVT, dilute solutions of PBD and POPOP, and a 20% nanoparticle/PVT/PBD/POPOP nanocomposite monolith. The emission maximum of PVT at 311 nm matches the excitation of PBD, while PBD's emission maximum at 365 nm overlapped nicely with the excitation of POPOP. These well-matched emission/excitation pairs promise efficient FRET transfers from PVT to PBD and finally via radiative transfer to POPOP. As shown in **Figure 2.12D**, the 20% nanoparticle/PVT/2% PBD/0.01% POPOP nanocomposite exhibited only POPOP emission at the PVT excitation wavelength of 298 nm, confirming an efficient energy transfer

process. The inset of **Figure 2.12D** shows the picture of a nanoparticle-free and a 20% nanoparticle/PVT/PBD/POPOP nanocomposite monoliths under 256 nm UV illuminations, where no discernable differences in the emission color and intensity could be observed.

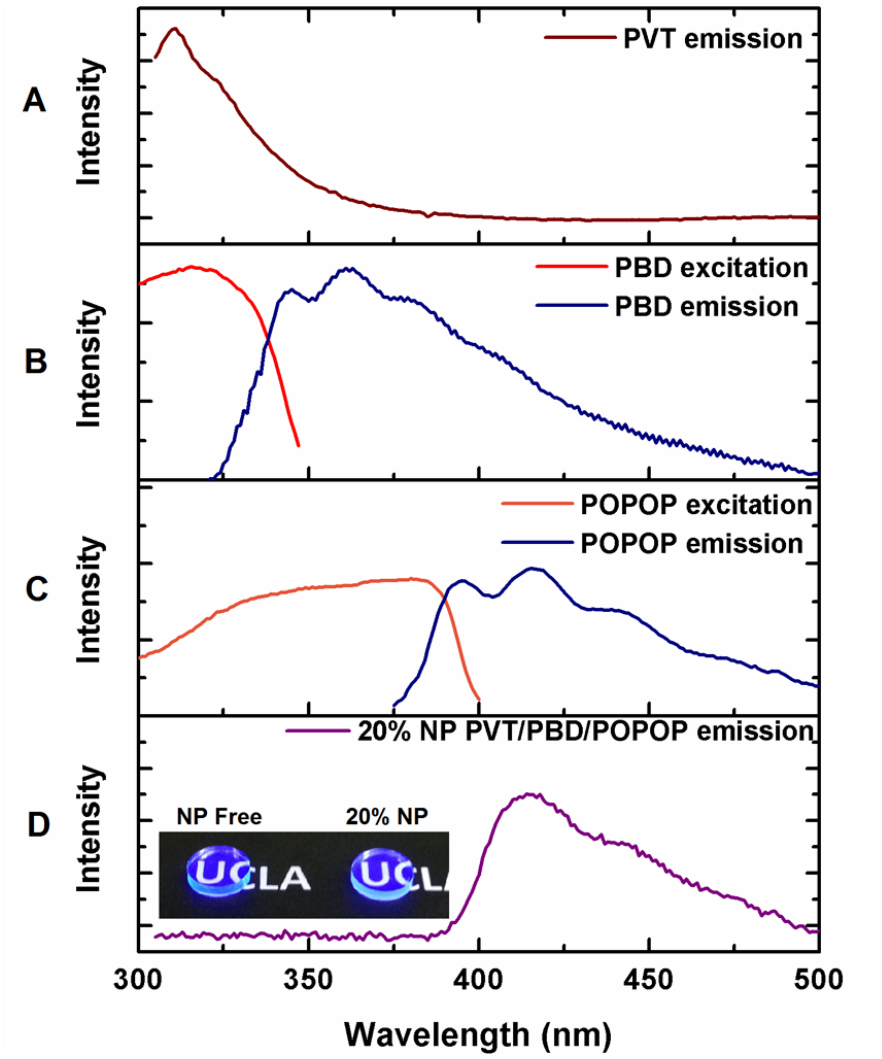

Figure 2.12 Photoluminescence spectra of **(A)** pure PVT monolith, **(B)** dilute PBD/$CHCl_3$ solution, **(C)** dilute POPOP/$CHCl_3$ solution, and **(D)** 20% nanoparticle/PVT/PBD/POPOP nanocomposite monolith (Inset: PVT/PBD/POPOP monoliths (2 mm thick by 1 cm diameter) containing zero (left) and 20% nanoparticles (right) under 256 nm UV illumination). The excitation wavelengths used for taking emission spectra were 298 nm, 311 nm, 365 nm, and 298 nm for PVT, PBD, POPOP, and the 20% nanoparticle nanocomposite, respectively. The excitation spectra were obtained by measuring the emission intensity at 365 nm and 415 nm for PBD and POPOP, respectively.

2.3.4 Gamma response of HfO_2-nanoparticle-based nanocomposite scintillator

Gamma responses of the blue-emitting nanocomposites were characterized using a homebuilt gamma pulse height analysis system. Pulse height spectra were first obtained on three samples including a nanoparticle-free PVT/PBD/POPOP nanocomposite, a 20% nanoparticle PVT/PBD/POPOP nanocomposite, and an Eljen-212 commercial plastic scintillator polished to the same size as the nanocomposite monoliths. **Figure 2.13A** shows the pulse height spectra obtained for these three samples. The appearance of a Compton edge is due to the Compton backscattering of gamma photons, and its position depends solely on the energy of the incident gamma photon.[1] For 662 keV γ, the Compton edge corresponds to a deposited energy of 478 keV. Therefore, using the channel number of Compton edge (typically chosen as the inflection point on the slope), the γ light yields of these three monoliths can be compared. The channel numbers for the Compton edges of Eljen-212, nanoparticle-free composite, and 20% nanoparticle nanocomposite were 1110, 1100 and 840, respectively. With the light yield of Eljen-212 being 10000 photons/MeV, the light yields of nanoparticle-free and 20% nanoparticle nanocomposites would be 9900 and 7600 photons/MeV, respectively. The similar light yield of PVT/PBD/POPOP with Eljen-212 is consistent with previous reports.[25,90] However, the decrease in light yield with nanoparticle inclusion may not be due to exciton quenching as reported in literatures using organometallics as the high-Z component, since the nanoparticles possess a much larger band gap than the organic components and therefore cannot capture and trap the low energy excitons and photons from the organics.[33,38] Nevertheless, a plausible case might be that the energy deposited within HfO_2 during photoelectron cascade could be trapped and dissipated without producing photons, leading to degradation in the composite's overall photon generation power and thus light

yield. In addition, a more obvious reason behind light yield deterioration is the loss of transmittance due to scattering induced by nanoparticles, which affects the efficiency of photons generated inside the monolith being out-coupled to the PMT.

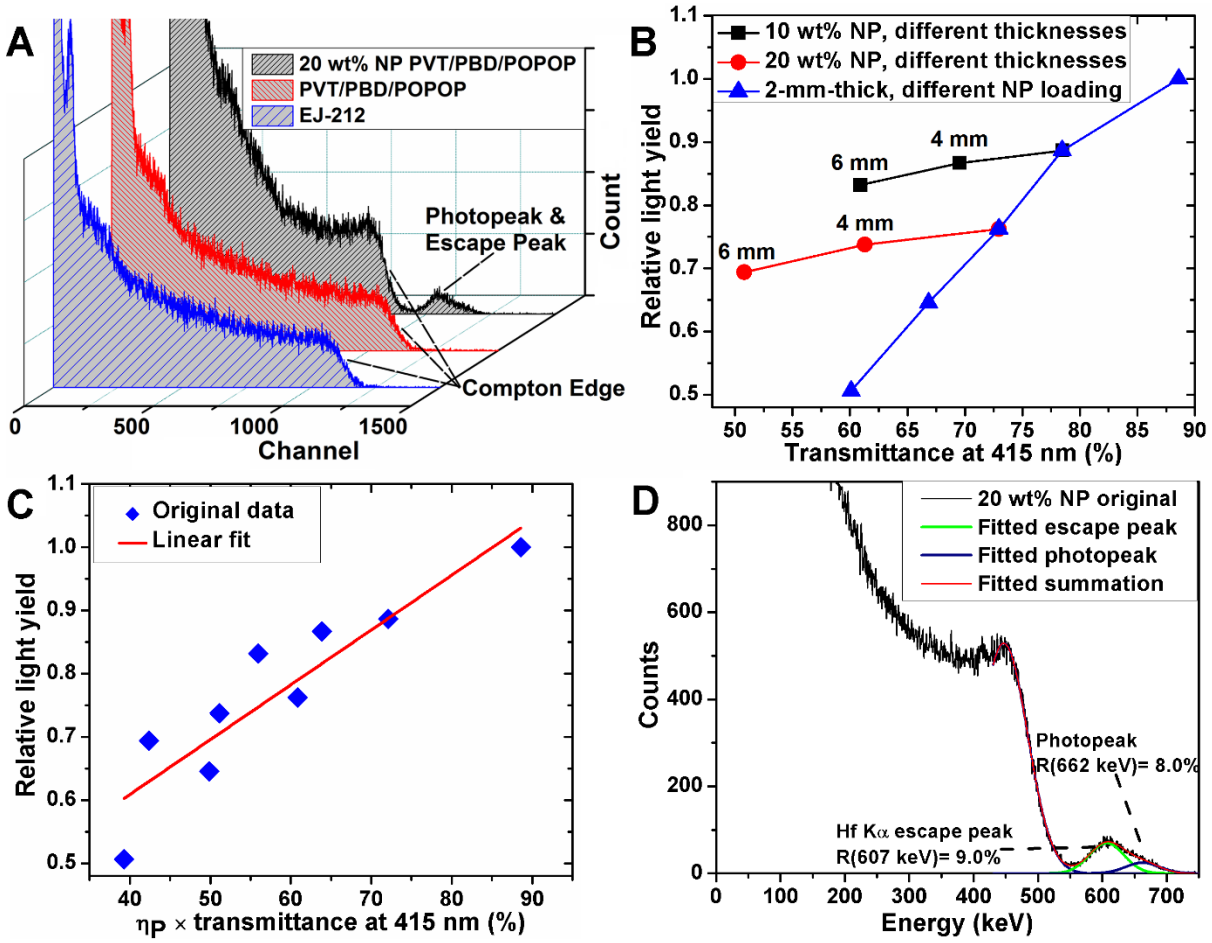

Figure 2.13 Pulse height spectra **(A)** obtained for monoliths of PVT/PBD/POPOP, 20% nanoparticle/PVT/PBD/POPOP and the standard Eljen-212 scintillator; **(B)** relative light yield vs. transmittance at 415 nm for 10% and 20% nanoparticle composites with different thicknesses (2, 4 and 6 mm), and for 2-mm-thick monoliths with 0% to 40% nanoparticle with 10% increment; **(C)** relative light yield re-plotted and linearly fitted as a function of the product of relative photon generation power (η_P) and transmittance at 415 nm for data points in **(B)**; and **(D)** energy correlated pulse height spectrum and fitted curve for a 2-mm-thick 20% nanoparticle PVT/PBD/POPOP monolith.

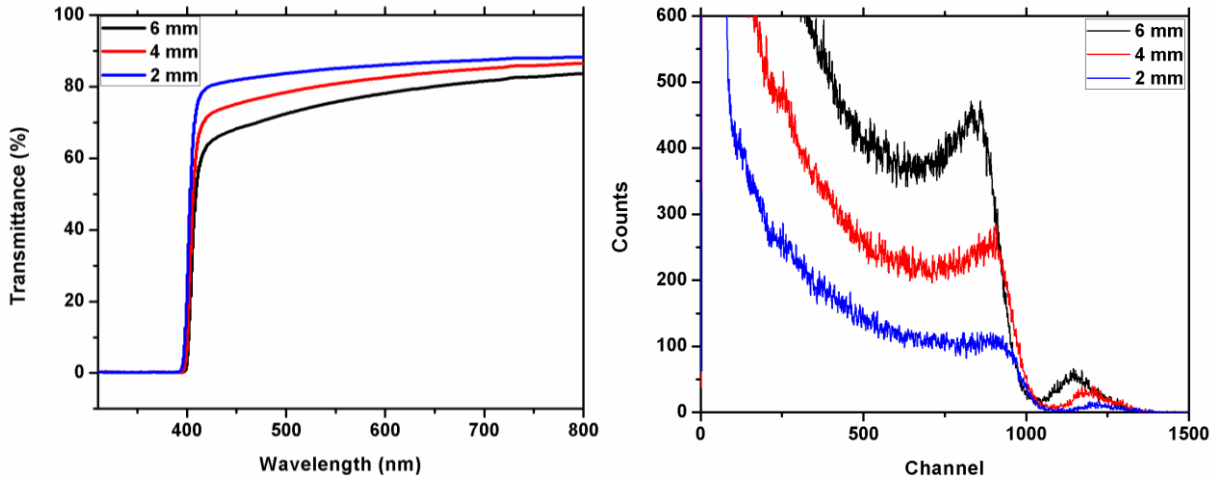

Figure 2.14 Transmittance curves (left) and pulse height spectra (right) of 10 wt% nanoparticle PVT/PBD/POPOP monoliths with different thicknesses.

In order to investigate these causes of light yield deterioration, three sets of experiments have been performed. The first two sets used 10% nanoparticle and 20% nanoparticle PVT/PBD/POPOP monoliths, respectively, at different thicknesses (2, 4 and 6 mm) to determine the effect of transmittance on light yield. In the third set, a series of 2-mm-thick monoliths with 0% to 40% nanoparticle loadings were tested, where the combined effects of transmittance loss and energy trapping in nanoparticles on light yield could be observed. Relative light yields of the samples were obtained by dividing their Compton edge channel numbers by that of the 2-mm-thick PVT/PBD/POPOP monolith. To characterize the light out-coupling ability of monoliths, the transmittance at 415 nm was chosen as the figure of merit, since the emission maxima of nanocomposite monoliths have all been located at this wavelength as shown in **Figure 2.12**. **Figure 2.13B** shows the relative light yields and transmittances at 415 nm obtained for these monoliths (original data shown in **Figures 2.14** to **2.16**). In each curve for the 10% and 20% nanoparticle monoliths, the relative light yield showed a somewhat linear dependence on transmittance, consistent with the as-proposed effect of transmittance, or light out-coupling, on

light yield. However, for these two curves, in addition to the curve for 2-mm-thick monoliths with different nanoparticle loadings, large discrepancies in relative light yields were found amongst samples with the same transmittance but different nanoparticle%, indicating a significant influence from the nanoparticles themselves in addition to the transmittance loss.

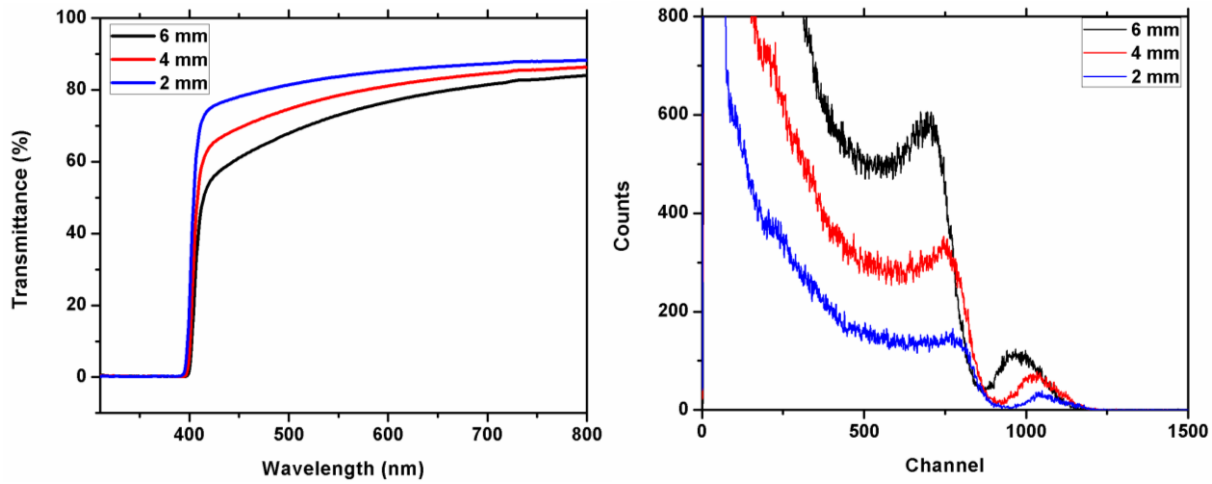

Figure 2.15. Transmittance curves (left) and pulse height spectra (right) of 20 wt% nanoparticle PVT/PBD/POPOP monoliths with different thicknesses.

As mentioned above, the nanoparticle's large band gap excludes possibilities of quenching excitons from organics and absorbing photons emitted by fluorescent dyes. A plausible mechanism behind this nanoparticle-induced extra light yield deterioration is the loss of energy trapped in nanoparticles during fast electron cascade, since the nanoparticles are not fluorescent and cannot transfer the deposited energy into the organic matrix via FRET. For a quantitative consideration, this part of trapped energy should be proportional to the volume percentage of nanoparticles multiplied by their fast electron stopping power (Note: this is still a somewhat simplified model, a more detailed discussion has been provided by Bulin *et al.* [96]). The fast electron stopping power in matter is directly proportional to that matter's electron density because a fast electron goes through energy cascade via collisions with electrons in the matter sitting in its tortuous pathway. The

organic components, PVT, PBD, and POPOP, have similar atomic compositions and thus almost identical electron densities. HfO_2 nanoparticles, on the other hand, have a much higher electron density than the organics and thus a greater stopping power for fast electron.

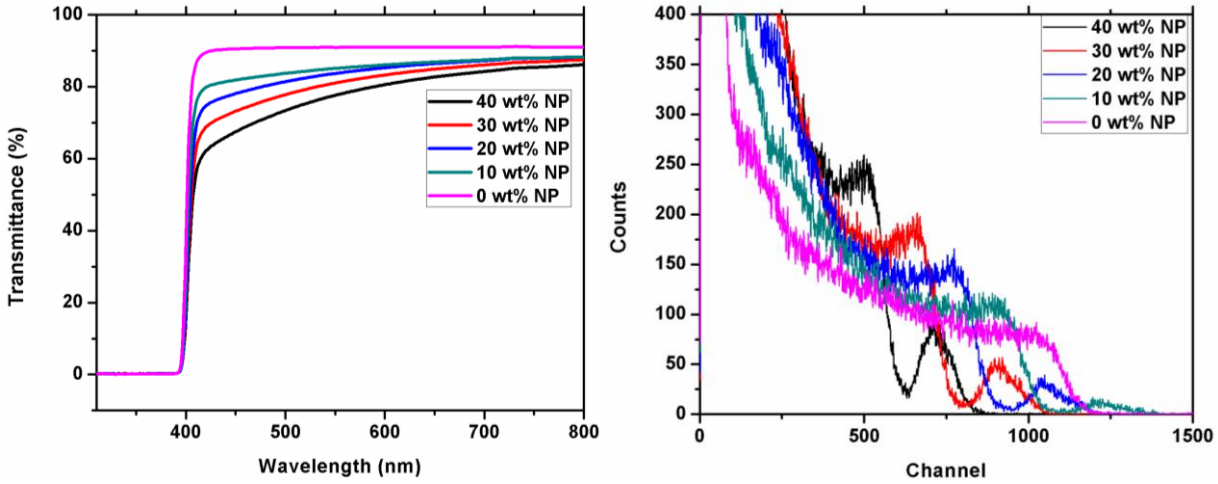

Figure 2.16 Transmittance curves (left) and pulse height spectra (right) of 2-mm-thick nanoparticle PVT/PBD/POPOP monoliths with different nanoparticle loadings.

Based on the statement above, the percentage of energy (**E*i***) deposited in component *i* in the nanocomposite can be expressed using the normalized product of stopping power (**-dE/d*x***) and volume percentage (**V**):

$$E_i = \frac{V_i(-\frac{dE}{dx})_i}{\sum_i V_i(-\frac{dE}{dx})_i} \tag{2.2}$$

The relationship between fast electron stopping power and the electron density of matter has been given by Bethe:[1]

$$-\frac{dE}{dx} \propto \frac{Z \times \rho}{A} \tag{2.3}$$

where ***Z***, ***ρ*** and ***A*** are the atomic number, volumetric mass density and relative atomic mass of the matter, respectively. Assuming all fast electron energy deposited in nanoparticles and

nanoparticle-bound ligands (which lack conjugated π-electrons for hosting excitons) dissipates without producing photons, and the energy deposited in organic matrix (including dyes) is used to generate photons, the relative photon generation power (**η_P**) is then directly proportional to the percentage of energy deposited within the organic matrix (E_M) and can be expressed as follows using (2.2) and (2.3):

$$\eta_P \propto E_M = \frac{V_M \frac{Z_M \times \rho_M}{A_M}}{V_M \frac{Z_M \times \rho_M}{A_M} + V_{NP} \frac{Z_{NP} \times \rho_{NP}}{A_{NP}} + V_L \frac{Z_L \times \rho_L}{A_L}} \tag{2.4}$$

where the subscripts M, nanoparticle and L denote matrix, nanoparticles and ligands, respectively. For each component, the volume percentage was calculated using wt% and density, whereas Z and A were taken as the total Z and relative molecular mass, respectively, e.g. $Z_{nanoparticle}$=88, $A_{nanoparticle}$=210.5 for HfO_2. From this expression, it is clear that although the volume percentage of HfO_2 nanoparticles is small compared with the organics, the amount of energy trapped during the fast electron cascades can still be significant due to the nanoparticle's much higher electron density.

The overall light yield determined by PMT depends not only on the generation but also out-coupling of the photons to the photodetector. It is thus proportional to the product of transmittance and relative photon generation power η_P. **Figure 2.13C** plots the relative light yield against the product of transmittance at 415 nm and calculated η_P for the data points shown in **Figure 2.13B**. A greatly improved linearity is seen, which is indicative of a good agreement between experimental results and the proposed combined effects of photon generation and out-coupling on light yield. It should be noted that the usage of transmittance at 415 nm as the light out-coupling power would be a great underestimation of the true value, which should have contributed to the

degradation of linearity in the light yield relationship shown in **Figure 2.13C**. This is due to the fact that most scattered photons are lost and not being detected by the detectors in a UV-visible test, whereas for the scintillator wrapped by a set of Teflon reflectors, a substantial fraction of scattered photons can eventually reach the PMT after multiple scattering and reflections. Since the large band-gap nanoparticles do not absorb low energy photons, the decreased light out-coupling power should only be ascribed to an increased self-absorption within the matrix due to multi-scattering induced extension of light path. Accounting for this effect of photon scattering requires random-walk simulations with geometrical considerations, which is out of the scope of discussion for this dissertation; however, with a more accurately represented light out-coupling term, a greatly improved linear relationship between light yield and the product of light out-coupling power with η_P should be obtainable, which should also intercept with the axes at origin.

Although the nanoparticle nanocomposites showed some decay in light yield due to scattering-induced transmittance loss and energy trapping in the nanoparticles, the addition of HfO_2 nanoparticles produced a full energy photoelectron peak in the gamma pulse height spectrum as shown in **Figure 2.13A** (also **Figures 2.14** to **2.16** for all other nanocomposites**)**. The presence of this peak is due to the drastically increased possibility of photoelectric process in the nanoparticle-containing nanocomposites, which produces photoelectrons with full 662 keV energy from gamma photons. Since the probability of photoelectric effect is roughly proportional to the fourth to fifth power of Z, the likelihood of producing a full energy photoelectron in Hf (Z = 72) is about 12^4 to 12^5 times of that for carbon (Z = 6). As a result, although no photopeaks can be clearly resolved with typical organic scintillators, the addition of HfO_2 endows it with the ability to show full energy peaks of gamma rays, and therefore promises gamma spectroscopic applications.

To further study the gamma energy resolving power of this nanocomposite, another pulse height spectrum was obtained with a 2-mm-thick 20% nanoparticle composite using an acquisition time of 4 hours. The longer acquisition time improves signal-to-noise ratio and thus improves the statistical reliability. As shown in **Figure 2.13D**, a full energy peak consisting of a main peak at 607 keV and a shoulder peak at 662 keV was observed. Positions of these peaks are in good agreement with those of a true photopeak (662 keV) and a Hf Kα escape peak (662 – 55 = 607 keV). The high-Z Kα escape peak have been reported in a number of publications using small trial-size scintillators and should disappear at larger scintillator sizes due to diminished possibilities of the high-Z Kα X-ray escaping the scintillator.[1,38] The photopeak and Hf Kα escape peak were subsequently fitted into two Gaussian peaks with energy resolutions (defined as FWHM / peak energy) of 8.0% and 9.0%, respectively (R^2 = 0.995, **Figure 2.13D**). Pulse height spectrum of a 10% nanoparticle nanocomposite monolith was also measured and shown in **Figure 2.17**, with deconvoluted photopeak and escape peak resolutions of 5.8% and 8.3%, respectively. It should be noted that the fitted 5.8% photopeak resolution for 10% nanoparticle nanocomposite is likely an over-optimistic value (resolution around 7.5% would be more plausible) due to fitting errors induced by weak photopeak intensity, since photon statistics dictate that the resolution of photopeak should only be slightly better than the escape.[1] As a more conservative note, fitting the full energy peak as a whole also gives resolutions of 9.6% and 10.8% for the 10% and 20% nanoparticle nanocomposites, respectively (**Figure 2.18**). These results compare favorably with the previous reported value of 11.4% obtained using 31% Gd_2O_3 nanocomposites (net Gd_2O_3 nanoparticle loading around 20%).[71] One contribution to this improvement is the difference in PMT spectral sensitivity: the PMT is 2 times more sensitive to the present nanocomposite's deep

blue emission than the green emission from previous Gd_2O_3 nanocomposite.[1,2] The greater PMT sensitivity results in a higher apparent light yield (photons detected by the PMT) and thus better resolution for the blue scintillator, since the resolution is inversely proportional to the square root of light yield.[1]

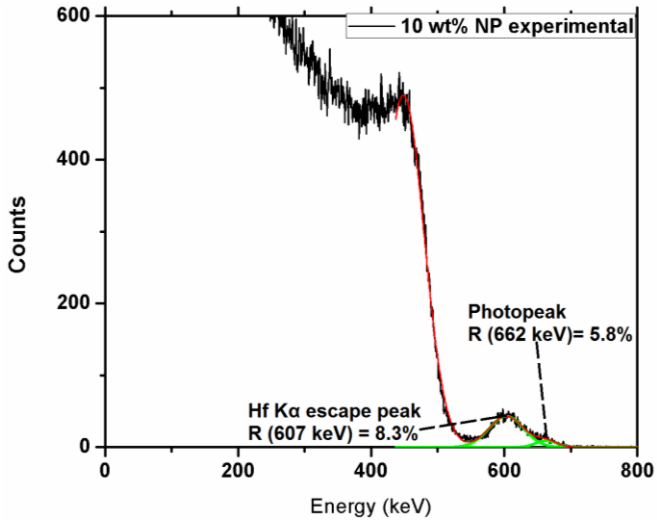

Figure 2.17 Fitted energy correlated pulse height spectrum of a 10 wt% nanoparticle PVT/PBD/POPOP composite monolith.

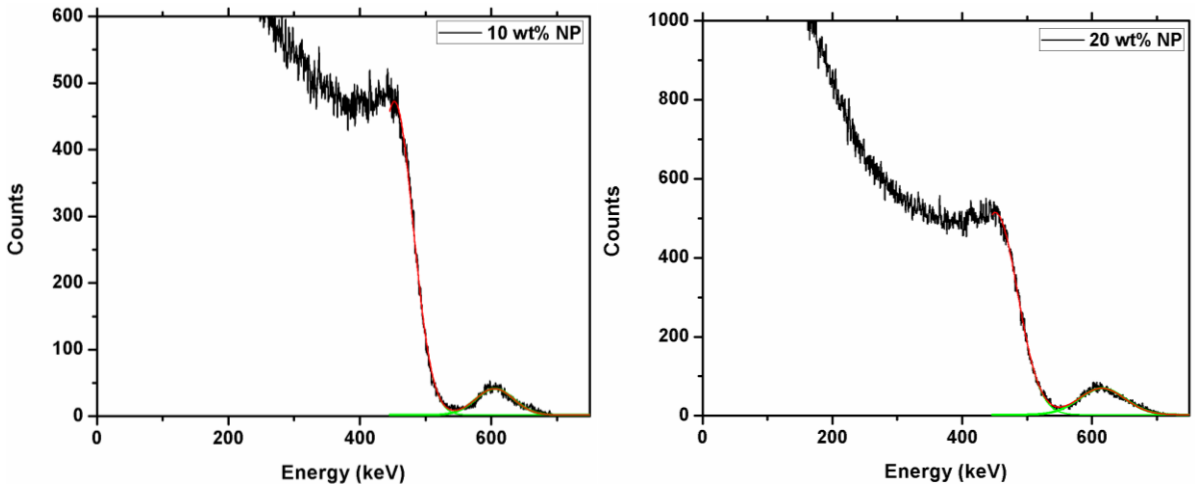

Figure 2.18 Energy correlated pulse height spectrum of 10 wt% (upper) and 20 wt% (lower) nanoparticle PVT/PBD/POPOP composite monolith. The full energy peaks were not deconvoluted but fitted as a whole.

The photoelectric cross-section of Hf is about 1.6 – 1.8 times of that of Gd (Z = 64); therefore, the photoelectric efficiency for 10% HfO_2 nanoparticle composite (net HfO_2 loading around 8.4%) is not much lower than that of the 31% Gd_2O_3 nanoparticle composite (net Gd_2O_3 nanoparticle loading around 20%), whereas the 20% monolith (net HfO_2 loading around 16.8%) has an even higher photoelectric efficiency than the 31% Gd_2O_3 composite. This relatively high photoelectric probability at lower nanoparticle% is beneficial, because both scattering and energy trapping increase with nanoparticle% and would thus deteriorate light yield. This is particularly important for the fabrication of nanocomposite monoliths sufficiently large for gamma spectroscopy. As the scintillator size increases, the X-ray escape peak would eventually disappear due to recapture of the escaping Hf Kα X-ray photon. Since the attenuation depth for a 50 keV X-ray photon is typically around a few cm in water, the disappearance of escape peak should be expected at sizes of several cubic inches for a low nanoparticle% composite monolith.

2.4 Concluding Remarks

In summary, HfO_2 nanoparticles with fairly uniform size distribution and excellent solubility in low-polarity solvent have been synthesized via a facile single-precursor method at high yield. The oleylamine ligand on nanoparticle surface can be replaced by BMEP to introduce polymerizable functional groups. Bulk polymerization of the modified nanoparticles dissolved in VT has produced bulk monoliths that remained transparent at nanoparticle loading as high as 40 wt%. Blue-emitting nanocomposite γ-ray scintillation monoliths have been synthesized, and a 2-mm-thick sample comprising up to 20 wt% nanoparticles, 2% PBD and 0.01% POPOP produced a deconvoluted photopeak with energy resolution ≤ 8% for 662 keV Cs-137 γ radiation. The

synthesis has high yield, and should be scalable to larger-size monoliths. However, the gamma light yield and photopeak resolution do not seem to improve with larger monoliths or higher loading, which may be attributed to aggravated light scattering and energy trapping during photoelectron cascade. In addition to the gamma scintillator application, with the facile syntheses and surface modification protocol developed in this work, the highly soluble, chemically inert, high-refractive-index HfO_2 nanoparticles should also find applications such as in composite high-κ dielectrics and biocompatible contrast agents in X-ray computed tomography.

Chapter 3. Syntheses of Group IVB metal oxide nanoparticles and their application in high refractive index nanocomposites

3.1 Introduction

The past few decades have seen a substantial development in the field of colloidal nanoparticles.[49,87,97–104] Due to the unusual nano-size effects such as quantum confinement, superparamagnetism, and extremely high specific surface area, various nanoparticles have been widely studied for a broad range of applications such as in energy harvesting, light emitting devices, biomedical applications, and catalysis.[97–100,103–107] In addition, colloidal nanoparticles dispersed uniformly in various solvents can be easily processed into different forms via simple solution casting techniques, rendering them a very versatile tool to use in device fabrication and materials engineering.[81,97,103,106,108]

Group IVB metal (Ti, Zr and Hf) oxide (**MO_2**) nanoparticles are among the most studied colloidal nanoparticles.[53,79,80,87,97,103,109–116] Exceptional properties such as chemical inertness, large band gap, high dielectric constant and refractive index (**RI**) nominate these nanoparticles as promising candidates for novel photocatalysts and engineered optical components.[80,105,110,113,117] Although a number of synthetic protocols such as aqueous and non-aqueous sol-gel method, hydrothermal

synthesis and solvothermal synthesis have been developed for MO_2 nanoparticles during the past few decades, a facile and scalable synthesis of nanoparticles with decent crystallinity, solubility and size distribution still remains challenging.[53,87,109–111,114–116] For instance, normal sol-gel synthesis is notorious for its difficulty in controlling the shape, size, and crystallinity of produced nanoparticles.[114] Hydrothermal method produces nanoparticles with good crystallinity, but their sizes are often too large for forming stable colloidal solutions.[111] Although the non-aqueous sol-gel synthesis employing cross-condensation between the metal chloride (**MCl_4**) and alkoxide (**$M(OR)_4$**) manages to produce nanoparticles with good crystallinity and solubility, this method has limited practicality since the use of trioctylphosphine oxide (a solid at room temperature) as solvent makes it very difficult to achieve uniform and stoichiometric mixing of the two components at large scale.[53,109] The single-precursor solvothermal synthesis utilizing an ether elimination reaction of $M(OR)_4$ might be the most facile and efficient synthetic protocol developed thus far; however, its wide application is still limited due to the use of pressurized vessel at high temperature and the resulting nanoparticles' poor solubility without follow-up surface modification.[87,110] Moreover, almost all of the as-mentioned methods involve using $M(OR)_4$ as a precursor, whose volatility, flammability, moisture-, air- and light-sensitivity also add to the difficulty and risks in storage and synthetic applications.

In the previous chapter, a single-precursor route has been introduced for the synthesis of HfO_2 nanoparticles using $Hf(CF_3COO)_4$ and oleylamine (**OAm**).[103] The simple one-pot heat-up synthesis using common synthetic glassware can produce small-size, narrowly dispersed HfO_2 nanoparticles with yield easily exceeding 90%. Moreover, the higher stability of $Hf(CF_3COO)_4$ also alleviates the complexity and risks involved in the storage and handling of typical alkoxides,

rendering this method more user-friendly. However, the detailed mechanism of this synthetic reaction still remained unclear. In addition, the much lower earth abundance of Hf (2 to 3 orders of magnitude lower than Zr and Ti) results in a much higher price of raw materials, therefore limiting the applicability of HfO_2 nanoparticles in general-purpose applications such as optical coating materials.

In this chapter, the previously developed synthetic protocol for HfO_2 is extended for the high-yield synthesis of narrowly dispersed ZrO_2 nanoparticles, where $Zr(CF_3COO)_4$ (**ZrTFA**) and OAm are used as the precursors. A series of experiments are performed to understand the reaction mechanism, with evidence indicating an amidization-assisted sol-gel reaction for the formation of oxide nanoparticles. The same protocol was further expanded to the synthesis of colloidal TiO_2 nanoparticles, thereby demonstrating the feasibility of using metal trifluoroacetates to synthesize all group IVB metal oxides. Using the highly dispersible ZrO_2 nanoparticles, high nanoparticle loading transparent nanocomposites (> 60 wt% nanoparticle loading) were fabricated in both monolithic and thin-film forms, proving the nanoparticles' great potential for high RI optical applications.

3.2 Experimental Section

3.2.1 Materials

Zirconium (IV) tetrachloride (99.9%), oleylamine (>98% primary amine), oleic acid (**OA**, technical grade, 90%), 1-octadecene (**ODE**, technical grade, 90%), trichloroacetic acid (99%), bis(2-(methacryloyloxy)ethyl) phosphate (**BMEP**), methylstyrene (**VT**, 99%) and divinylbenzene (**DVB**, 80%) were purchased from Sigma Aldrich. Titanium (IV) tetrachloride (99.9%), and 1,1-

di-(*tert*-butylperoxy)-3,3,5-trimethylcyclohexane (**Luperox-231**, 75% solution in aromatic free mineral spirit) were purchased from Acros Organics. Trifluoroacetic acid (99%) was purchased from EMD. Acetic acid (glacial) was purchased from Macron. All solvents used were of ACS grade. VT and DVB were purified by a mini column packed with inhibitor removers to remove *tert*-butylcatechol before use. All other materials were used as received.

3.2.2 Synthesis and fabrication

ZrTFA was synthesized following the protocol previously described by Sartori *et al.*[91] In a typical synthesis, trifluoroacetic acid (60.0 mL) was slowly added to $ZrCl_4$ (6.99 g, 30 mmol). The mixture was stirred at 40 ^oC for 5 hours and then dried by rotary evaporation and high vacuum to obtain ZrTFA in a white solid form (>97% yield). $Ti(CF_3COO)_4$ (**TiTFA**) in a white powdery form was synthesized in the same fashion, except that in this case the liquid $TiCl_4$ (2.19 mL, *ca.* 20 mmol) was injected into cool trifluoroacetic acid (30 mL) and heated to reflux for 5 hours.

The high-temperature synthesis of ZrO_2 nanoparticles from ZrTFA was carried out using a typical air-free Schlenk setup. In a typical reaction, ZrTFA (2.17 g, 4 mmol) was mixed with OAm (52.6 mL, *ca.* 160 mmol) and stirred under vacuum for 30 min at 110 ^oC. The resulting transparent solution was then heated to 330 ^oC for 1 hour under Ar. White ZrO_2 nanoparticles were flocculated by adding 150 mL acetone into the cooled reaction mixture, collected by centrifugation, and washed by re-dissolving and flocculating using toluene and ethanol for three times. Washed nanoparticles were dissolved in 20 mL toluene to form a stable colorless stock solution of around 30 mg/mL. Synthesis of TiO_2 nanoparticles was performed under the same procedures with the only exception that 1 gram of TiTFA was mixed with 53 mL OAm.

Surface modification of ZrO_2 nanoparticles was carried out by admixing the as-prepared ZrO_2 with a predetermined amount of BMEP in chloroform and stirring overnight. The resulting solution was first concentrated using rotary evaporation, then washed three times with hexane and acetone following the similar redissoving-flocculating procedure described above. The washed nanoparticles were first roughly air-dried and then dissolved in a nanocomposite precursor solution composed of 2 vol% DVB and 1 vol% Luperox-231 in VT. The clear solution was transferred into a 10 mm diameter glass vial and cured (100 ^oC, 24 hours) in a nitrogen protected glove box. After curing, the resulting monoliths were removed from the glass vials and polished for further characterizations. For the fabrication of ZrO_2 nanoparticle thin films, a typical process involves spin-coating 100 mg/mL ZrO_2 solution in tetrahydrofuran at 1500 rpm.

3.2.3 Attempted synthesis of ZrO_2 nanoparticles using other precursors

Synthesis of zirconium acetate ($Zr(OAc)_4$) and zirconium trichloroacetate (ZrTCA)

The synthesis of $Zr(OAc)_4$ was carried out in a similar way as ZrTFA. In a typical synthesis, acetic acid (20.0 mL) was added to $ZrCl_4$ (2.33 g, 10 mmol) to form a clear solution. The mixture was refluxed for 7 hours and then dried by rotary evaporation and high vacuum to obtain $Zr(OAc)_4$ as a white solid. EDX measurement showed very little amount of Cl (<10% vs. Zr), confirming the formation of zirconium acetate. For the synthesis of ZrTCA, trichloroacetic acid (7.85 g, 48 mmol) was first dissolved in 20 mL hexane. The solution was then added into a suspension of $ZrCl_4$ (1.40 g, 6 mmol) in hexane (20 mL). The suspension was stirred at 40 ^oC for 5 hr and then dried using rotary evaporation. The white crude product was washed three times using hexane before being thoroughly dried under high vacuum.

Attempted syntheses using $Zr(OAc)_4$, ZrTCA and zirconium oleate

Attempts to synthesize ZrO_2 nanoparticles from $Zr(OAc)_4$ and ZrTCA were made in a similar way as with ZrTFA. In short, the precursor (2 mmol) was first mixed with OAm (26.3 mL, *ca.* 160 mmol) and stirred under vacuum for 30 min at 110 ^oC, followed by reacting at 330 ^oC for 1 hour under Ar. The product was similarly washed using acetone and ethanol, except that the precipitate cannot be redispersed in toluene to form a transparent solution.

Another attempt to make ZrO_2 nanoparticles from zirconium oleate was made in a different way. The mixture of $ZrCl_4$ (0.45 g, 2 mmol), OAc (16 mmol) and ODE (40 mmol) was first heated to 110 ^oC under vacuum for 1 hour to generate zirconium oleate. OAm (24 mmol) was then added under Ar. The mixture was then heated to 330 ^oC for 1 hour. The white opaque solution was cooled and processed using acetone and ethanol in the same way as in other syntheses. The precipitate also could not be dispersed in toluene to form a transparent solution.

All these attempts failed to produce soluble crystalline materials.

Attempted syntheses using octadecylamine (ODA) and hexadecylamine (HDA)

Attempts to synthesize ZrO_2 nanoparticles were also made with saturated fatty amines such as ODA and HDA. The synthetic procedures were almost identical to the one using OAm, except that the room-temperature-solid ODA and HDA were first mixed with ZrTFA and mildly heated to around 50 ^oC to melt before subjected to degassing at 110 ^oC. The solution was transparent throughout the reaction and turned white turbid upon cooling. 25 mL toluene was poured into the flask at around 90 ^oC to prevent solidification, and the product was similarly flocculated and washed with ethanol and finally dispersed in toluene to form a white turbid suspension. The

suspension was centrifuged at 10000 rpm for 5 min, and only the supernatant was kept as product and characterized.

3.2.4 Characterizations

Transmission electron microscopy (**TEM**) was performed on an FEI T12 Quick CryoEM and CryoET microscope operated at 120 keV. High resolution TEM images were taken on an FEI Titan S/TEM operated at 300 keV. The nanocomposite thin-film TEM samples were prepared by focused ion beam etching of the monolith using an FEI Nova 600 SEM/FIB system. Powder X-ray diffraction (**XRD**) data was obtained using a Panalytical X'Pert Pro X-ray powder diffractometer with Cu Kα radiation. Fourier transform infrared (**FTIR**) spectra were obtained using a Jasco 420 FTIR spectrophotometer with standard KBr pelletized samples. UV-visible (**UV-vis**) tests were carried out on a Shimadzu UV-1700 spectrophotometer. For transmittance tests of monoliths, a set of homemade masks were applied to mount samples in a controlled way. Thermogravimetric analysis (**TGA**) was performed on a Perkin Elmer Diamond Thermogravimetric/Differential Thermal Analyzer. For determination of the organic contents on nanoparticles and in nanocomposites, the sample was first stabilized at 100 ^{o}C for 10 min to remove residue solvents and water before being heated to 850 ^{o}C in air at a ramping rate of 15 ^{o}C/min, after which it was kept at 850 ^{o}C for another 10 min to ensure complete decomposition. Scanning electron microscopy (**SEM**) and energy dispersive X-ray spectroscopy (**EDX**) was performed on an FEI Nova Nano 230 scanning electron microscope operated at 10 keV (15 keV for samples containing Ti). For insulating samples, a thin layer of Au was sputtered before SEM tests. Samples for EDX were first dispersed in corresponding solvents and then drop-casted onto Cu tapes, followed by vacuum drying to finish the preparation. RI measurements were carried out

using a Film Sense FS-1TM Multi-Wavelength Ellipsometer with a typical acquisition time of one second. For monolith sample measurements, one surface of the monolith was first roughened to reduce the birefringence induced by polymer. For thin film samples, the RI of glass substrate was first measured and then used for thin film measurements. The results were fitted using a Cauchy dispersion model, where the typical fitting errors were smaller than 0.1%. For mass spectrometry, five microliters of sample solution was placed in the center of the OpenSpotTM card, which was dried at room temperature and then applied to a Thermo Scientific ExactiveTM Plus benchtop Orbitrap mass spectrometer coupled to an IonSense ID-CUBE® ionization source using He as the carrier gas. The ID-CUBE discharge voltage was controlled through Thermo Scientific Xcalibur software by setting the ion source spray voltage to 1.0 kV and the sheath, auxiliary and sweep gases to zero for all ID-CUBE analyses. The Exactive™ Plus MS was operated in the negative ion modes from 75 to 1050 m/z.

3.2.5 Estimation of refractive index

Nanocomposites studied in this chapter all have very high nanoparticle loading (>20 vol%). In this case, the commonly used Maxwell Garnett model cannot be applied because it deals with composites wherein one component is sparsely dispersed in another[118]. The effective medium theory, or the Bruggeman's model, copes with high loading composites by assuming that two or more materials with similar loadings are interspersed in a random fashion, which is the case for high-loading nanocomposites studied in this chapter. Further assuming that most inclusions are round-shaped (as observed in TEM), the Bruggeman's model gives the following relation[118]:

$$\sum_i f_i \frac{{n_i}^2 - {n_{eff}}^2}{{n_i}^2 + 2{n_{eff}}^2} = 0 \tag{3.1}$$

where f_i, n_i, and n_{eff} are the volume fraction of component ***i***, refractive index of component ***i***, and the effective refractive index of the final composite, respectively. Using the documented refractive indices and f_i calculated from the weight percentage and density of each component, the effective refractive index can be estimated with the above equation.

3.3 Results and Discussion

3.3.1 Synthesis of ZrO_2 nanoparticles

ZrO_2 nanoparticles were successfully synthesized using a one-pot single-precursor method. The precursor, ZrTFA was first prepared via a simple reaction between $ZrCl_4$ and CF_3COOH as reported by Sartori *et al*.[91] Complete reaction of $ZrCl_4$ was confirmed by EDX in that no Cl could be detected. The as-synthesized ZrTFA was then used to synthesize ZrO_2 nanoparticles via a one-pot reaction as shown in **Figure 3.1A**. The transparent solution of ZrTFA in OAm was first dried at 110 ^oC under vacuum and then heated to 330 ^oC to produce ZrO_2 nanoparticles. The change in solution color from light green to almost colorless at 330 ^oC marked the completion of ZrTFA-to-ZrO_2 transition. **Figure 3.1B** shows a TEM image of the as-synthesized ZrO_2 nanoparticles. The nanoparticles were mostly round-shaped with similar sizes despite the presence of a few oval-shaped or interconnected nanoparticles. **Figure 3.1C** shows a histogram of more than 250 nanoparticles, where a mean size of 5.5 nm with 14.5% standard deviation (0.8 nm) was derived, indicating a narrow size distribution of the nanoparticles. Powder XRD result of the nanoparticles showed a good match with JCPDS card No. 01-089-9066, revealing a monoclinic crystallinity of the ZrO_2 nanoparticles (**Figure 3.1D**). Crystallite size calculations of the fitted (-111) and (111) peaks were performed using the Scherrer equation after stripping the Cu $K\alpha_2$ signal and instrumental broadening of 0.07^o. The calculated sizes of 5.8 nm and 6.0 nm for these two

directions matched well with the TEM observation, which indicated a good crystallinity of the as-synthesized nanoparticles. EDX measurement of the nanoparticles showed a roughly 1:2 ratio between Zr and O, thus confirming the composition of ZrO_2 nanoparticles.

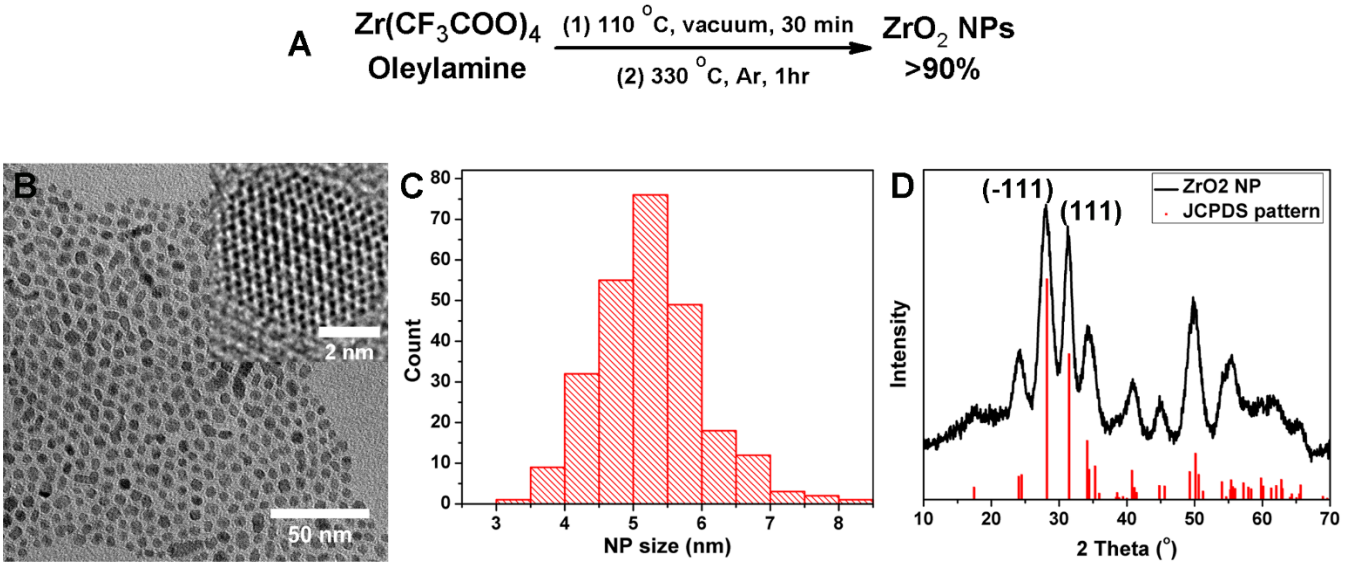

Figure 3.1 (A) Schematic of the one-pot synthesis protocol of ZrO_2 nanoparticles; **(B)** TEM image (inset: high resolution TEM of a single ZrO_2 nanoparticle) and **(C)** histogram of the as-synthesized ZrO_2 nanoparticles; and **(D)** powder XRD pattern of ZrO_2 nanoparticles with reference JCPDS pattern.

3.3.2 Study of nanoparticle formation mechanism

In the previous chapter, an amidization-assisted sol-gel mechanism was proposed based on the following two observations: 1) Reactions using high concentration of $Hf(CF_3COO)_4$ showed a sequence of transitions from clear solution - viscous gel - turbid suspension - clear solution from 290 ^oC to 330 ^oC; 2) No nanoparticles but yellow oil was obtained when OA was used instead of OAm. The same phenomena were also observed during the synthesis of ZrO_2 nanoparticles under identical conditions, indicating a similar passage for the formation of ZrO_2 nanoparticles as

proposed in **Figure 3.2**. In order to better understand the mechanism, a series of tests were performed, and the results and implications are discussed as follows.

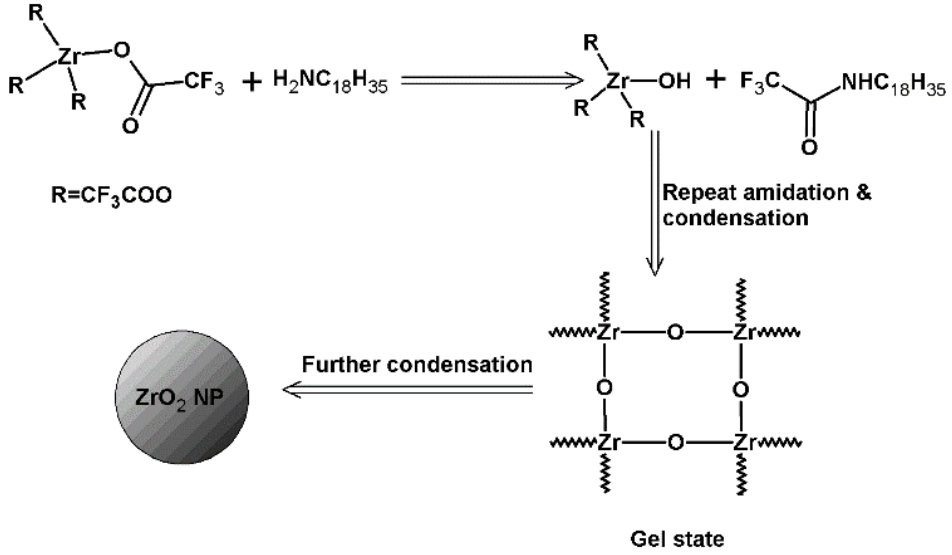

Figure 3.2 Proposed amidization-assisted sol-gel mechanism for ZrO_2 nanoparticle formation using OAm.

To begin with, metal trifluoroacetates were known for their decomposition at high temperature into corresponding fluorides, oxides and oxyfluorides.[48,119] Therefore, it is essential to first study the decomposition product of ZrTFA before investigating the reaction mechanism in solution with OAm. Direct calcination of ZrTFA was thus performed under Ar protection at 330 ^{o}C for 1 hour. As shown in **Figure 3.3**, powder XRD result of the greyish product can be matched with a combination of zirconium oxyfluorides $ZrO_{0.87}F_{2.46}$ (cubic, JCPDS 01-070-1651) and $Zr(O,F)_{2.7}$ (orthorhombic, JCPDS 00-039-1216). EDX measurement performed on the calcined sample showed a Zr/O/F ratio of 1:1.13:1.70, also indicating the formation of zirconium oxyfluorides. Similar results have been reported in a number of papers studying the thermal decomposition routes of ZrTFA.[93,119] In addition to the solid-state calcination, a solution-phase experiment using ZrTFA and the non-coordinating solvent, ODE was also carried out following the exact same

synthesis procedure for ZrO_2 nanoparticles, except that the solution was only heated to the reflux temperature of ODE (315 ^oC). The suspension of ZrTFA in ODE turned dark brown at elevated temperatures, suggesting the onset of decomposition and possibly, formation of oxidizing species. However, no crystalline materials could be obtained after the reaction. These results from both solid-state and solution-phase experiments excluded the possibility of ZrO_2 nanoparticle formation from direct decomposition of ZrTFA and indicated an important role of OAm in the production of ZrO_2 nanoparticles.

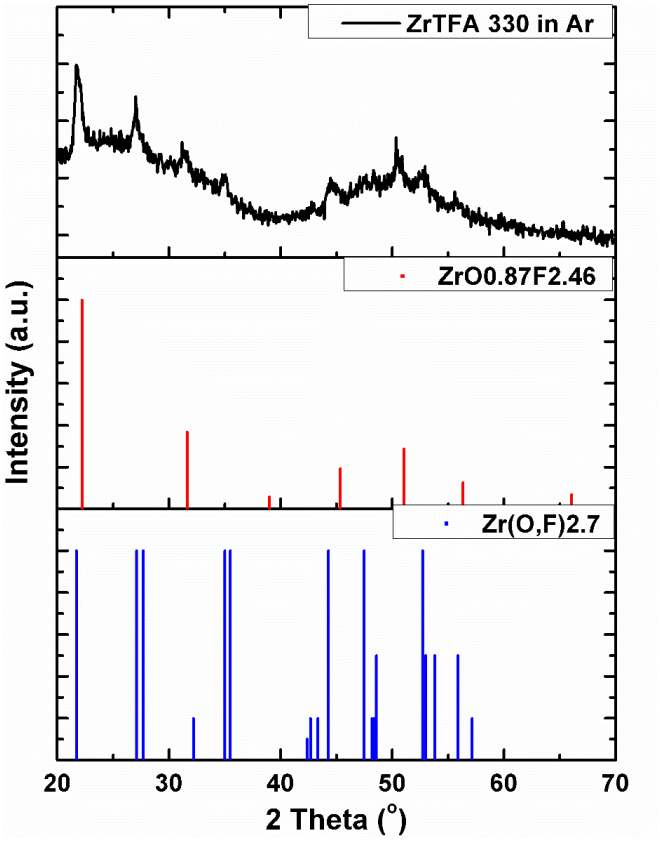

Figure 3.3 XRD profile of ZrTFA calcined at 330 ^oC for 1 hour in Ar, compared with two JCPDS patterns of zirconium oxyfluorides.

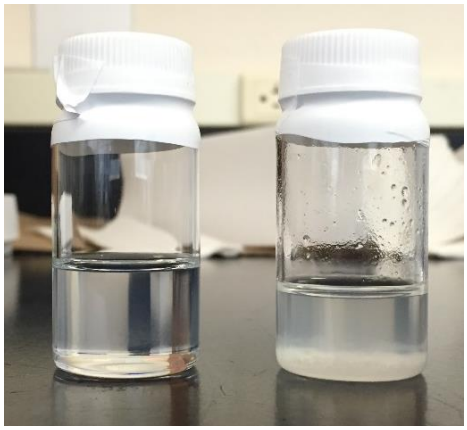

Figure 3.4 Photo of a clear toluene solution of ZrO_2 nanoparticle synthesized at 330 ^oC (**left**) and the 300 ^oC synthesized insoluble gel in toluene (**right**).

After confirming the synergistic effect between ZrTFA and OAm, a number of ZrO_2 syntheses were carried out under varied conditions to study the ZrO_2 formation mechanism. The first series of syntheses were performed using 1/40 ZrTFA/OAm precursor molar ratio at different final reaction temperatures ranging from 300 to 340 ^oC for 1 hour. All reactions yielded clear solutions upon completion, except that the solution of the 300 ^oC reaction looked slightly more viscous. Upon flocculation and centrifugation, toluene-redispersible white powders were successfully obtained from solutions of the 315, 330 and 340 ^oC reactions, whereas the precipitate of the 300 ^oC reaction was gel-like and insoluble in any solvent (**Figure 3.4**). Powder XRD characterizations were performed for these products dried under high vacuum. As shown in **Figure 3.5**, the reaction products from 315 to 340 ^oC showed similar diffraction patterns of ZrO_2 nanoparticles, whereas the dried gel of 300 ^oC exhibited significantly broader peaks, indicating its much inferior crystallinity. The poor crystallinity and gel appearance of the 300 ^oC product indicated an insufficient degree of cross-condensation among precursors as shown as the “gel state” in **Figure 3.2**. Since the onset of gel formation had been observed at around 290 ^oC in other reactions using

1/20 ZrTFA/OAm, the insufficient condensation at 300 °C after 1 hour of reaction seemed reasonable.

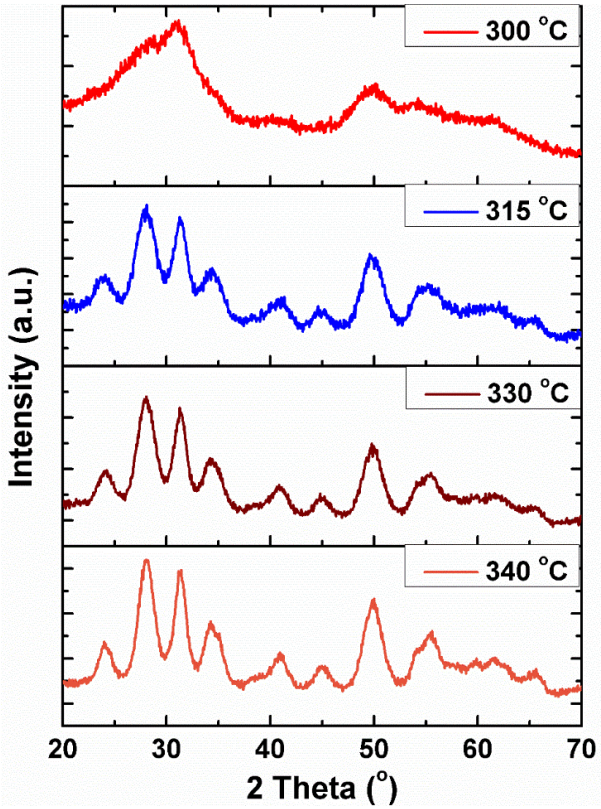

Figure 3.5 Powder XRD patterns of the ZrO_2 synthesis reaction products obtained at different aging temperatures ranging from 300 to 340 °C.

Table 3.1 Calculated crystallite sizes of ZrO_2-synthesis products obtained at 300-340 °C

	300 °C	**315 °C**	**330 °C**	**340 °C**
Calc. (-111) size / nm	Around 2*	4.1	5.8	7.4
Calc. (111) size / nm	Around 2*	6.1	6.0	6.4

* Peaks are too broad to be distinguished and accurately fitted, only approximate crystallite sizes are given.

TEM images of the products are shown in **Figure 3.6**. Discrete nanoparticles were observed for the 315 to 340 °C reactions. The particle size seemed to increase at a slow pace with the temperature, which was further confirmed by analyses of the XRD patterns (**Table 3.1**). In contrast

to the discrete nanoparticles obtained at higher temperatures, the reaction product at 300 ^{o}C appeared like an amorphous aggregate under TEM. However, electron diffraction on the "amorphous aggregate" showed a ring pattern which could be easily matched with the XRD pattern, indicating the presence of small crystalline phases within the aggregate. High resolution TEM image of the aggregate revealed a crosslinked network composed of very small crystals with sizes of around 2 nm (**Figure 3.7**). It could be seen that the small crystals with different orientations were mostly fused by regions with poor crystallinity, which formed backbones for the insoluble gel. These observations strongly suggested the formation of an inadequately condensed gel state during nanoparticle growth, thereby corroborating the as-proposed sol-gel mechanism.

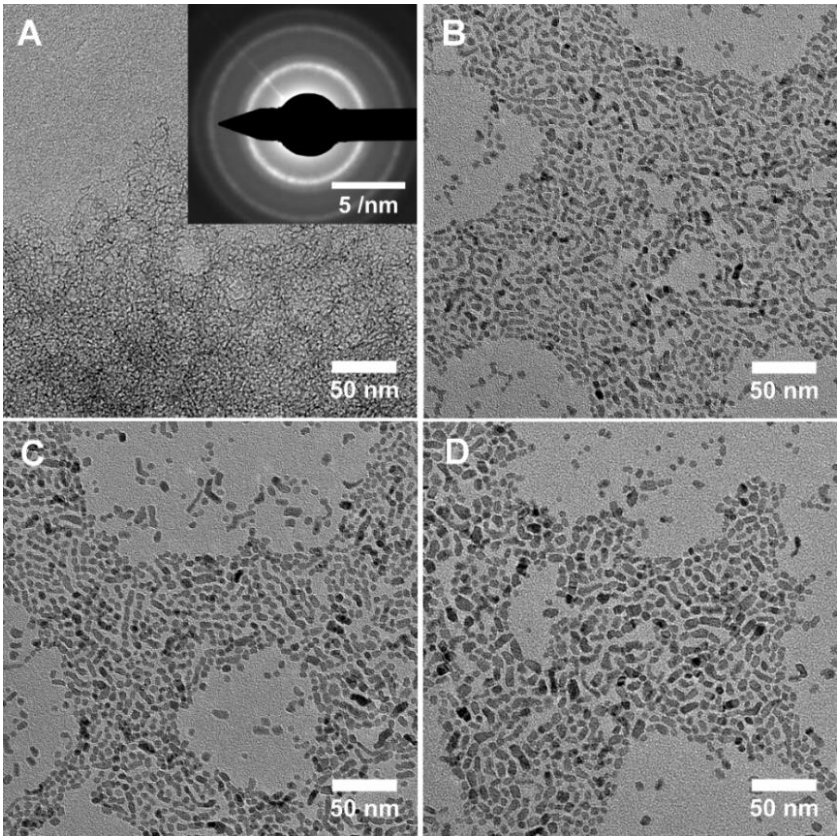

Figure 3.6 TEM images of the ZrO_2 synthesis reaction products obtained at **(A)** 300 ^{o}C, **(B)** 315 ^{o}C, **(C)** 330 ^{o}C and **(D)** 340 ^{o}C using 1/40 ZrTFA/OAm and one hour aging time (Inset of A: electron diffraction pattern of the 300 ^{o}C product).

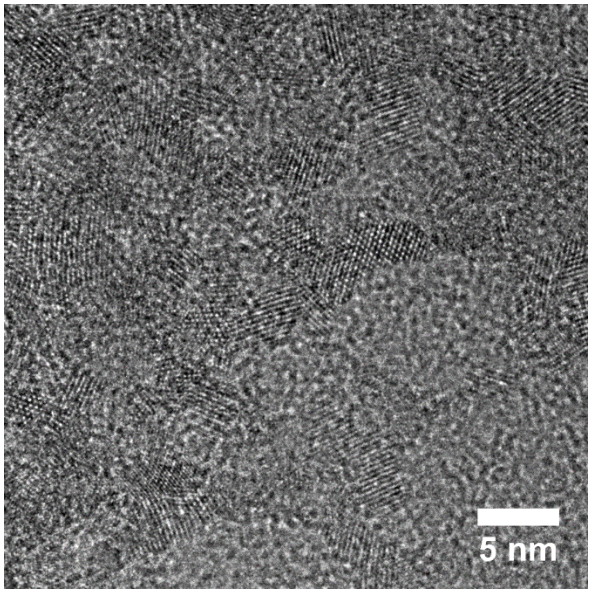

Figure 3.7 High resolution TEM image of the 300 ^{o}C reaction product.

To further confirm the as-proposed amidization-assisted sol-gel mechanism, another attempt was made to probe the proposed by-product, N-octadec-9-enyl trifluoroacetamide (**OleylTFAA**). Supernatant of the acetone precipitated reaction mixture was fed into a mass spectrometer coupled with a direct-analysis-in-real-time (**DART**) ion source. The mild DART source facilitated straightforward analyses, since it could generate simple protonated or deprotonated molecules in the positive or negative mode, respectively. The as-acquired mass spectrum in negative mode showed a strong peak at m/z = 362.267 (**Figure 3.8**). This peak could be very well matched with the molecular weight of deprotonated OleylTFAA anions (m/z=362.267), which strongly suggested the formation of OleylTFAA during the reaction and further corroborated the as-proposed mechanism. The appearance of peaks with even larger molecular weights was probably due to other side reactions such as additions of some decomposition product, whose likelihood could be greatly boosted at a temperature as high as 330 ^{o}C.

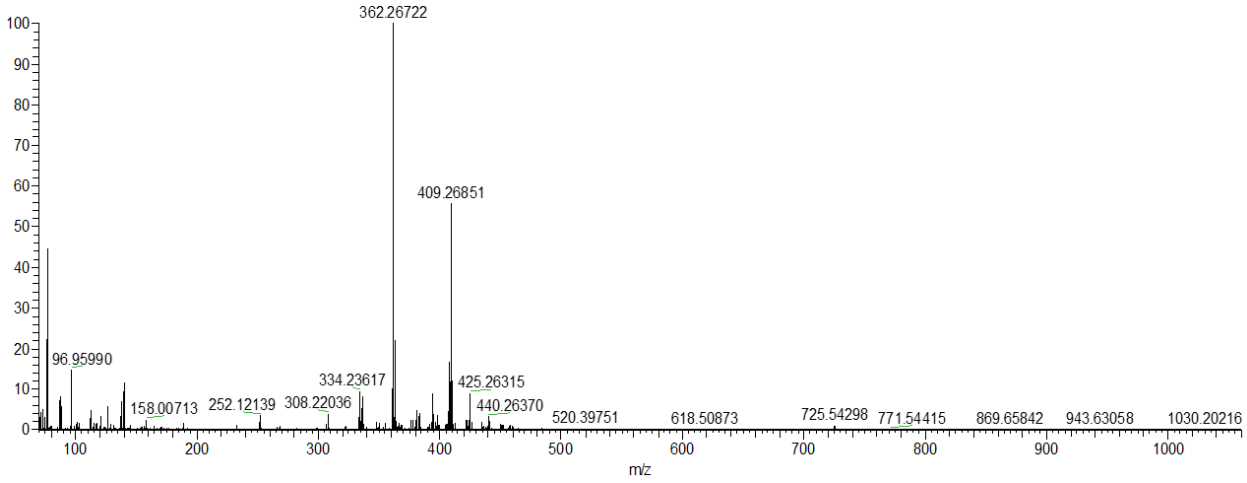

Figure 3.8 Negative mode mass spectrum obtained for the supernatant of acetone-precipitated nanoparticle-synthesis reaction mixture.

It should be noted that not all acetates of zirconium were effective in producing ZrO_2 nanoparticles. A number of attempts following the similar protocol were made using $Zr(CH_3COO)_4$, $Zr(CCl_3COO)_4$ and zirconium oleate, and none of these succeeded to generate crystalline products. All these failures could be attributed to a reduced likelihood for amidization reaction. Firstly, the failed syntheses using $Zr(CH_3COO)_4$ and zirconium oleate could be ascribed to the substantially weaker electrophilicity of aliphatic acetates, which could significantly reduce the likelihood of an electrophilic amidization reaction. Secondly, although trichloroacetic acid (pKa=0.66) has a similar acidity to trifluoroacetic acid (0.23), the significantly larger size of trichloromethyl group could drastically increase the steric hindrance for OAm to approach the carbonyl group and thus reduce the amidization reaction rate. In addition, the fact that only ZrTFA could be dissolved in OAm to form a clear solution indicated a good possibility of hydrogen bond formation in the form of N-H···F, which could possibly be beneficial for the amidization reaction as well (**Figure 3.9**).

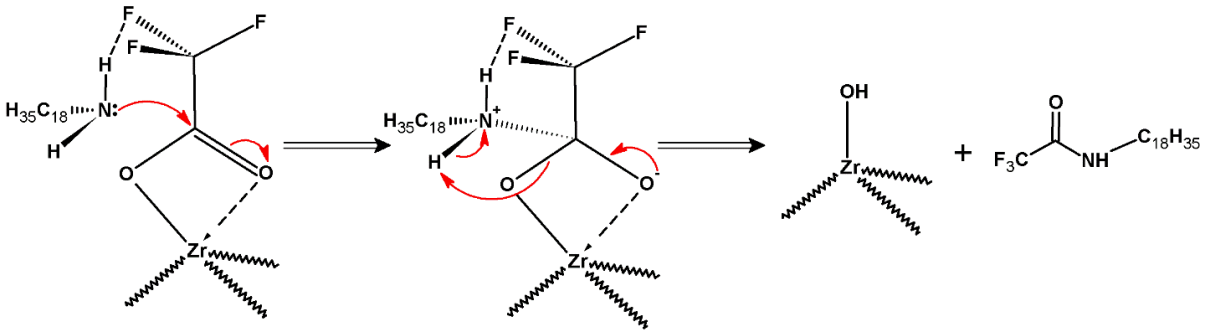

Figure 3.9 Proposed mechanism of the hydrogen-bonding-assisted amidization reaction.

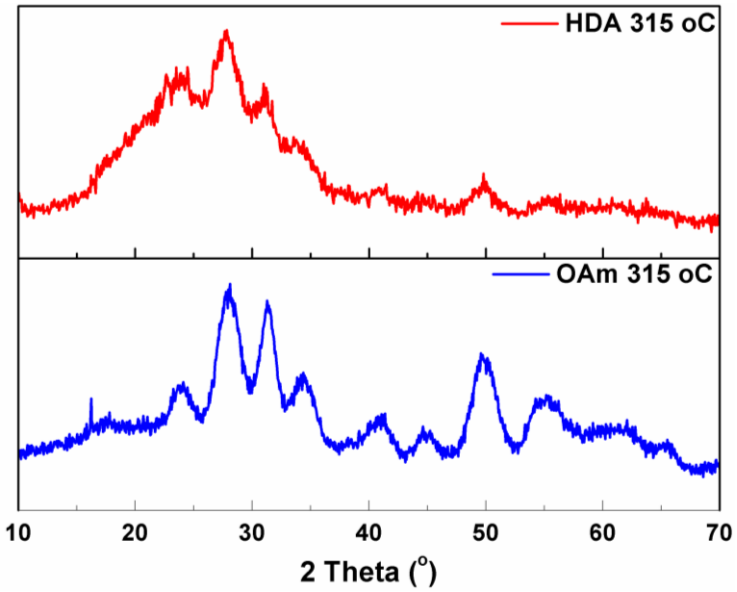

Figure 3.10 Powder XRD patterns of ZrO_2 synthesized with HDA and OAm at 315 °C.

In addition to the reaction's requirement on acetate, unexpectedly, the type of long chain amine was also found affecting the quality of final product. Several experiments were carried out to synthesize ZrO_2 nanoparticles with saturated fatty amines such as octadecylamine and hexadecylamine. Interestingly, while monoclinic ZrO_2 could still be obtained in these attempts, the crystallinity was much lower compared to the ZrO_2 nanoparticles synthesized under identical conditions using OAm (**Figure 3.10**). Such results implied that while the head amine group

facilitated the formation of ZrO_2 via the amidization-condensation reaction, structure of the aliphatic long chain could also play an important role in regulating the crystal sizes of the final product.

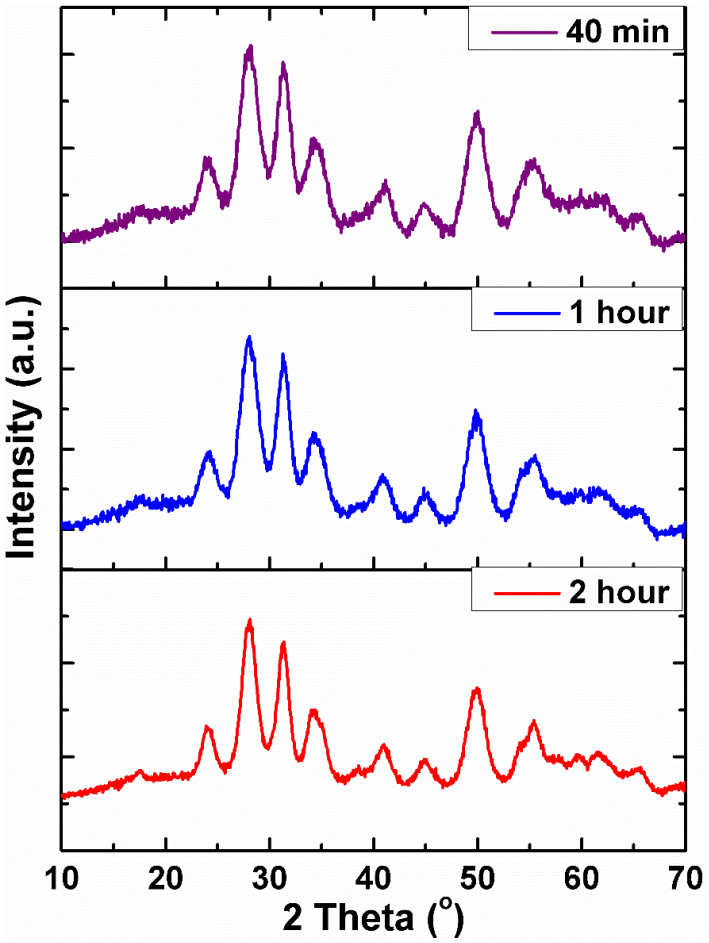

Figure 3.11 Powder XRD patterns of ZrO_2 nanoparticles synthesized at 330 °C using different aging times.

Table 3.2 Calculated crystallite sizes of nanoparticles synthesized at 330 °C at varied aging times.

	40 min	**1 hour**	**2 hour**
Calc. (-111) size / nm	5.4	5.8	7.3
Calc. (111) size / nm	5.9	6.0	8.6

To further explore the nanoparticle synthesis condition, another set of reactions was carried out at 330 ^{o}C for different aging times. **Figure 3.11** and **3.12** showed the powder XRD patterns and TEM images of the as-synthesized nanoparticles, with their calculated crystallite sizes being listed in **Table 3.2**. Both the crystallite and particle sizes were found to increase with aging time. However, nanoparticles synthesized with two-hour aging time displayed a much higher degree of size polydispersity and shape irregularity. Similar degradations in polydispersity and size regularity were also observed for nanoparticles synthesized at 340 ^{o}C for 1 hour as previously shown in **Figure 3.6D**. In addition to the commonly discussed factor of Ostwald ripening, an intensified degree of nanoparticle interconnection was also observed at higher temperature or for prolonged reaction time. This effect could be attributed to an increased possibility of condensation between unreacted surface hydroxyl groups on different nanoparticles, a phenomenon widely reported for both aqueous and non-aqueous sol-gel synthesis.[102,115,120]

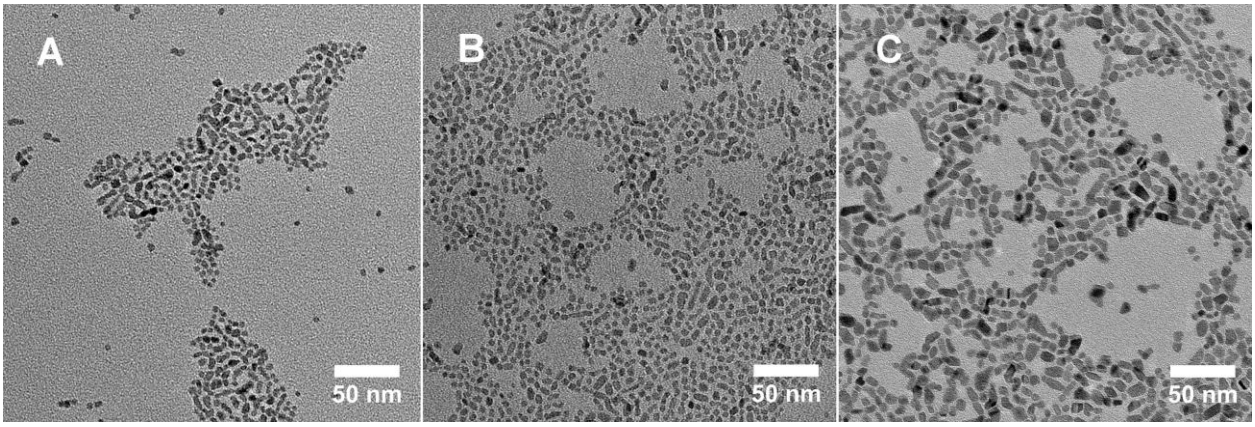

Figure 3.12 TEM images of ZrO_2 nanoparticles synthesized at 330 ^{o}C for **(A)** 40 min, **(B)** 1 hour and **(C)** 2 hour aging times.

3.3.3 Synthesis of TiO_2 nanoparticles

Our one-pot metal-trifluoroacetate protocol can be further applied to the synthesis of TiO_2 nanoparticles. White powdery TiTFA was first synthesized by refluxing the solution of $TiCl_4$ in trifluoroacetic acid.[91] The as-synthesized TiTFA was then dissolved in OAm to form a clear solution and then heated following the same protocol in ZrO_2 synthesis. A blue transparent solution was obtained at 330 ^oC, which upon precipitating and further washing gave a white powdery product that could be easily dispersed in toluene to form a colorless clear solution. **Figure 3.13** showed the TEM image and powder XRD result of the product, revealing the formation of anatase TiO_2 nanoparticles with an average size of around 6 nm. An acquired Ti/O radio of 1:2 from EDX analysis further confirmed the composition of TiO_2 nanoparticles. It is believed that the formation mechanism of TiO_2 nanoparticles should be the same as the ZrO_2 case investigated above, since direct calcination of TiTFA at 330 ^oC in Ar yielded products with mostly $TiOF_2$ crystallinity (**Figure 3.14**).

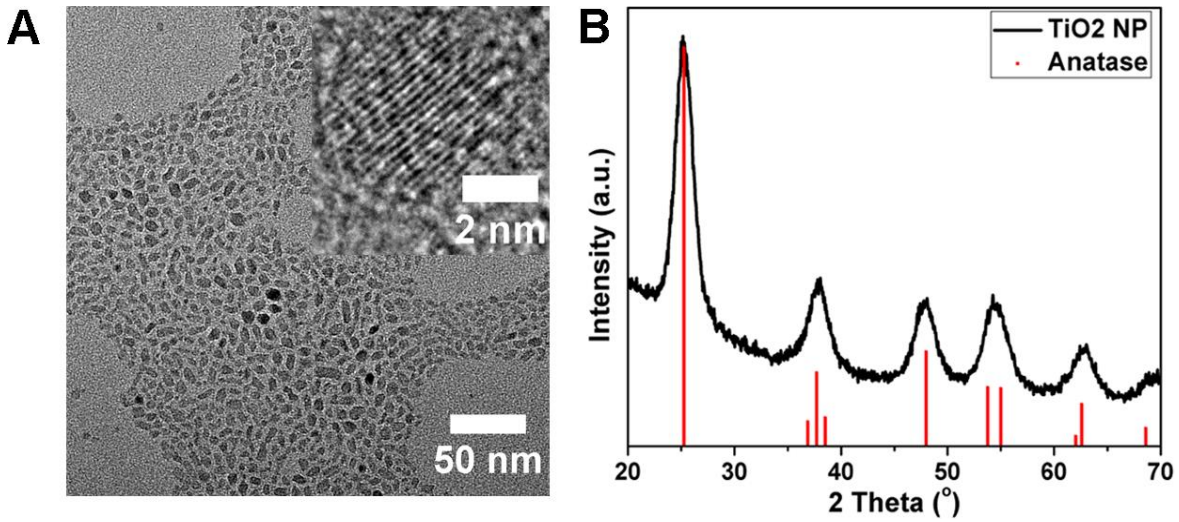

Figure 3.13 TEM images **(A)** and powder XRD pattern **(B)** of TiO_2 nanoparticles.

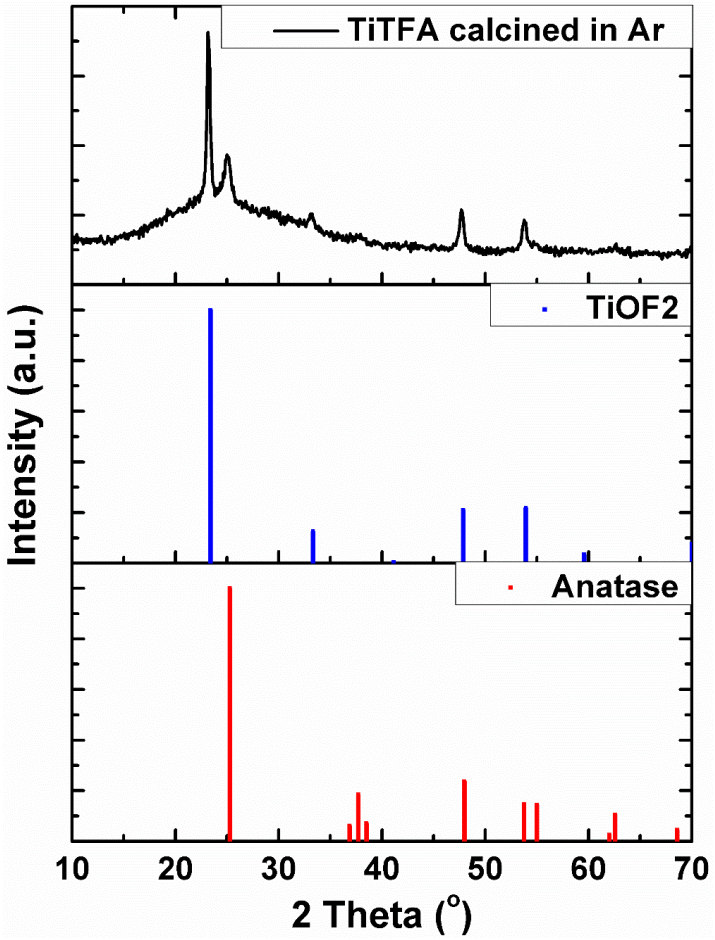

Figure 3.14 Powder XRD pattern of TiTFA calcined at 330 °C for 1 hour in Ar, in comparison to the standard patterns of $TiOF_2$ and anatase TiO_2.

3.3.4 Fabrication of high-RI monolith and thin film

Using the as-developed versatile protocol, highly soluble IVB metal oxide nanoparticles can be efficiently produced for various applications. As a demonstration, the as-synthesized ZrO_2 nanoparticles were used to fabricate transparent high RI nanocomposites in the forms of both bulk monolith and thin film.

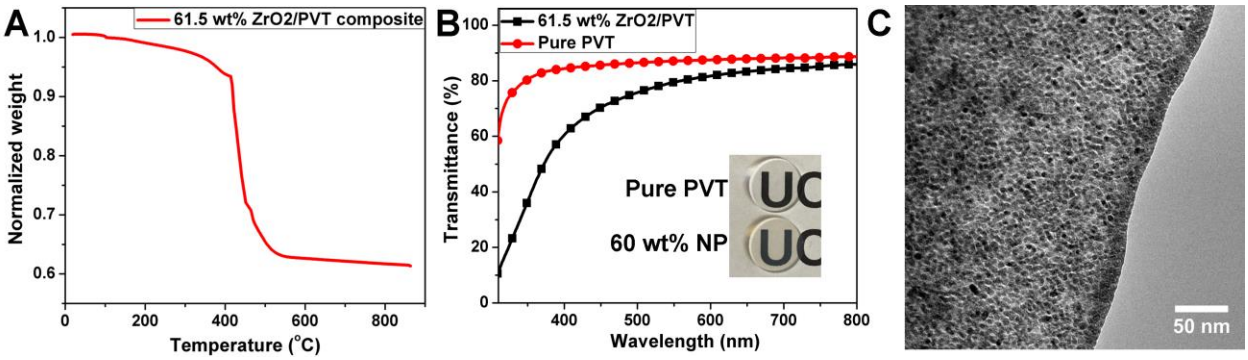

Figure 3.15 (A) TGA profile of a 61.5 wt% ZrO_2/PVT nanocomposite; **(B)** UV-vis transmittance curves of the 1 mm thick 61.5 wt% ZrO_2/PVT nanocomposite compared to a 1 mm thick pure PVT monolith (inset: photo of the two 1 mm thick monoliths); **(C)** TEM image of a focused ion beam etched thin film from the 61.5 wt% ZrO_2/PVT nanocomposite.

For the fabrication of transparent monoliths, ligand exchange was first performed on ZrO_2 nanoparticles using BMEP as reported in the previous chapter.[103] The surface modified nanoparticles were then dissolved at up to 80 wt% (organic ligand included) in a solution consisting of VT, DVB and 1 vol% peroxyketal thermal initiator, followed by curing in inert atmosphere at 100 °C for 24 hr to form transparent nanocomposites with thicknesses of 1 mm (after polishing). **Figure 3.15A** showed the thermogravimetric analysis (**TGA**) curve of such a high nanoparticle loading nanocomposite tested in air. The 61.5 wt% net ZrO_2 content (21.5 vol%) was among the highest loadings reported for transparent monolithic nanocomposites.[81,121] **Figure 3.15B** showed the UV-visible (**UV-vis**) transmittance spectra and photo of the 1 mm thick 60 wt% ZrO_2 nanocomposite compared to a bare PVT/DVB polymer composite with the same thickness. The high nanoparticle loading nanocomposite showed a similar transparency as the bare polymer composite by visual inspection, and its transmittance in the visible range was also decent (79.4% at 550 nm) as shown in the UV-vis spectrum. The faster deterioration of transmittance towards the shorter wavelength region should be attributed to an intensified Rayleigh scattering by

nanoparticles, since the ZrO_2 nanoparticles showed almost no absorption above 250 nm (**Figure 3.16**).[81,121] A uniform dispersion of nanoparticles within the polymer matrix was observed through TEM (**Figure 3.15C**), which was the main reason for this high transparency. It should be noted that the seeming "aggregation region" on the left of **Figure 3.15C** was in fact due to the inhomogeneity of focused ion beam etching, which was caused by severe warping of the film during etching.

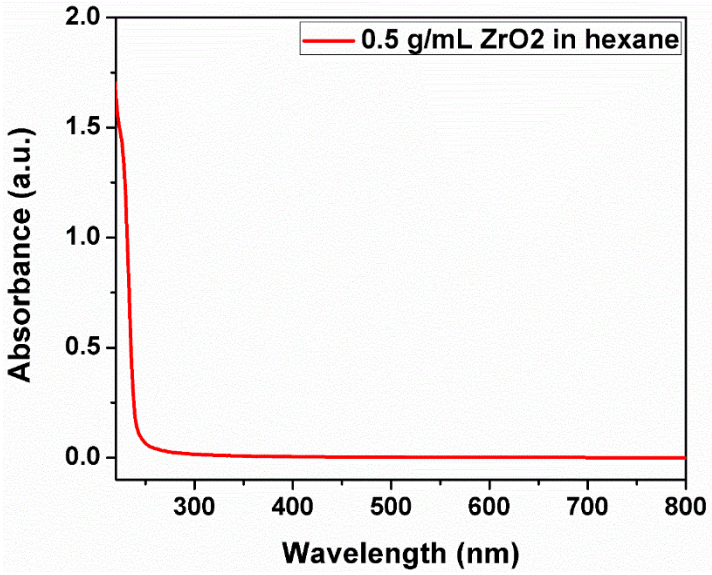

Figure 3.16 UV-vis absorption spectrum of a 0.5 g/mL ZrO_2 nanoparticle solution in hexane.

The addition of high RI ZrO_2 nanoparticles at high loading was supposed to enhance the RI of the resulting nanocomposite. **Figure 3.17** showed the RIs of both pristine PVT and 61.5 wt% ZrO_2/PVT nanocomposite measured with ellipsometry. Compared with pristine PVT (RIs from 1.553 to 1.567 at wavelengths from 663 nm to 400 nm, respectively), the nanocomposite displayed significantly improved RIs of 1.649 to 1.672 at 633 to 400 nm, respectively. However, these measured RIs of the nanocomposite are still lower than what one would expect for a 61.5 wt% ZrO_2/PVT nanocomposite (around 1.681 at 589 nm, calculated using Bruggeman's model[118,122]).

This could be explained by the fact that the nanocomposite contained a substantial amount of low RI organic ligands (OAm and BMEP) adhered to the nanoparticle surface. By plugging known refractive indices and calculated volume percentages of all components in the nanocomposite into the Bruggeman's model, an estimated refractive index of around 1.642 at 589 nm was obtained, showing a close match with the measured value of 1.651 and thus confirming the influence by low RI ligands (**Table 3.3**).

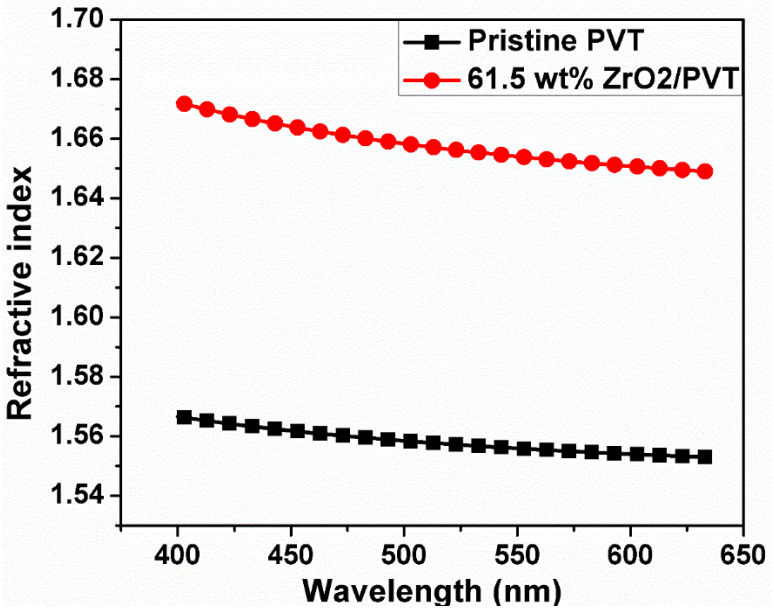

Figure 3.17 Refractive indices of the pristine PVT monolith and 61.5 wt% ZrO_2 nanoparticle/PVT nanocomposite monolith.

Table 3.3 Constants and derived values for components in 61.5 wt% ZrO_2 /PVT nanocomposite

Component	**Density(g/cm^3)**	**$n_{(589\ nm)}$**	**wt%**	**vol%**
ZrO_2	5.68	2.159	61.5	21.5
OAm	0.81	1.46	11.3 [b]	27.6
BMEP	1.28	1.47	5.6 [b]	8.7
PVT	1.02	1.554 [a]	21.6 [b]	42.1

a: From measured RI; **b**: Estimated with TGA result of BMEP-modified ZrO_2 nanoparticles.

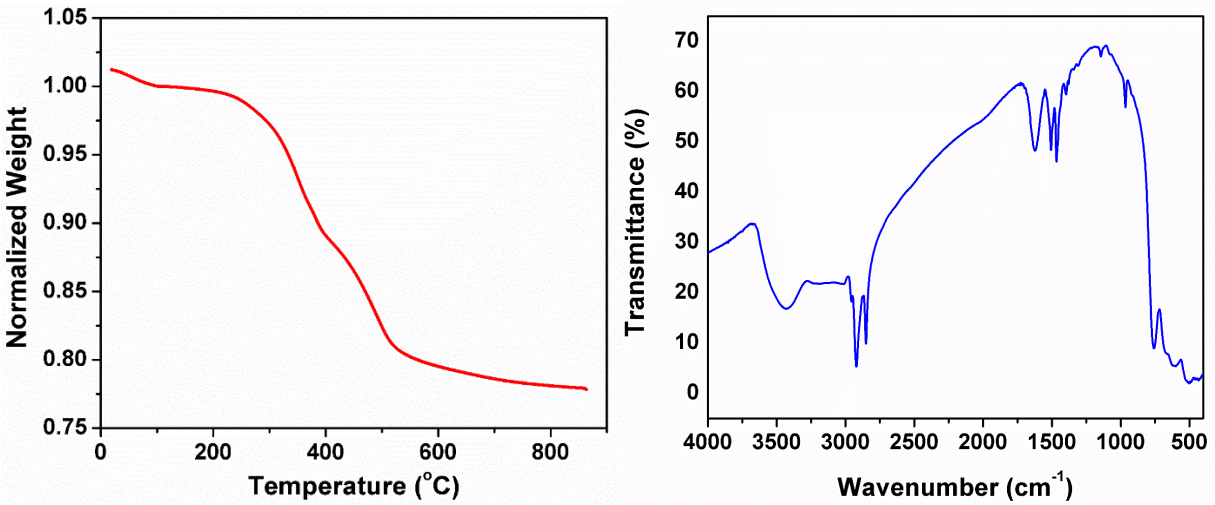

Figure 3.18 TGA profile (left) and FTIR spectrum (right) of the as-synthesized ZrO_2 nanoparticles.

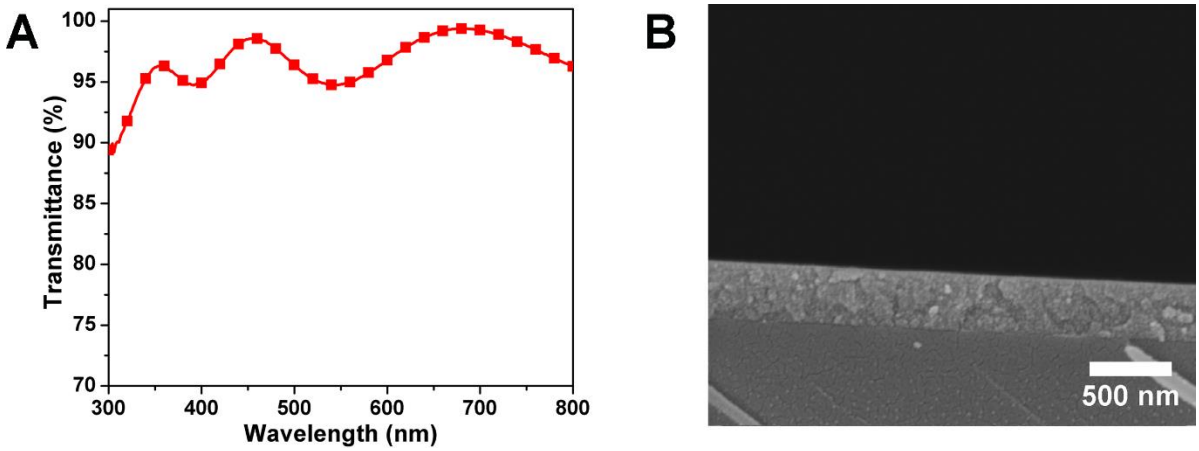

Figure 3.19 (A) UV-vis transmittance curve and **(B)** cross-sectional SEM image of a spin-coated thin film comprising only OAm-coated ZrO_2 nanoparticles.

In addition to the monolith, the nanoparticles can also be applied to the fabrication of thin films. Due to the large amount of OAm ligand on surface (23.0 wt%, approximately 67.6 vol%, FTIR result indicates presence of OAm ligand as analyzed in last chapter, **Figure 3.18**), simply spin-coating the nanoparticles could already form a "ZrO_2/organic nanocomposite" thin film. As shown in **Figure 3.19A**, the thin film had excellent transmittance in the visible and UVA regions (average >

97%), the typical range for most optical applications. It should be noted that the rapid transmittance deterioration slightly above 300 nm is most likely due to glass absorption but not absorption or scattering by ZrO_2 and ligand, and the corrugation on spectrum was a result of thin film interference. **Figure 3.19B** showed a cross-sectional SEM image of the spin-coated thin film. A uniform, dense layer of around 350 nm was observed, indicating a good film quality. The dense film showed a quite strong adherence to the glass substrate and resistance to scrubbing, which was likely due to intertwining of the surface-bound OAm molecules. RI of the thin film was measured by ellipsometry (**Figure 3.20**). The measured RIs of 1.677 at 633 nm and 1.710 at 400 nm are similar to the state-of-the-art nanocomposites with similar ZrO_2 loadings in low RI organic matrices.[80,81,123] In addition, the Bruggeman's model was also used to estimate the refractive index of this thin film composed of only OAm-coated ZrO_2 nanoparticles. As shown in **Table 3.4**, the calculated RI of 1.674 at 589 nm has a good match with the measured value of 1.680. It is assumed that by replacing the OAm ligand with smaller molecules with similar or even larger RI, the weight and volume fraction of ZrO_2 nanoparticles could be increased, which would lead to nanocomposites with larger RIs.

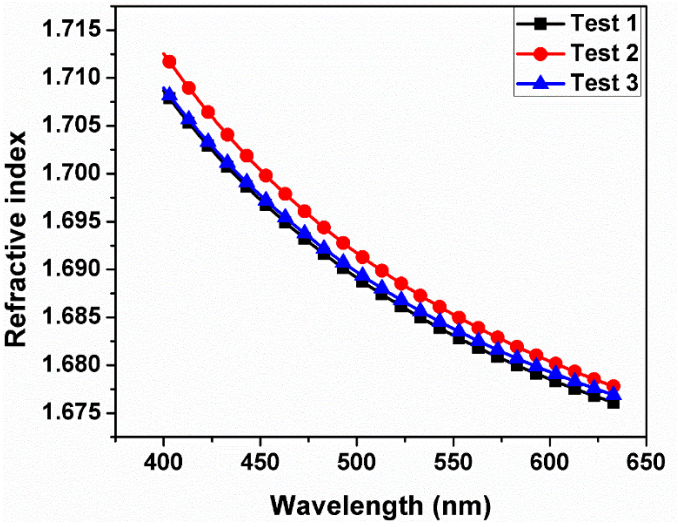

Figure 3.20 Refractive indices of the OAm-coated ZrO_2 nanoparticle thin film.

Table 3.4 Constants and derived values for components in OAm-coated ZrO_2 nanoparticles

Component	**Density(g/cm^3)**	**$n_{(589\ nm)}$**	**wt%**	**vol%**
ZrO_2	5.68	2.159	77.0	32.4
OAm	0.81	1.46	23.0	67.6

3.4 Concluding Remarks

In summary, stable colloidal ZrO_2 and TiO_2 nanoparticles have been successfully synthesized using their trifluoroacetates. Considering the previously demonstrated synthesis of HfO_2 nanoparticles, all IVB metal oxide nanoparticles can now be synthesized using this facile one-pot single-precursor method. The nanoparticle formation mechanism has been investigated from various aspects such as precursor decomposition, varied synthesis conditions, and by-product tracing. Current observations indicate that the reaction follows an amidization-assisted sol-gel mechanism, which expands the current toolkit of non-aqueous sol-gel chemistry. The highly soluble ZrO_2 nanoparticles have been used to fabricate highly transparent high RI bulk nanocomposites (>60 wt% net ZrO_2 loading, T_{550nm}>79% at 1 mm thickness, n_{400nm}=1.67) and dense, uniform high RI thin films (n_{400nm}=1.71), both kinds amongst the best reported so far. The facile, high-yield synthetic method has no requirement on specialized high pressure vessels, and the trifluoroacetate precursors have better stability than the alkoxides due to their less susceptibility to hydrolysis. These factors render this protocol an improved high-efficiency method for synthesizing IVB metal oxide nanoparticles. The small-sized colloidally stable nanoparticles enable facile solution processing in a wide loading range for fabricating nanocomposites in different transparent forms, suggesting wide applications for the nanoparticles in optical materials

engineering. In addition, the highly soluble nanoparticles could potentially be further applied in other solution reactions to form functional nanostructures, endowing the nanoparticles with more possibilities for applications such as in catalysis and nanotherapeutics.

Chapter 4. Quantum dot/polymer nanocomposite scintillator

4.1 Introduction

Low-cost, high-performance spectroscopic γ-photon detectors have been long sought for due to their numerous applications in high-energy physics, the promotion of nuclear non-proliferation, and medical imaging.[1,4,9] Scintillators resolve γ energy by proportionally converting a single high-energy photon into a number of photomultiplier-tube (**PMT**) detectable low-energy photons, which is considered a more affordable solution for general purposes than delicate semiconductor detectors.[1,2] An ideal scintillator should simultaneously exhibit the following traits: 1) high atomic number (**Z**) to increase gamma attenuation and photoelectron production; 2) high light yield (**LY**, low energy photons produced per unit energy deposited, photons/MeV); 3) short emission decay lifetime; and 4) low cost and ease of large-scale fabrication. However, commercial scintillators, generally made of either inorganic single crystals or plastics, inevitably fail to meet all of these requirements due to their intrinsic material properties and limitations in fabrication processes. Nanocomposite scintillators composed of uniformly dispersed high-Z nanoparticles and organic dyes in a polymer matrix have been proposed to integrate the high-Z of inorganics with the fast decay and low cost of plastics, thereby improving the overall performance and cost-effectiveness.[38,61–63,65,71,103] However, most attempts were stalled at low nanoparticle loadings (<10 wt%) due to severe optical loss induced by aggregation at higher concentrations, limiting their

potential for practical application.[62,63,65] While the use of high-Z organometallics provided an alternative for higher loading, their strong spin-orbit coupling effect necessitates careful matching of their triplet energy levels using costly triplet emitters.[38,124] Recently, the group of Pei *et al*. has fabricated transparent nanocomposite scintillators containing up to 60 wt% of surface-modified high-Z oxide or fluoride nanoparticles which have been used to detect a 662 keV γ photopeak.[71,103,125,126] However, in this system, the LY deteriorates at higher nanoparticle loadings as the energy deposited in the non-emitting nanoparticles cannot be transported to dye sites to produce photons, limiting the loading to < 30% for practical use.[103,126]

Quantum dots (**QDs**) have been touted as a promising candidate for numerous applications such as in light emitting devices[127–134], photodetectors,[15,106,135,136] bio-labelling and imaging,[100,137–139] and energy harvesting[140–142] due to attractive properties such as narrow tunable emission and high photoluminescence quantum yield (**PLQY**). For nanocomposite scintillator applications, incorporation of QDs could theoretically improve both Z and LY of the nanocomposite scintillator due to the QDs' higher Z and PLQY.[61,63] However, aggregation of QDs still poses the biggest hurdle against achieving any loading level applicable for practical usage (> 20 wt%).[62–64] Furthermore, the QDs' small Stokes shift also becomes problematic at high loadings because the severe self-absorption can easily destroy the LY of these scintillators.

In this chapter, it is demonstrate that, by overcoming aggregation and self-absorption issues, the use of $Cd_xZn_{1-x}S$/ZnS core/shell (**CZS**) QDs at extremely high loadings (up to 60 wt%) in a polyvinyltoluene (**PVT**) matrix with sufficient 4,7-bis-{2'-9',9'-bis[(2''-ethylhexyl)-fluorenyl]}-2,1,3-benzothiadiazole (**FBtF**) dyes is capable of simultaneously improving Z and LY in the

resulting nanocomposite scintillators. A simple surface modification step using bis(2-(methacryloyloxy)ethyl) phosphate (**BMEP**) enables the QDs to be covalently attached to the polymerizing PVT chain, thus preventing aggregation and facilitating high transparency in the product monolith with a record-high QD loading (T_{550nm} = 65.8% for a 60 wt% QD nanocomposite monolith). Efficient Förster resonance energy transfer (**FRET**) from QDs to the lower-band-gap FBtF both suppresses QD self-absorption and promotes the extraction of QD-borne excitons to dye sites for photon production, resulting in an improved LY of up to 10% compared to the control sample. The ultra-high loading of QD greatly improves the Z and, for the first time, enabled detection of the 662 keV gamma photopeak using a QD-loaded nanocomposite scintillator. In the best demonstration, a 60 wt% CZS QD/2% FBtF/PVT nanocomposite scintillator showed a LY of 9255 photons/MeV and a photopeak resolution of 9.8% under 662 keV Cs-137 γ irradiation.

4.2 Experimental Section

4.2.1 Materials

Cadmium oxide (99.99% trace metal basis), zinc acetate (99.99% trace metal basis), oleic acid (technical grade, 70%), 1-octadecene(technical grade, 90%), sulfur (99.998% trace metal basis), tributylphosphine(97%), bis(2-(methacryloyloxy)ethyl) phosphate (**BMEP**), methylstyrene (commonly referred to as vinyltoluene, **VT**, 99%), divinylbenzene (**DVB**, technical grade, 80%), 1,4-bis(5-phenyl-2-oxazolyl)benzene (**POPOP**), and Luperox 231 (92%) were purchased from Sigma Aldrich. All common solvents used were ACS grade, while solvents used for spectroscopy were HPLC grade. VT and DVB were purified by a mini column packed with inhibitor removers to remove *tert*-butylcatechol before use. An Eljen-212 general-purpose plastic scintillator was obtained from Eljen Technology and was polished into a disk with dimensions 10 mm in diameter

and 2 mm thickness to serve as the standard for scintillation measurements. 4,7-bis-{2'-9',9'-bis[(2''-ethylhexyl)-fluorenyl]}-2,1,3-benzothiadiazole (**FBtF**) was synthesized according to a previous protocol developed by Chen *et al*.[143,144] All other materials were used as received.

4.2.2 Synthesis of $Cd_xZn_{1-x}S/ZnS$ core-shell quantum dots

$Cd_xZn_{1-x}S/ZnS$ core-shell QDs were synthesized following a well-developed protocol using a typical air-free Schlenk setup.[129] All sulfur stock solutions used thereafter were prepared air- and water-free and stored under Ar. In a typical synthesis, 1 mmol of CdO, 10 mmol of $Zn(OAc)_2$, 7mL of oleic acid (**OA**) and 15 mL of 1-octadecene (**ODE**) were first loaded into a 150 mL three-neck round-bottom flask. After three pump-refill cycles, the mixture was heated to 110 ^oC under vacuum (pressure around 3 torr) and kept there for an hour. The almost colorless clear solution was then heated to 300 ^oC under Ar. A stock solution (preheated to 100 ^oC) containing 2 mmol of S in 3 mL of ODE was swiftly injected into the reaction mixture, then the reaction temperature was raised to 310 ^oC. After 8 min of reaction, a second stock solution containing 8 mmol of S in 4 mL of tributylphosphine (**TBP**) was injected drop-wise into the reaction mixture. The reaction was left at 310 ^oC for an hour and then cooled to room temperature. 180 mL of acetone was added to the cooled mixture, followed by centrifugation at 11000 rpm for 10 min to yield orange oil precipitated at the bottom. The oil was washed with 3:1 EtOH/toluene twice, followed by another three times with 3:1 acetone/toluene to get QDs as a white precipitate. The QDs were finally dissolved in 20 mL of toluene to form a stock solution. Typical yield of the reaction was above 90%.

4.2.3 Fabrication of ultra-high-loading QD/PVT nanocomposite monoliths

Surface modification of the QDs was performed following a similar protocol described previously.[125] In a typical experiment, 1000 mg of QDs were precipitated from the toluene stock solution using EtOH. The QDs were then dissolved in 14 mL of $CHCl_3$ to form a clear solution, into which 89 mg of BMEP in 2 mL $CHCl_3$ was added drop-wise under rigorous stirring. The reaction mixture was left stirring overnight and then filtered through a 200-nm pore-size PTFE syringe filter to remove the minimal precipitates generated during the reaction. The as-filtered solution was first concentrated using rotary evaporation and then washed twice with 3:1 acetone/toluene, followed by washing another two times with 3:1 acetone/hexane. The washed QDs were sonicated to disperse in a VT solution containing 5 vol% DVB and 0.1 vol% Luperox 231. The clear solution was then brought into a nitrogen-protected glove box and mixed with 1-5 wt% of FBtF in 10 mm diameter glass vials, followed by thermal curing at 95 ^{o}C for 24 hours. After curing, the resulting monoliths were removed from the glass vials and polished for further characterizations.

4.2.4 Characterization

Transmission electron microscopy (**TEM**) images were taken using an FEI T12 Quick CryoEM and CryoET microscope operated at 120 keV. The nanocomposite thin-film TEM samples were prepared by focused ion beam etching of the monolith using an FEI Nova 600 SEM/FIB system. Powder X-ray diffraction (**XRD**) data was obtained using a Bruker D8 Discover powder x-ray diffractometer with Cu Kα radiation. Fourier transform infrared (**FTIR**) spectra were obtained using a Jasco 420 FTIR spectrophotometer. FTIR samples were prepared by applying a drop of QD solution (around 50 mg/mL) onto a Real Crystal KBr IR sample card followed by drying in

air. Energy dispersive X-ray spectroscopy (**EDX**) was performed on an FEI Nova Nano 230 scanning electron microscope operated at 10 keV. The EDX samples were first dispersed in corresponding solvents and then drop-casted onto Cu tape, followed by drying under high vacuum. UV-visible tests were performed on a Shimadzu UV-1700 spectrophotometer. Homemade masks were applied to reduce the variations in light paths for monolith transmittance tests. Thermogravimetric analysis (**TGA**) was performed on a Perkin Elmer Diamond Thermogravimetric/Differential Thermal Analyzer. The sample was first stabilized at 100 ^{o}C for 10 min to remove residue solvents and water before being heated to 750 ^{o}C in air at a ramping rate of 10 ^{o}C/min, followed by an isothermal process at 750 ^{o}C for another 20 min to ensure complete decomposition. Photoluminescence (**PL**) spectra were obtained with a PTI QuantaMaster 30 spectrofluorometer. Solution-sample emissions were acquired using 10 mm quartz cells in the standard right-angle geometry, whereas monoliths were mounted on a homemade rotation stage with masks for tests in different geometries. Photoluminescence quantum yields (**PLQY**) of the QDs in toluene were measured by the relative method as described in an IUPAC technical report, with POPOP in cyclohexane (PLQY = 0.97) serving as the reference standard.[145] In short, photoluminescence (under 350 nm excitation) and absorbance spectra were recorded for a series of dilute solutions with different concentrations. The integrated PL intensities were plotted against the absorbance at 350 nm for both QD and POPOP solutions. PLQY of the QD were given by:

$$\Phi_{QD} = \Phi_{POPOP}\left(\frac{Grad_{QD}}{Grad_{POPOP}}\right)\left(\frac{n_{QD}^2}{n_{POPOP}^2}\right) \quad (4.1)$$

where Φ, Grad, n are the PLQY, slope of the curve for integrated PL intensity vs. absorbance, and refractive index of the solvent, respectively.

4.2.5 Calculation of FRET distance R_0

The FRET efficiency of a single donor-acceptor pair is given by[146]

$$F = \frac{k_t}{k_t + k_D} \tag{4.2}$$

where k_t and k_D are the donor-acceptor FRET rate and intrinsic donor radiative decay rate, respectively, with

$$k_t = \frac{1}{\tau_D}\left(\frac{R_0}{R}\right)^6 \tag{4.3}$$

and

$$k_D = \frac{1}{\tau_D} \tag{4.4}$$

where τ_D, R_0 and R are the donor's intrinsic fluorescence decay lifetime, FRET distance, and donor-acceptor distance, respectively. By substituting (4.3) and (4.4) into (4.2), we have

$$F = \frac{1}{1 + \left(\frac{R}{R_0}\right)^6} \tag{4.5}$$

It can now be seen that when $R = R_0$, the FRET efficiency of this donor-acceptor pair is equal to 50%.

The QD-FBtF FRET distance R_0 was calculated using the UV-vis absorption and PL results of both FBtF and BMEP-modified CZS QDs by the following equation from IUPAC Gold Book:[147]

$$\frac{R_0}{\text{nm}} = 2.108 \times 10^{-2} \left\{ \kappa^2 \Phi_{QD} n^{-4} \int \bar{I}_{QD}(\lambda) \left[\frac{\varepsilon_{FBtF}(\lambda)}{\text{dm}^3\text{mol}^{-1}cm^{-1}} \right] \left(\frac{\lambda}{nm} \right)^4 d\lambda \right\}^{1/6} \quad (4.6)$$

where κ^2, Φ_{QD}, n, $\bar{I}_{QD}(\lambda)$, $\varepsilon_{FBtF}(\lambda)$ and λ are the dipole-dipole orientation factor (2/3 in this case since the orientation should be random), PLQY of BMEP-modified QDs (0.774), average refractive index of the matrix (1.59 for PVT at 425 nm), QD emission spectrum normalized to an area of 1, molar extinction coefficient of FBtF, and wavelength, respectively. It should be noted that the refractive index used here is an approximation since it did not account for the influence from the high-refractive-index CZS QDs (*n*20/D = 2.37, 17.5 vol% in a 60 wt% nanocomposite monolith) and the low-refractive-index organic ligands (OA and BMEP, *n*20/D = 1.46, comprising a total of 22.1 vol% in a 60 wt% nanocomposite monolith).

4.2.6 Calculation of overall FRET efficiency $E_{overall}$

The FRET of a donor to multiple acceptors in a homogeneous solution without donor-acceptor diffusion and restricted geometry has been well studied. The relative steady-state quantum yield of donor is given by[146,148]

$$\frac{I_{DA}}{I_D} = 1 - \sqrt{\pi}\gamma \exp(\gamma^2)[1 - \text{erf}(\gamma)] \quad (4.7)$$

where

$$\text{erf}(\gamma) = \frac{2}{\sqrt{\pi}} \int_0^{\gamma} \exp(-x^2)\, dx \quad (4.8)$$

with $\gamma = C/C_0$, where C is the molar concentration of acceptor with C_0 being the characteristic molar concentration of acceptor expressed as

$$C_0 = \left(\frac{2}{3}\pi^{3/2} N_A R_0^3\right)^{-1} \tag{4.9}$$

Where N_A and R_0 denote Avogadro's Constant and the FRET distance, respectively.

The overall FRET efficiency $F_{overall}$ was then given by:

$$F_{overall} = 1 - \frac{F_{DA}}{F_D} = \sqrt{\pi}\gamma \exp(\gamma^2)[1 - \mathrm{erf}(\gamma)] \tag{4.10}$$

It should be noted that the usage of this formula assumed no restricted geometry, i.e. the donor-acceptor distance could be anywhere from 0 to infinity. In the real case for CZS QD/FBtF/polymer nanocomposite system, there would be a minimum spacing between an exciton located in a QD to an FBtF molecule, since the exciton should only reside within the $Cd_xZn_{1-x}S$ core of the core-shell QD. The minimum possible donor-acceptor distance could then be taken as the shell thickness of QD, assuming that 1) the exciton could be at any place within the core and 2) FBtF could be found right outside the QD shell embedded amongst the ligands. Since the shell thickness of 1.25 nm as estimated before was much smaller than the 4 nm FRET distance (99.9% efficiency of single donor-acceptor pair at this distance), the overestimation brought by the above formula should not be very significant. More accurate calculation should be viable with Monte Carlo simulation, but it would be beyond the scope of this dissertation and was thus not further discussed.

4.2.7 Gamma scintillation measurement

Gamma scintillation measurement was performed using a home-built system in a dark box as described in the previous chapter. In a typical measurement, a 1-cm-diameter 2-mm-thick sample was first placed in a customized PTFE sample holder and then coupled to a Hamamatsu R878 PMT using optical grease. A Cs-137 source (662 keV characteristic γ energy) of 10 μCi activity (3.7×10^5 decays/second) was then placed right outside the PTFE sample holder. The PTFE sample holder was used to optimize photon collection by PMT and to exclude the influence of concomitantly emitted β rays from the Cs source. The PMT was equilibrated for 30 min after sealing the dark box. Typical acquisition live time was set to one hour. The signal was recorded by a Canberra Lynx multichannel analyzer with rise time and flat top time set to 1 μs and 0.5 μs, respectively. Light yields of the scintillators were obtained by first comparing the sample's Compton edge channel number to that of a standard EJ-212 sample tested under the same conditions, followed by correction with regard to the PMT's spectral sensitivity using the as-obtained transmission-mode PL spectra. In this manner, the light yields were calculated using the following formula:

$$LY_{NC} = LY_{EJ-212}\left(\frac{CE_{NC}}{CE_{EJ-212}}\right)\left(\frac{\phi_{EJ-212}}{\phi_{NC}}\right) \tag{4.11}$$

where LY, CE, and ϕ represent the light yield, channel number of the Compton edge, and the PMT-sensitivity correction factor, respectively. A light yield of 10,000 photons/MeV for EJ-212 was used per the product specification. The PMT-sensitivity correction factor ϕ_x for sample *x* was computed using the following formula:

$$\phi_x = \frac{\int \varphi(\lambda)\, I_x(\lambda) d\lambda}{\int I_x(\lambda) d\lambda} \tag{4.12}$$

where $\varphi(\lambda)$ and $I_x(\lambda)$ are the PMT's quantum efficiency and the sample's emission intensity at wavelength λ, respectively.

4.2.8 Time resolved radioluminescence decay lifetime measurement

Time resolved radioluminescence decay curves were measured using a home-built time-correlated single photon counting (**TCSPC**) system described by Hajagos *et al.*[149] The measurement uses a Hamamatsu H2431-50 assembly as the start PMT and a Hamamatsu H10721P-110 module fitted with an E5776-51 SMA fiber optic adapter as the stop PMT. The sample was placed in a homemade PTFE sample holder and directly coupled to the start PMT using optical grease, with a bare terminated 800 μm multi-mode fiber inserted through a tightly fitting hole on the PTFE sample holder to conduct single photons from the sample to the stop PMT. The 10 μCi Cs-137 source was then placed near the PTFE sample holder. Similarly, the PMTs were equilibrated for 30 min after the dark box was sealed. Signal from the stop PMT was fed into an Ortec Model 9326 fast preamplifier, and the resulting output along with the signal from the start PMT was digitized using a PicoScope Model 5244B oscilloscope (Pico Technology, Inc.). The differences in arrival times between the main pulses detected by the start PMT and the single photon pulses detected by the stop PMT were histogrammed to obtain the scintillation decay curves over a 250-ns interval.

4.2.9 Fitting of radioluminescence decay curves

Radioluminescence decay curves displayed in Figure **4e** and **4f** were fitted using the double-exponential decay functions as described below:

$$I = A_{fast}e^{-\frac{t}{\tau_{fast}}} + A_{slow}e^{-\frac{t}{\tau_{slow}}} \quad (4.13)$$

where I, A and τ denote intensity, the amplitude and characteristic decay lifetime, respectively. The slow component fraction (f_{slow}) denotes the percentage of slow emission intensity within total emission and is calculated as:[146]

$$f_{slow} = \frac{A_{slow} \times \tau_{slow}}{A_{slow} \times \tau_{slow} + A_{fast} \times \tau_{fast}} \quad (4.14)$$

It should be noted that the slow component lifetime for the bare 2% FBtF/PVT monolith cannot be very well fitted due to low signal level. Therefore, the tail is used to indicate the noise level, which is about 6.3% of the total emission.

4.3 Results and Discussion

4.3.1 Scintillation mechanism for QD-based nanocomposite scintillator

Figure 4.1 shows a simplified schematic of the scintillation process involved in the QD/dye/polymer nanocomposite scintillator. A γ photon is first converted at QD site into a photoelectron with all energy of the photon. The photoelectron with high kinetic energy then cascades to produce a number of low-energy excitons via collisional energy exchange with the ground-state electrons on its trajectory. Depending on where the excitons are generated, they would take different FRET routes to transport and eventually be converted into visible photons at the dye sites. As dictated by the decreasing band gaps from PVT matrix (4.2 eV) to CZS QDs (2.84 eV) then to FBtF (2.56 eV), excitons generated in PVT can either be directly transferred to FBtF as shown in route 1, or to be first transferred to a nearby CZS QD as in route 3, depending on the relative proximity from the generated exciton to the closest QD and FBtF. Excitons in CZS QDs, either generated therein (route 2) or transferred from PVT matrix (route 3), quickly decay in energy

through internal conversion to its $Cd_xZn_{1-x}S$ core due to the QD's type I core/shell structure, and then transfer to FBtF via FRET. The excitons collected at FBtF sites finally recombine radiatively to produce visible photons to be detected by the PMT. It should be noted that the band structure and FRET sequences shown above should be quite generic for all efficient QD/polymer nanocomposite scintillators due to following two reasons: 1) most matrix monomers with some conjugated structures and reasonably low melting points (for the ease of fabrication) have larger band gaps than QDs with a reasonably high PLQY; 2) suppression of QD self-absorption requires the use of a lower band gap dye at rather high concentration to facilitate efficient FRET.

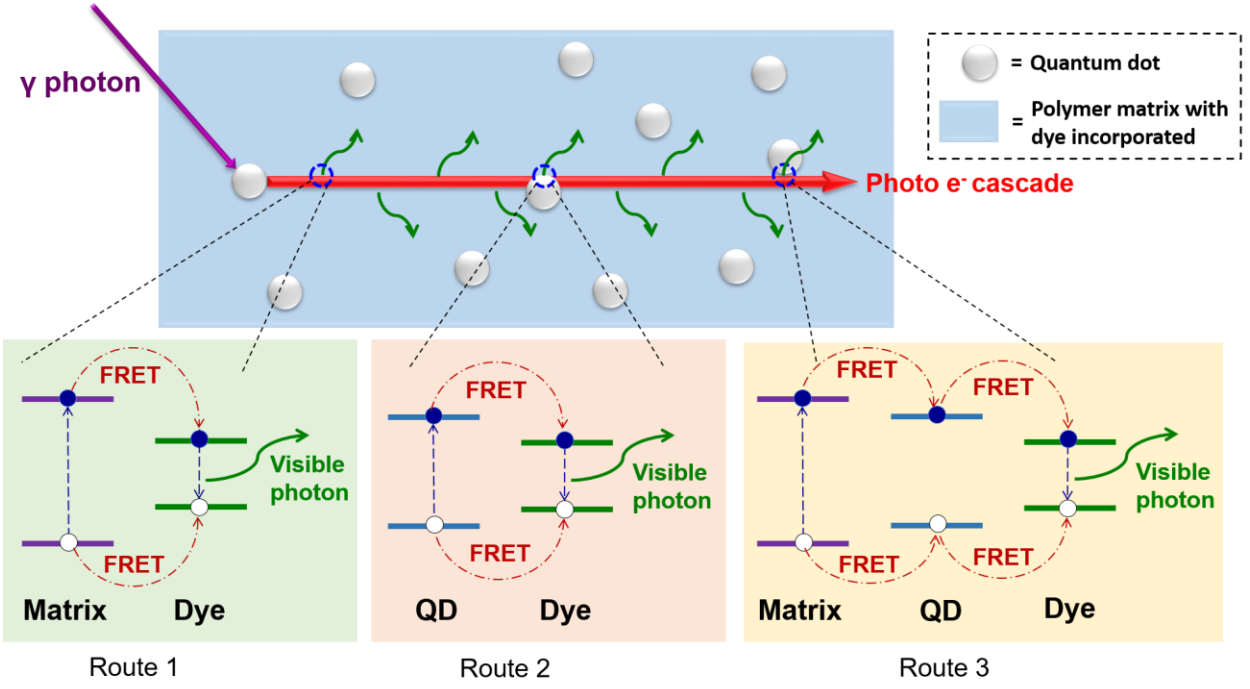

Figure 4.1 Schematic illustration of the scintillation process and major FRET routes involved in a QD/dye/polymer ternary system.

4.3.2 Synthesis and surface modification of CZS QDs

CZS QDs are synthesized following a well-developed protocol using a typical air-free Schlenk setup.[56,129] **Figure 4.2** shows the TEM image and XRD pattern of pristine CZS QDs. The QDs

have a uniform size distribution and are around 6 nm in diameter. Assuming that all Cd precursor (1 mmol) is depleted during the 2 mmol S/ODE injection to form $Cd_{0.5}Zn_{0.5}S$ cores, and that the additional 8 mmol S/TBP precursor is all consumed in ZnS shell formation, an estimated core radius of 1.75 nm can be obtained. XRD pattern of the QDs shows a close match with that of cubic $Cd_{0.1}Zn_{0.9}S$ (JCPDS file 00-024-1137). TGA test (**Figure 4.3**) of the QDs in air shows a 35% loss in weight at 750 ^{o}C, a temperature high enough for all oxidation and decomposition to happen. The slightly-yellowish white remnant was taken for EDX test, where only Cd, Zn and O were found, indicating a complete removal of all surface ligands and total oxidation of $Cd_xZn_{1-x}S$ into $Cd_xZn_{1-x}O$. Weight percentage of $Cd_xZn_{1-x}S$ (**CZS%**) in the original surface ligand wrapped QD was then calculated using the final weight percentage of $Cd_xZn_{1-x}O$ (**CZO%**) and the molecular weight of CZS and CZO ($\mathbf{MW_{CZS}}$ and $\mathbf{MW_{CZO}}$), as follows:

$$CZS\% = CZO\% \times \left(\frac{MW_{CZS}}{MW_{CZO}}\right) \tag{4.15}$$

It should be noted that the fraction x for Cd is set to 0.1 for calculation. This should be the case since the more reactive Cd should be completely depleted during the first S/ODE injection and the overall molar ratios of Cd:Zn:S precursors (total amount in both ODE and TBP) are 1:10:10. CZS% was then calculated to be 77%, indicating that 23% of the total QD weight came from wrapping ligands.

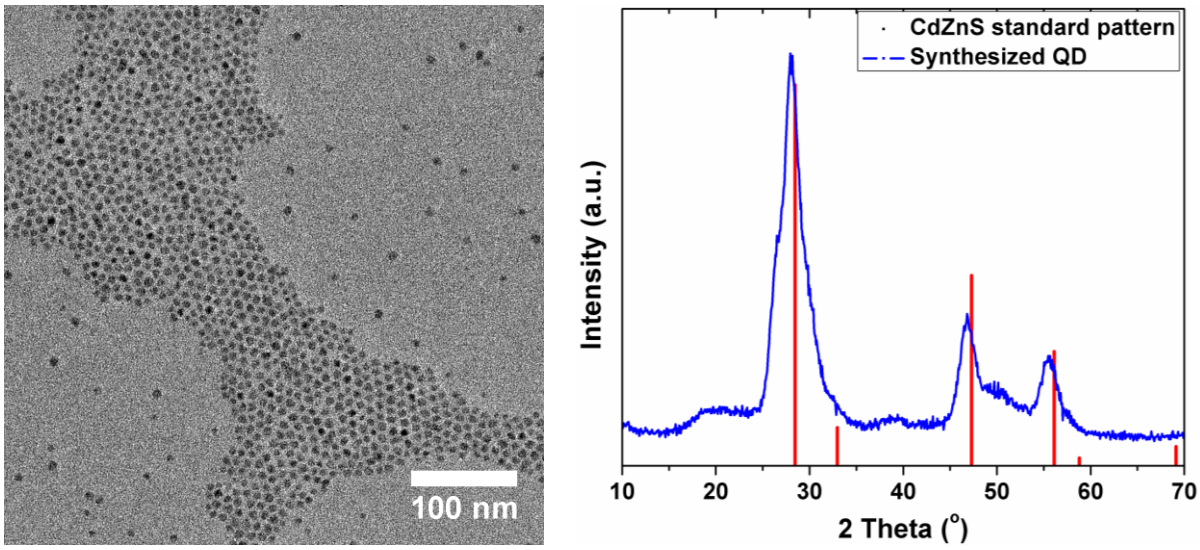

Figure 4.2 TEM image (left) and XRD pattern (right) of pristine CZS QDs.

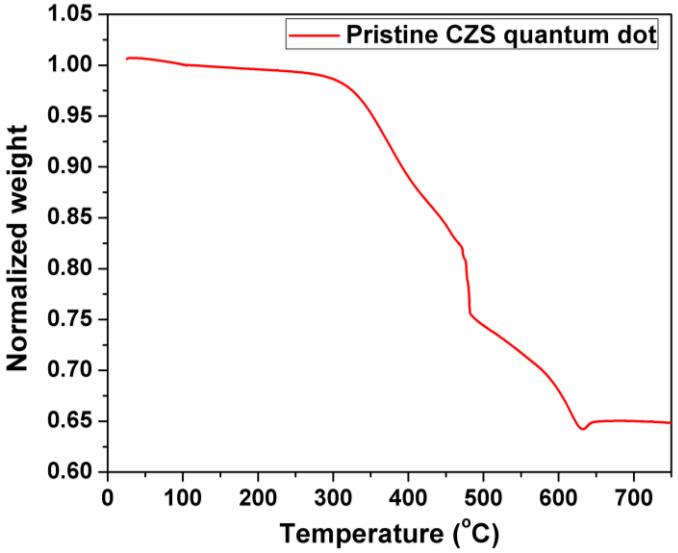

Figure 4.3 TGA curve of pristine CZS QDs.

Wrapping ligand on the QD surface is determined by EDX and FTIR. EDX of the pristine QD showed an approximate 10:1 ratio of C:O with no P present. Of the possible ligand species present

in the reaction—ODE, OA, acetate ion and TBP—the lack of P in EDX excluded TBP, while the large C:O ratio excluded both acetate and ODE, leaving OA, or oleate ion to be more accurate, the only possible wrapping ligand. FTIR spectrum of the pristine QD (**Figure 4.4**) confirmed the existence of oleate ion. The main peak at 1546 cm^{-1} and the shoulder peak at 1430 cm^{-1} could be attributed to asymmetric and symmetric vibrations of the chelating COO^- ion. The strong peaks at 1465 cm^{-1}, 2853 cm^{-1} and 2963 cm^{-1} were ascribed to alkane C-H bending and stretching vibration, whereas the weak peak at 3009 cm^{-1} was alkene C-H stretching vibration peak. The above characteristics indicate oleate ion as the chelating ligand on QD surface.

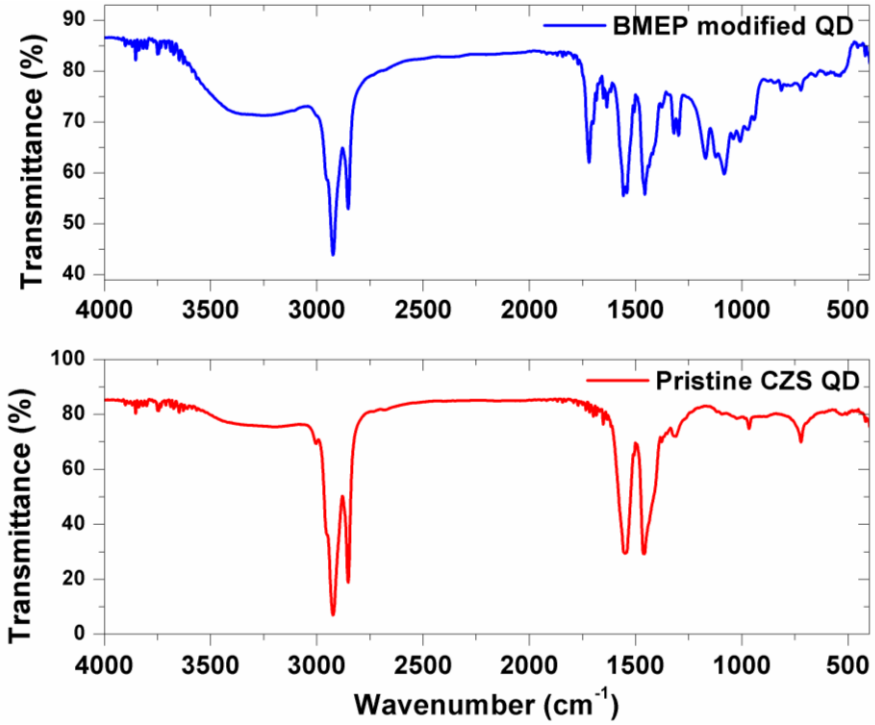

Figure 4.4 FTIR spectra of pristine and BMEP-modifed CZS QDs.

Partial BMEP exchange was carried out in a similar manner as described in the previous chapters.[103,125] The amount of BMEP ligand used was determined using the following formula:

$$m_{BMEP} = m_{QD} \times OA\% \left(\frac{MW_{BMEP}}{MW_{OA}}\right) \times \frac{1}{3} \quad (4.16)$$

Where m_{BMEP}, m_{QD}, OA%, MW_{BMEP}, MW_{OA} are mass of BMEP, mass of QD, wt% of OA ligand on QD as determined via TGA, molecular weight of BMEP and molecular weight of OA, respectively. The factor of 1/3 indicates that only 1/3 of the OA ligand molecules will be exchanged. The reaction should proceed almost stoichiometrically as the phosphate group has a much stronger anchoring capability than OA. In fact, dropping rate of the BMEP solution needed to be kept low due to the fast reaction between BMEP and QD, as evident by the appearance of white precipitates if BMEP was added too fast. By slowly adding BMEP into QD solution, only a very small amount of precipitates appears. Careful washing with toluene/acetone and hexane/acetone removes residual unreacted BMEP and exchanged OA, whereas syringe-filtration removes the white precipitates. The partial-BMEP-modified QDs have excellent solubility in VT, as evident by the formation of a clear VT solution containing 60 wt% QD only shortly after sonication. FTIR of the partial-BMEP-modified QDs showed a series of new peaks in addition to the old oleate peaks. The peaks at 1718 cm^{-1} and 1638 cm^{-1} could be attributed to the C=O and C=C vibrations of methacrylate group on BMEP, whereas the peaks at 1314, 1292, 1174, 1131, and 1076 cm^{-1} could be ascribed to the vibrations of C-O, P=O and P-OR groups from BMEP. The combination of these new peaks with the rather strong old peaks indicated the coexistence of BMEP and OA on the QD surface, confirming the efficacy of partial BMEP exchange.

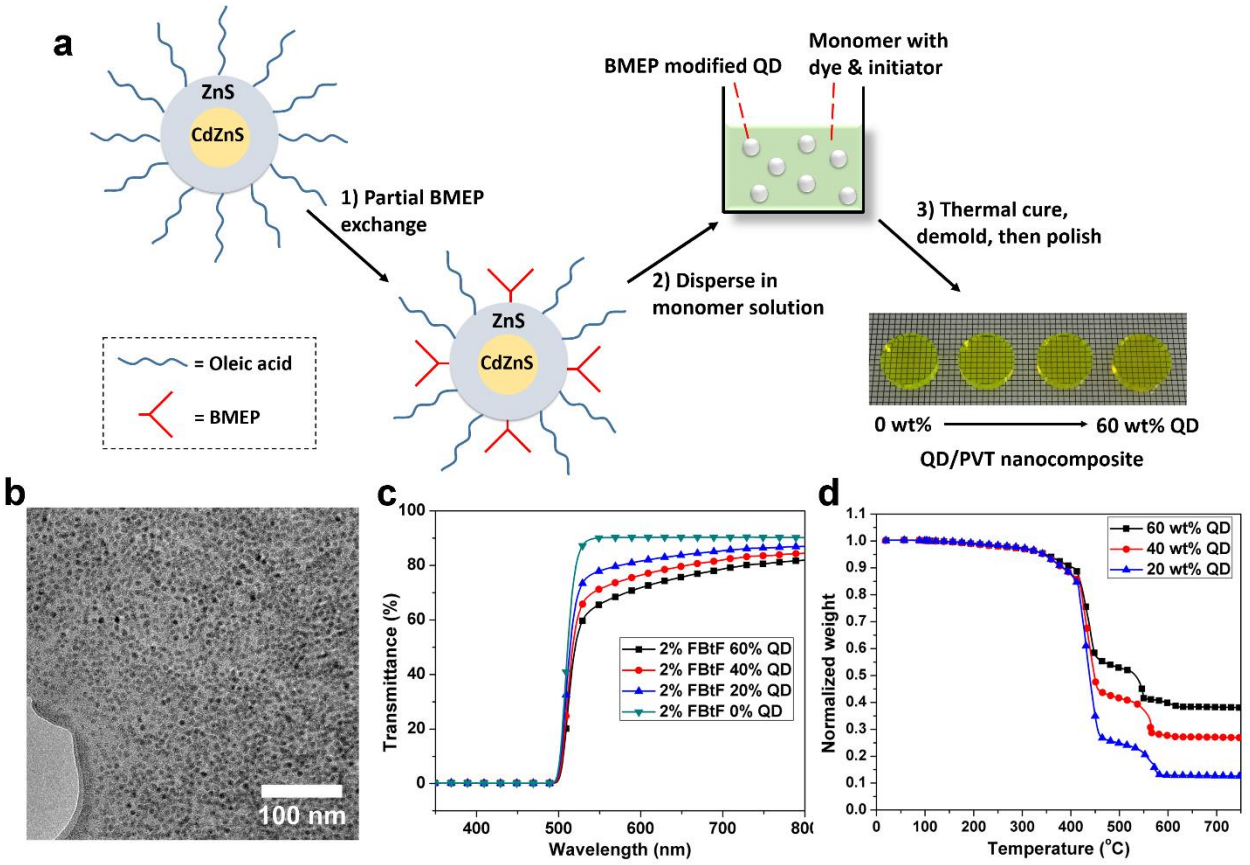

Figure 4.5 a, Schematic illustration of the partial surface modification-*in situ* copolymerization process for fabricating ultra-high-loading QD/polymer nanocomposite monoliths. The last frame is a photograph of nanocomposite monoliths (2 mm thick by 1 cm diameter) with 2% FBtF and varying QD loadings from 0% to 60% at a 20 % increment. **b,** TEM image of an FIB-etched thin film from a 60 wt% QD/PVT nanocomposite monolith. Film thickness is approximately 50 nm, with the lower-left part being thinner and upper-right thicker. **c,** UV-vis transmittance curves of the QD/PVT nanocomposite monoliths shown in **a**. **d.** TGA curves of the monoliths.

4.3.3 Fabrication of QD/polymer nanocomposite scintillator

To realize scintillation detection using the as-described nanocomposite structure, aggregation of QDs in polymer matrix has to be minimized due to the needs for a successful out-coupling of photons and an efficient QD-dye FRET which requires a donor-acceptor spatial proximity of 1-10 nm.[103,146] To achieve this goal, a partial surface modification-*in situ* copolymerization process was

developed based on works developed in the previous chapters (**Figure 4.5a**). The partial BMEP-modification endowed QDs with surface-grafted mathacrylate monomer groups while retaining the QD's solubility in the low-polarity VT monomer solution. It should be noted that the PLQY of CZS QD decreased only slightly from 83.8% to 77.4% after partial BMEP modification, which could be ascribed to the protective ability of ZnS shell against the small amount of BMEP used. The as-modified QDs were then dissolved in VT along with FBtF and thermal initiator to form an optically clear solution. Afterwards, the solution was heated to initiate the *in situ* copolymerization, where the surface-grafted mathacrylate groups copolymerize with VT to provide covalent linkage between the QDs and polymer, thus alleviating the aggregation of QDs. As shown in **Figure 4.5a**, the as-fabricated nanocomposite monoliths were highly transparent with CZS QD loadings of up to 60 wt% (including surface ligand, all QD percentages from here on are weight percentages including ligand, if not specified), indicating a uniform dispersion of QDs within the matrix, which is further confirmed by transmission electron microscopy (TEM) on a focused-ion-beam etched thin film from a 60% QD nanocomposite monolith (**Figure 4.5b**). UV-vis transmittance test results (**Figure 4.5c**) confirmed the good transparencies of these ultra-high-loading nanocomposite monoliths, where the 60% QD nanocomposite monolith showed a transmittance of 65.8% at 550 nm. The slight decrease of transmittance at larger QD% and shorter wavelength is due to intensified Rayleigh scattering caused by the addition of QDs, since the refractive index of CZS QDs (>2.39 at 550 nm) is much higher than that of the PVT matrix (1.59 at 550 nm).[81] The high QD loadings in these nanocomposite monoliths were confirmed by TGA tests in air at up to 750 ^{o}C (**Figure 4.5d**). Considering the QD's weight loss of 35% under the same TGA condition due to loss of ligand and conversion of $Cd_xZn_{1-x}S$ to $Cd_xZn_{1-x}O$ (Supplementary Note 1), the final weight percentages of 38.1%, 26.9% and 12.6% matched well with the predetermined QD loadings

of 60%, 40% and 20%, confirming the efficacy of this protocol in fabricating transparent ultra-high-loading QD/polymer nanocomposite monoliths.

4.3.4 FRET of QD/dye/polymer nanocomposite

As mentioned before, a key advantage of using QDs as the high-Z additive is that their high PLQY should enable efficient conversion of energy deposited therein into detectable photons. However, severe self-absorption of QDs due to their small Stokes shift often results in drastically decreased PL at high QD concentrations. To suppress QD self-absorption, organic dyes with large Stokes shift and great absorption at QD emission wavelengths were added to facilitate efficient FRET from QDs. **Figure 4.6** shows the normalized absorption and PL spectra of CZS QD and the dye, FBtF, a fluorene-derivative that has demonstrated its use as an efficient dye in a work by Kishpaugh *et al.*[144] The narrow violet emission of CZS QD centering at 425 nm fell exactly within the absorption peak of FBtF ($\varepsilon_{(417\ nm)}$ = 21595 $M^{-1}\cdot cm^{-1}$), implying a great potential for an efficient QD-to-FBtF FRET. Moreover, the significantly larger absorbance of FBtF also ensured, if any, a more competitive absorption of the QD emission, thus further alleviating the QD self-absorption. In addition, the emission of FBtF had negligible overlap with the QD absorption, rendering both exciton back-transfer and the reabsorption of FBtF-emitted photons by QDs unlikely. These spectral characteristics suggest an efficient, unidirectional FRET from QDs to FBtF, which would alleviate QD self-absorption and help extract QD-borne excitons for photon production.

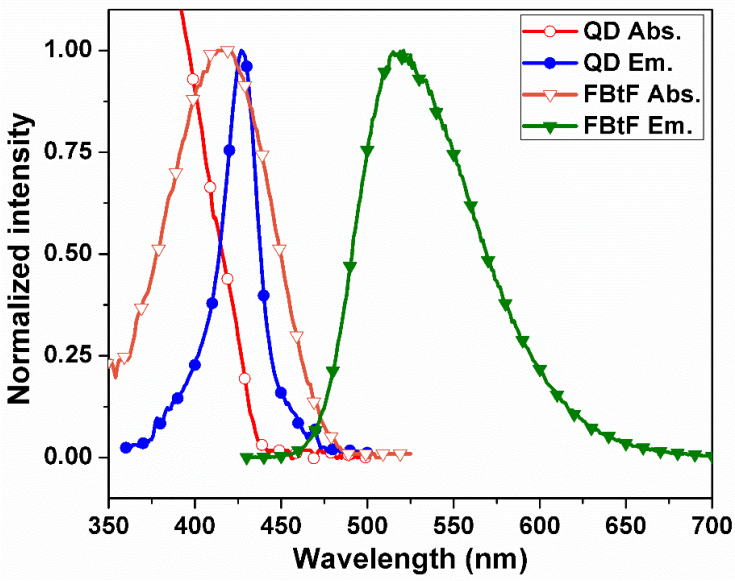

Figure 4.6 Normalized UV-vis absorbance and PL spectra ($\lambda_{exc\ QD}$ = 350 nm, $\lambda_{exc\ FBtF}$ = 420 nm) of $Cd_xZn_{1-x}S/ZnS$ core/shell quantum dot and FBtF in dilute solutions. Absorbance spectra were mass-concentration normalized, and the normalized absorbance for QDs was further multiplied by 30 to qualitatively account for the weight differences between CZS QDs and FBtF in a 60% QD/2% FBtF nanocomposite monolith.

It should be noted that the overall FRET rate from PVT matrix to QD and FBtF acceptors should be, if not more efficient, at least comparable to the PVT-dye FRET in traditional plastic scintillators, because 1) both FBtF and QD have very strong absorbance at PVT's emission maximum of 310 nm (**Figure 4.7**) and 2) the average distance from a generated exciton on PVT to the closest QD or FBtF in a 60% QD/2% FBtF nanocomposite scintillator should be much smaller compared to the case for a traditional plastic scintillator containing nothing else but 2% primary dye. For this reason, FRET from PVT is assumed to be "efficient", and the QD-to-FBtF FRET efficiency is studied as the key variable for scintillator performance.

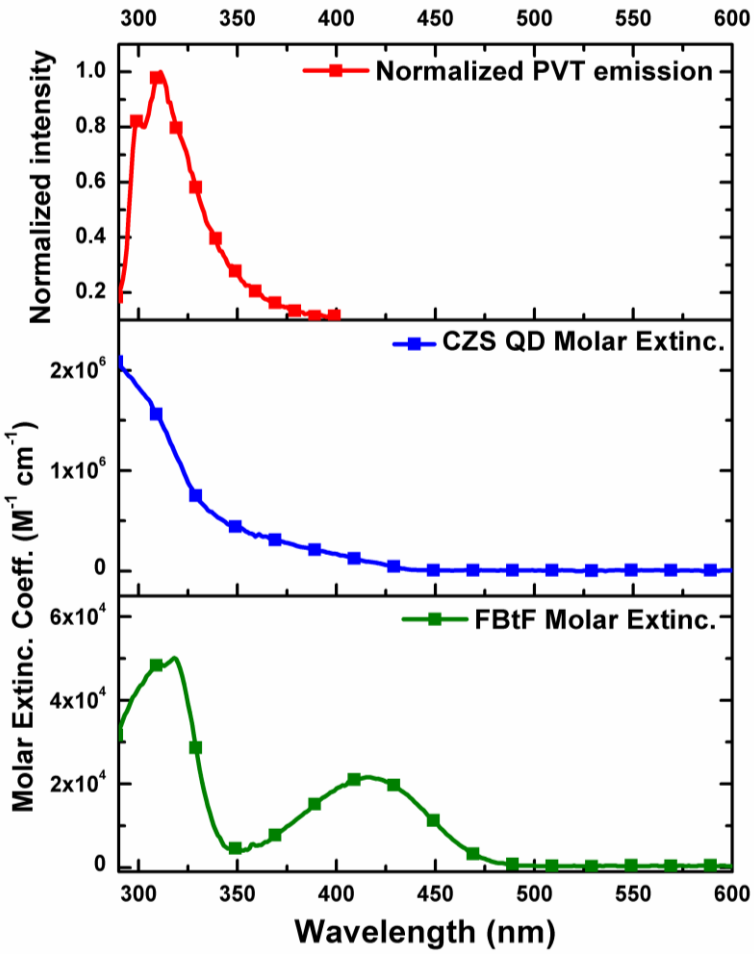

Figure 4.7 Normalized PL spectrum of PVT, and curves of the molar extinction coefficients of CZS QD and FBtF. The "molecular weight" of QD was derived by multiplying the weight of an individual QD to Avogadro's Constant. The weight of an individual QD was calculated using the TEM-measured radius of QD, density of QD (ZnS density of 4.09 g/cm^3 was used as a conservative approximation), and the TGA-determined ligand% on QD.

PL spectroscopy is then used to characterize the QD-to-FBtF FRET efficiencies of nanocomposite monoliths with varying concentrations of FBtF and CZS QDs. Since efficient FRET requires a close spatial proximity (< 10 nm) between the donor QD and acceptor FBtF, a high concentration of FBtF (> 1 wt%) is needed in the nanocomposite. However, an excessively high concentration

of FBtF also increases dye self-absorption in the monolith, which would decrease LY. A series of nanocomposite monoliths containing 50% QD and 1% to 5% FBtF were then fabricated to probe the optimal FBtF concentration. Due to the high concentration of FBtF, conventional right-angle setup (or transmission-mode as shown in **Figure 4.8**) cannot be used to test FRET since all QD emission would eventually be absorbed by FBtF in the bulk. As a result, surface-mode PL setup (**Figure 4.8**) is used to qualitatively study the FRET efficiencies in these monoliths.

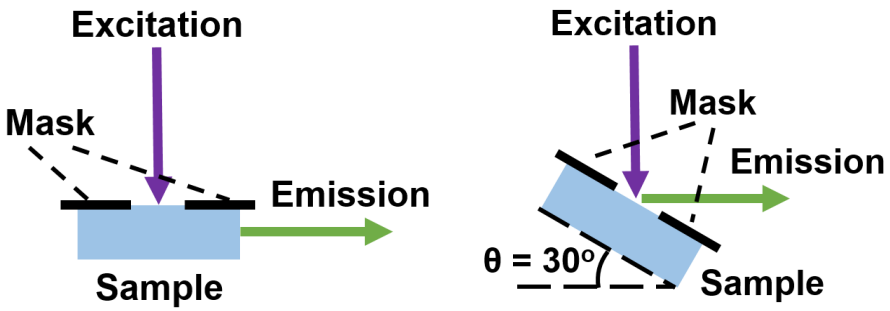

Figure 4.8 Schematic illustrations of the transmission-mode (**left**) and surface-mode (**right**) PL setups.

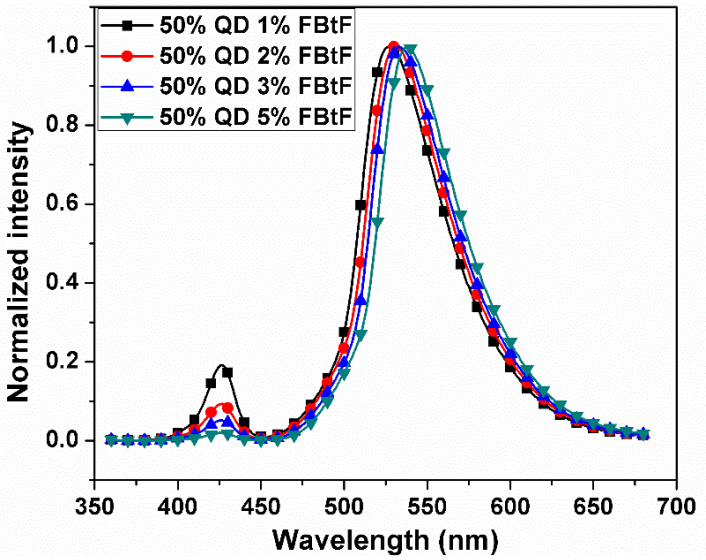

Figure 4.9 Normalized surface-mode PL spectra (λ_{exc} = 350 nm) of 50% QD/1-5% FBtF/PVT nanocomposite monoliths.

At the excitation wavelength of 350 nm, QDs are the major absorbing species in nanocomposite monoliths due to their significantly greater absorbance compared to FBtF (**Figure 4.6**) and the non-absorbing PVT (E_g = 4.2 eV). Therefore, excitons were generated mainly in the QDs within a shallow layer of around 10 μm thick, as estimated using the extinction coefficient and concentration of the QDs. By comparing the QD emission to total emission intensity, FRET efficiencies could be estimated. It should be noted that this method gave only qualitative estimations, since the influence from various other processes such as absorption-reemission and scattering could hardly be excluded. As shown in **Figure 4.9**, QD emission intensity decreased with the addition of FBtF, indicating an improved FRET efficiency. However, the effect of QD emission quenching diminishes at higher FBtF concentrations (**Figure 4.10**). This could be attributed to the saturation of FRET at high acceptor concentrations. The overall FRET efficiency $\mathbf{F_{overall}}$ from a QD to any one of its surrounding FBtF molecules can be expressed as:[146]

$$F_{overall} = \frac{\sum_i k_{ti}}{\sum_i k_{ti} + k_D} = \frac{\frac{1}{\tau_D}\sum_i \left(\frac{R_0}{R_i}\right)^6}{\frac{1}{\tau_D}\sum_i \left(\frac{R_0}{R_i}\right)^6 + \frac{1}{\tau_D}} = \frac{\sum_i \left(\frac{R_0}{R_i}\right)^6}{\sum_i \left(\frac{R_0}{R_i}\right)^6 + 1} \quad (4.17)$$

where k_{ti}, k_D, τ_D, R_0 and R_i are the FRET rate between QD and the *i*th nearby FBtF acceptor, radiative recombination rate of QD exciton in the absence of acceptors, fluorescence decay lifetime of QD in the absence of acceptors, characteristic FRET distance (4.02 nm as calculated using methods described in section 4.2.5), and the distance between donor QD and the *i*th FBtF molecule, respectively. At high FBtF concentrations, $\sum_i(R_0/R_i)^6 >> 1$, and $F_{overall}$ approaches 1, rendering excessive FBtF redundant. A preliminary calculation using the equations in section 4.2.6 showed that $F_{overall}$ increased from 92.2% at 1% FBtF to 97.7% at 2%, confirming the as-mentioned FRET saturation. Considering the rise of FBtF self-absorption at higher concentrations, which was

evident by the 10-nm-redshift of FBtF emission peak when its concentration was increased from 1% to 5%, an FBtF concentration of 2% was chosen as the optimal concentration for further fabrications and tests.

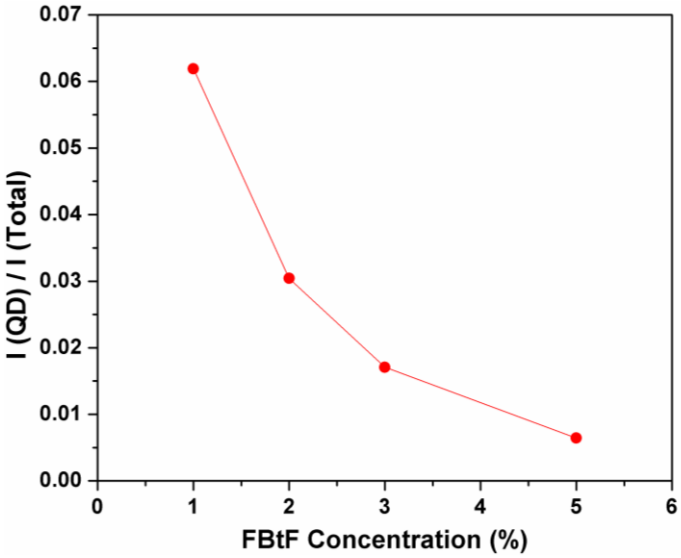

Figure 4.10 Ratios of integrated emission intensities between QD and (QD + FBtF) at different FBtF concentration.

Using the optimal FBtF concentration of 2%, another series of nanocomposite monoliths containing 0-60% CZS QD were also fabricated and tested. As shown in **Figure 4.11**, the relative intensity of QD emission remained almost identical when the QD% increased from 20% to 60%, indicating a similarly efficient QD-to-FBtF FRET with 2% FBtF. In addition, no obvious quenching of the FBtF emission was observed at larger QD%, as evident by the bright green emission of all nanocomposite monoliths under 365 nm UV illumination (**Figure 4.12**). The FBtF emission only redshifted slightly from 529 to 531 nm as the QD concentration amounted to 60%, implying a similar level of self-absorption.

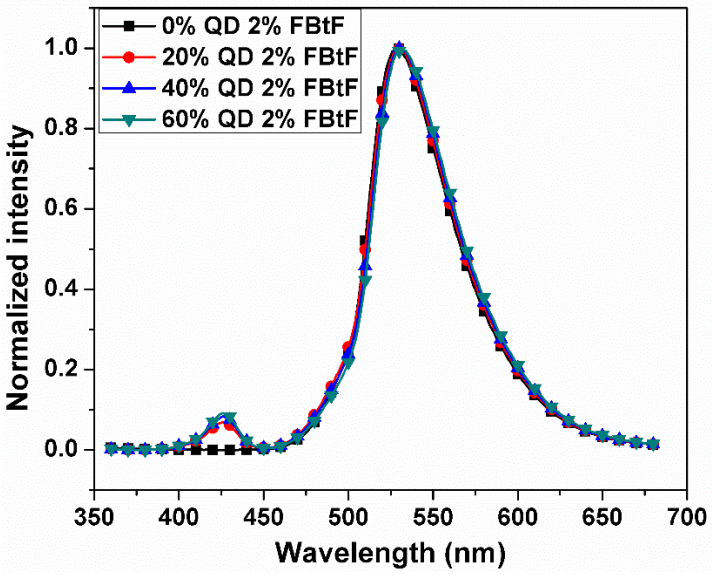

Figure 4.11 Normalized surface-mode PL spectra (λ_{exc} = 350 nm) of 0-60% QD/2% FBtF/PVT nanocomposite monoliths.

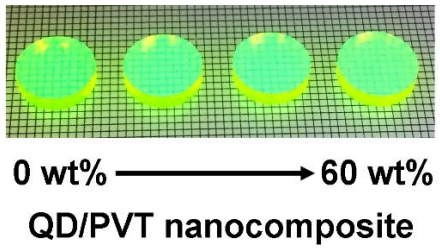

Figure 4.12 Photograph of the 0-60% QD/2% FBtF/PVT nanocomposite monoliths under 365 nm UV illumination.

To further study the effect of self-absorption within the bulk, transmission-mode PL spectra of these monoliths were also obtained. As shown in **Figure 4.13**, similar to the surface-mode spectra, only a small redshift from 529 nm to 531 nm was observed as the QD% increased. The similar peak positions and small redshift indicated that the addition of QDs did not induce severe self-absorption by increasing scattering within the bulk. In addition, QD emission peaks disappeared in transmission-mode PL due to complete absorption by FBtF. It should be noted that, since most

photons would be generated along the fast-electron path within the bulk, these transmission-mode PL spectra should also reflect the "actual" spectra detected by PMT in scintillation tests. Therefore, transmission-mode PL spectra were used to correct the LYs with regard to PMT sensitivities, as would be shown later in this chapter.

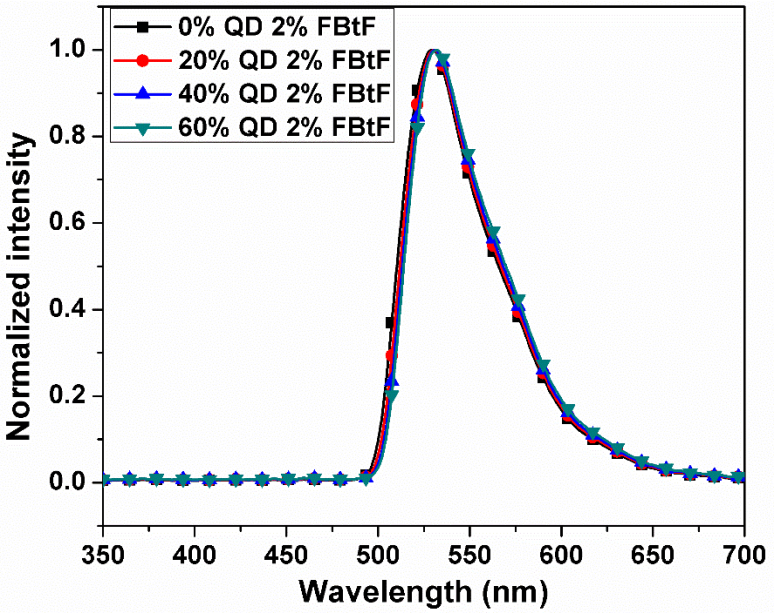

Figure 4.13 Normalized transmission-mode PL spectra (λ_{exc} = 300 nm) of 0-60% QD/2% FBtF/PVT nanocomposite monoliths.

4.3.5 Scintillation characteristics of the QD-based nanocomposite scintillator

With the effective QD-to-FBtF FRET confirmed, scintillation characteristics of the ultra-high-loading QD/FBtF/PVT nanocomposite monoliths are tested under 662 keV gamma radiation. **Figure 4.14a** shows the pulse-height spectra of nanocomposite monoliths containing 50% QD and 1-5% FBtF. The Compton edge was shifted significantly from 385 channels to 455 channels as the FBtF loading increased from 1% to 2%, displaying an improvement of 15.4% in apparent LY. However, further increasing FBtF loading from 2% to 5% saw no obvious change in LY. Such trend in LY change could be ascribed to the competition between FRET and self-absorption. The

initial LY increase at 2% FBtF could be ascribed to the significantly improved FRET efficiency compared to 1% FBtF as discussed before. However, adding more FBtF only has a limited effect on FRET, which could be offset by the steadily intensified self-absorption, resulting in the stagnation of LY. The balance between FRET improvement and self-absorption therefore made 2% FBtF the optimal concentration.

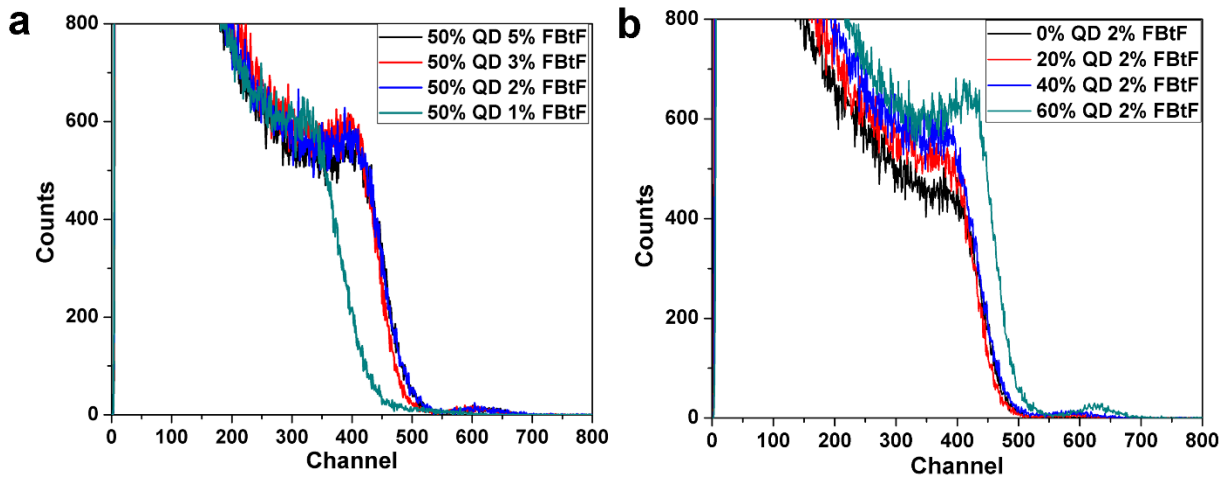

Figure 4.14 Pulse height spectra of (**a**) 50% QD/1-5% FBtF/PVT nanocomposite monoliths and (**b**) 0-60% QD/2% FBtF/PVT nanocomposite monoliths.

Pulse-height spectra of nanocomposite monoliths containing 2% FBtF and 0-60% of CZS QDs were shown in **Figure 4.14b**. LY of the nanocomposite monoliths did not decrease at larger QD%, as opposed to the case with non-emitting nanoparticle.[103,126] In contrast, a significant increase of LY was observed at 60% QD loading. By comparing the Compton Edge to that of a standard EJ212 sample and correcting the PMT sensitivity difference (**Figure 4.15**), the absolute LYs were obtained for the 0-60% QD/2% FBtF nanocomposite scintillators. As shown in **Figure 4.16**, the LY increased from 8359 photons/MeV for the bare 2% FBtF/PVT scintillator to 8490, 8714 and 9255 photons/MeV for the nanocomposite scintillators containing 20%, 40% and 60% QD, respectively, demonstrating a maximum of 10.7% improvement in LY.

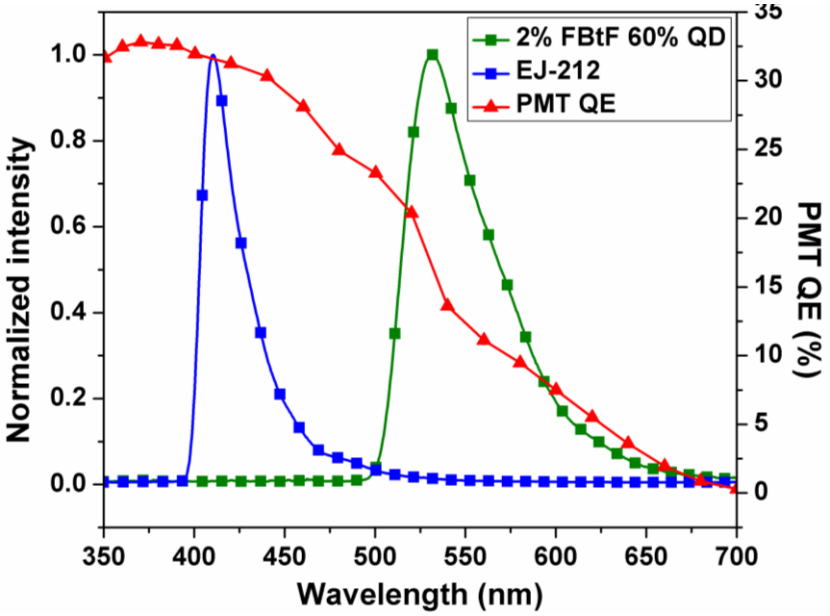

Figure 4.15 PMT spectral sensitivity and emission spectra of EJ-212 and a 60% QD/2% FBtF/PVT nanocomposite monolith.

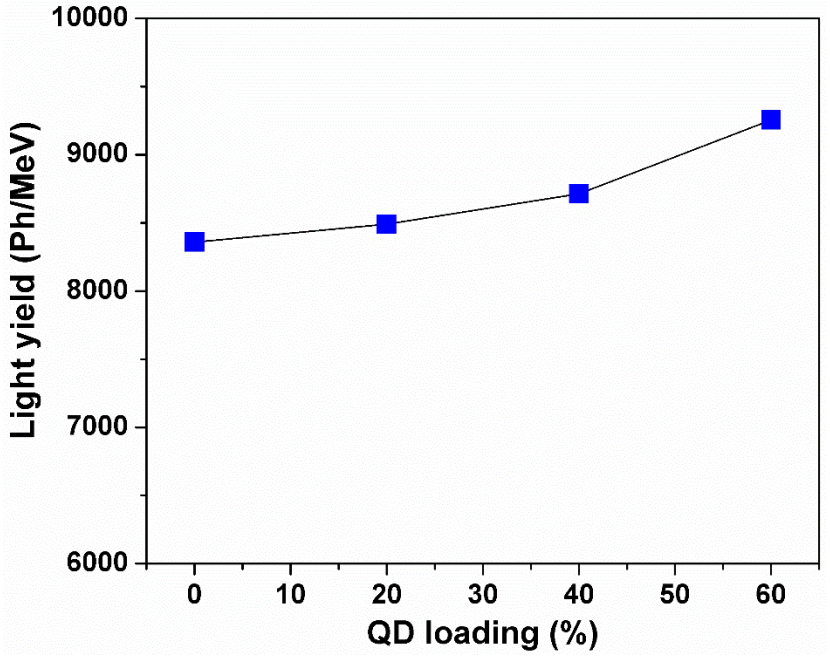

Figure 4.16 Chart of scintillation light yields of the 0-60% QD/2% FBtF/PVT nanocomposites after PMT spectral sensitivity correction.

To find out the reason for this improved LY, the LY of a composite system can be first expressed as:[2,103]

$$LY = \left(\sum_j E_j \times P_j \times F_j\right) \times \Phi_{dye} \times \left(1 - A_{dye}\right) \quad (4.18)$$

where E_j, P_j, F_j, Φ_{dye} and A_{dye} denote the percentage of energy deposited in component j (j = QD, matrix or ligand),[103] exciton productivity of component j (excitons/MeV), overall efficiency of exciton transfer from component j to dye site, PLQY of dye, and self-absorption of dye emission, respectively. Among the five factors, Φ_{dye} should remain constant regardless of QD%, while A_{dye} should increase with QD% due to intensified scattering and result in a lower LY. Since E_j is not an intrinsic property dictating exciton and photon production, the increase in LY should then be ascribed to a larger product of P_j and F_j for QD compared to the matrix, as this product for the aliphatic ligands should be close to zero due to their negligible PLQY.[2,103,126] As discussed before, FRET for excitons generated in QD and matrix should both be efficient with 2% FBtF. Therefore, the higher LY for QD/PVT nanocomposite scintillator should be mainly attributed to a larger P_j of QD compared to that of PVT. Assuming $F_{QD} = F_{Matrix}$, $P_{Ligand} \times F_{Ligand} = 0$, and no absorption loss, i.e. $A_{dye} = 0$, it is easy to obtain $P_{QD} = 1.3 \times P_{Matrix}$ using E_j's calculated as described in chapter 2, indicating a 30% higher exciton productivity. Greater exciton productivities of inorganic materials due to their smaller ionization energies had been proposed before to account for the higher LYs of inorganic scintillators; however, the exact reasons behind this still remained unknown.[2,61,62] More research, both theoretical and experimental, is needed to unravel the puzzle.

The addition of QDs also improved the Z of nanocomposite scintillators, which enabled the detection of photopeak in the pulse-height spectra. **Figure 4.17** shows the energy correlated pulse-height spectrum obtained using the 60% QD/2% FBtF/PVT nanocomposite scintillator. A full-energy peak centering at 646 keV with 9.8% resolution was observed. The small offset of 16 keV from 662 keV is due to the existence of an inseparable Cd Kα escape peak located at 639 keV, which should be eliminated at larger scintillator sizes. The energy resolution of 9.8% is not superior to previous blue-emitting scintillators, which is due to the green-emitting scintillator's lower apparent LY as-detected by the PMT.[103,126] However, it is much better than the reported 11.4% resolution of FBtF-loaded Gd_2O_3 nanocomposite scintillators, confirming the improved LY by adding QDs.[71] By using the green-sensitive Si photomultiplier for photon detection, the spectral mismatch could be eliminated, which should greatly enhance the apparent LYs and resolutions.[150]

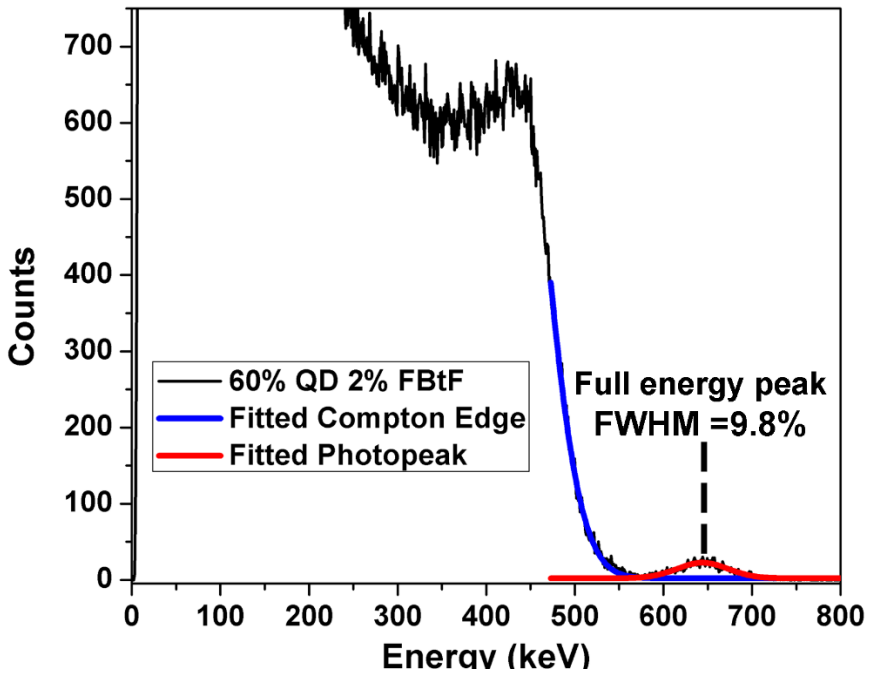

Figure 4.17 Energy correlated pulse height spectrum with fitted Compton edge and full-energy peak for a 2-mm-thick 60% QD/2% FBtF/PVT nanocomposite monolith.

In addition to the enhanced LY and Z, another promising feature of the QD/polymer nanocomposite scintillators is their retained short scintillation lifetimes. **Figure 4.18** shows the radioluminescence decay curves of 50% QD/1-5% FBtF/PVT and 0-60% QD/2% FBtF/PVT nanocomposite scintillators, respectively. The curves were fitted using a double exponential function with the results listed in **Table 4.1**. All nanocomposite scintillators displayed a dominating fast emission with around 7 ns lifetimes, which was from FBtF as evident from the 2% FBtF/PVT sample. The lifetime of this fast component decreased with increasing FBtF% or QD%, which could be ascribed to an intensified FBtF self-absorption due to higher dye loading or enhanced scattering, respectively. In addition to the fast component, a minor slow component with around 70 ns lifetimes was also observed. The intensity of this slow emission increased with additional QD but decreased at higher FBtF%. In addition, the lifetime of slow decay decreased at higher FBtF% and QD%. Since the typical PL lifetime of CZS core/shell QD is around 10-15 ns, which should further be significantly reduced due to strong FRET to FBtF, the slow component should not come from direct QD emission.[133,146,151] However, the increased intensity at higher QD% and lower FBtF% also suggest that the slow component originates from the addition of QD. It is therefore assumed that the slow decay might be related with some nonlinear processes of QD. Effects such as triplet-triplet annihilation and delayed fluorescence had been reported on plastic scintillators with high primary dye loadings, which might also be applied to this case since QDs could also be viewed as a primary dye.[1,2,149] More research is underway to address the slow emission, which might find potential applications in γ/neutron pulse-shape discrimination.

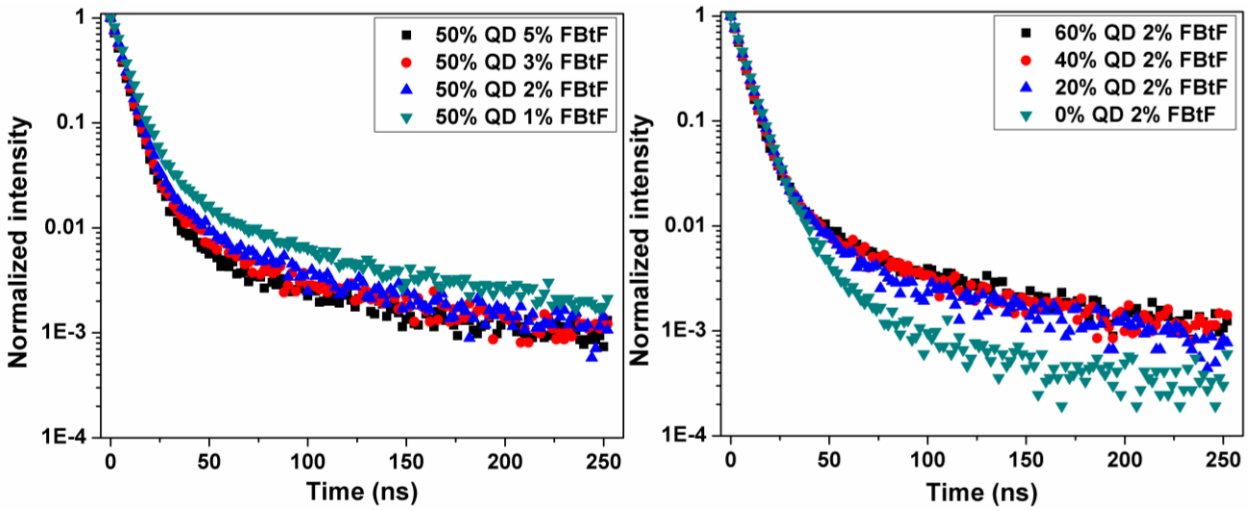

Figure 4.18 Radioluminescence decay curves of (**left**) 50% QD/1-5% FBtF/PVT nanocomposite monoliths and (**right**) 0-60% QD/2% FBtF/PVT nanocomposite monoliths.

Table 4.1 Fitted decay lifetimes and slow component fraction for 50% QD/1-5% FBtF/PVT and 0-60% QD/2% FBtF/PVT nanocomposite scintillators.

	τ_{fast} /ns	τ_{slow} /ns	f_{slow}
50% QD 1% FBtF	7.79	92.21	19.1%
50% QD 2% FBtF	6.66	77.78	13.8%
50% QD 3% FBtF	6.28	71.91	11.9%
50% QD 5% FBtF	5.96	59.44	10.7%
0% QD 2% FBtF	7.47	97.59*	6.3%*
20% QD 2% FBtF	7.08	81.09	9.8%
40% QD 2% FBtF	6.64	72.88	12.3%
60% QD 2% FBtF	6.49	78.32	13.4%

* Slow component cannot be well fitted due to low signal level.

4.3.6 Comparison between 400-nm- and 425-nm-emitting CZS QDs for nanocomposite scintillators

Besides the 425 nm CZS QDs, 400 nm CZS QDs were also synthesized in preliminary tests, with the hope to shift nanocomposite scintillator emission into the blue region with blue-emitting dyes. 400 nm CZS QDs could be easily obtained by only changing the initial injection of 2 mmol S in 3

mL ODE to 3 mmol S in 4.5 mL ODE. PLQYs of the pristine and 1/3-BMEP-modified 400 nm CZS QDs were obtained as 73.7% and 61.5%, respectively. The much lower PLQYs of 400 nm CZS QD is in good agreement with previous reports.[56] Scintillators fabricated using the 400 nm QD and a blue emitting dye, ADS086BE (absorption maximum at 397 nm) from American Dye Source, exhibited green-blue emission. However, LY of the nanocomposite scintillators are constantly lower than the control samples with no QDs. In order to find the reason for this inferior LY, a set of 50 wt% QD/2% FBtF/PVT nanocomposite scintillators were fabricated using both 400 nm QDs and 425 nm QDs, with their performance compared to a blank control sample. **Figure 4.19** shows the emission spectra of 400 nm QD and 425 nm QD in addition to the absorbance spectrum of FBtF. Compared to the 425 nm QDs, the 400 nm QDs also have a good spectral overlap with FBtF. However, LY of the 400-nm-QD loaded nanocomposite scintillator was still lower than the control sample, while the 425-nm-QD loaded nanocomposite scintillator had a higher LY than the control sample (**Figure 4.20**). The lower LY of 400-nm-QD loaded nanocomposite could be ascribed to the smaller R_0 of the 400 nm QD, which was only 3.69 nm compared to the 4.02 nm R_0 for 425 nm QD. Although the difference is only 0.33 nm, considering the QDs' radius of 3 nm with considerable organic ligands wrapped around, such difference could already cause a significant drop in FRET efficiency and thus LY. Since shorter-wavelength-emitting QDs typically have smaller Z and PLQYs than longer-wavelength-emitting QDs, future efforts should then be focused on the development of longer-wavelength-emitting-QD-based nanocomposite scintillators with Si photomultiplier as the detector.

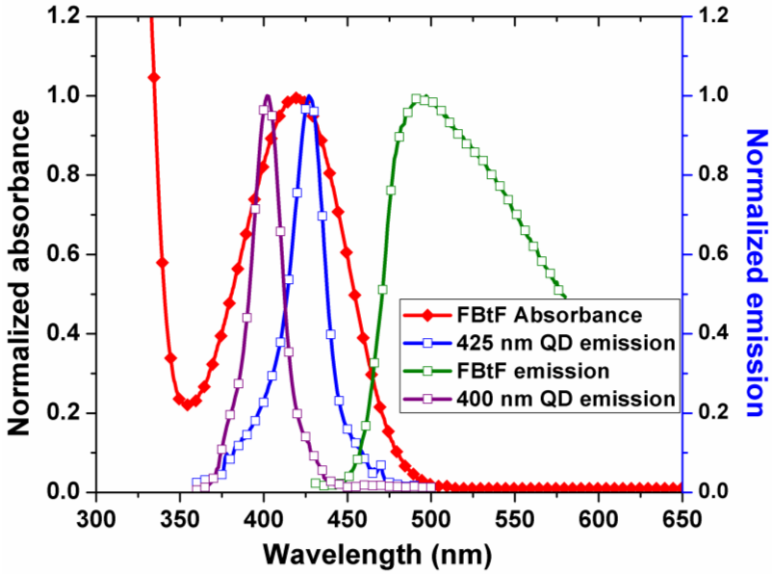

Figure 4.19 Normalized PL spectra of 400-nm- and 425-nm-emitting CZS QDs vs. normalized absorbance and PL spectra of FBtF.

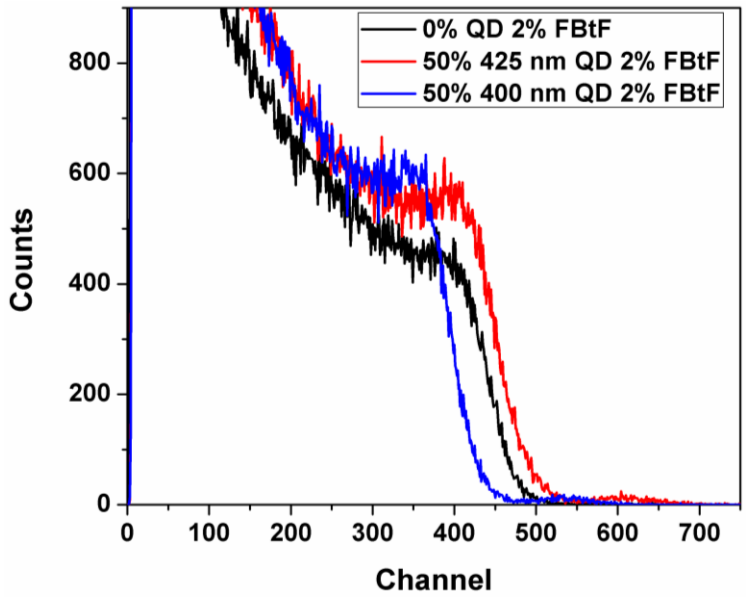

Figure 4.20 Pulse height spectra of 2% FBtF nanocomposite scintillators with no QD, 50% 425-nm-emitting QDs, and 50% 400-nm-emitting QDs.

4.3.7 Additional evidence for the rate-controlling QD-to-FBtF FRET process

As shown before, the QD-to-FBtF FRET is deemed the performance-controlling property for QD-based nanocomposite scintillators under the assumption that the FRET from matrix is efficient, or at least more efficient compared to that from QD to FBtF. In addition to the experimental observation on scintillators with different QDs from section 4.3.6, an additional experiment was carried out to confirm that the QD-to-FBtF FRET rate is smaller than the one from PVT to FBtF. **Figure 4.21** shows the pulse height spectra obtained using QD-free scintillators containing 1-5 wt% of FBtF. The light yield first increases greatly as the FBtF content increases from 1% to 2%, then stays at a similar level with 3% FBtF, and finally decreases significantly when the loading is increased to 5%. This trend in light yield indicates that 1) the PVT-to-FBtF FRET efficiency increases most significantly from 1% to 2% FBtF; 2) the increase in FRET efficiency is almost balanced out by an intensified self-absorption for FBtF loadings between 2% and 3%; and 3) the increase in FRET efficiency is negligible with FBtF loadings higher than 3% and the intensified self-absorption dominates and deteriorates the light yield. Comparing this trend to the one obtained with 50% QD nanocomposite scintillators (**Figure 4.14a**), which shows that the increase in FRET efficiency is constantly balanced by the intensified self-absorption for FBtF loadings between 2% and 5%, and further considering the higher volume percentage of FBtF in QD-loaded scintillators, we can easily reach the conclusion that the PVT-to-FBtF FRET is more efficient compared to that from QD to FBtF. Therefore, the QD-to-FBtF FRET is the rate-controlling process for energy transfer within the nanocomposite, which determines the performance of QD-based nanocomposite scintillators.

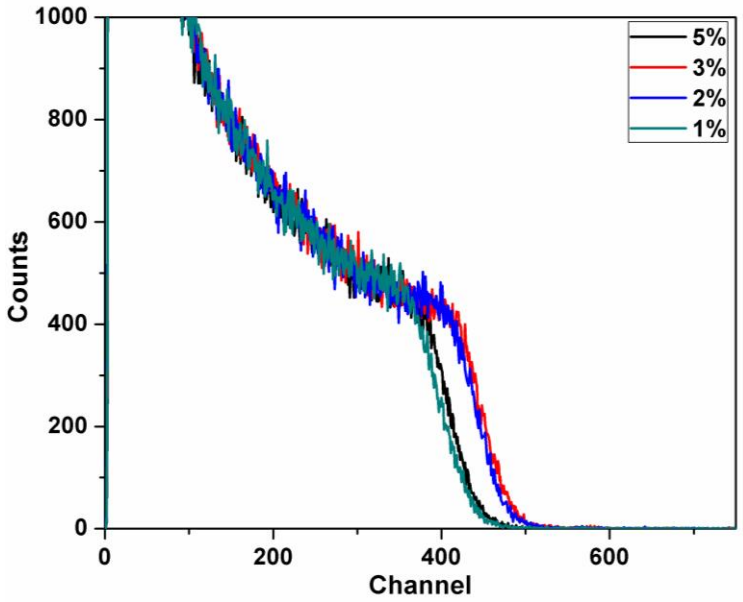

Figure 4.21 Pulse height spectra of QD-free, 1-5% FBtF/PVT nanocomposite monoliths.

4.4 Concluding Remarks

In summary, transparent ultra-high-loading CZS QD/FBtF/PVT nanocomposite scintillators have been successfully synthesized via *in situ* polymerization of the monomer solution containing partial BMEP-modified QDs. By facilitating effective QD-dye FRET, simultaneous enhancements in both Z and LY in a nanocomposite scintillator have been achieved for the first time. The detection of a 662 keV Cs-137 photopeak with 9.8% resolution using a commercial PMT has been demonstrated, highlighting great potential for the development of QD/dye/polymer nanocomposite scintillators for radiation spectroscopy. With the integration of more advanced green/red-sensitive photodetectors such as the Si photomultiplier, a greatly expanded family of QDs with both higher Z and PLQY would become available for building better nanocomposite systems. To ensure high LY in the new system, efficient FRET must be enforced, which can be achieved by using small QDs (radius < 3 nm) with high PLQY (preferably > 80%), in addition to a spectral-matching dye

with high extinction coefficient (> 20000 $M^{-1} \cdot cm^{-1}$). In addition, secondary dyes can also be employed to reduce the self-absorption of primary dye, therefore improving the LY. Future efforts will be focused on elucidating the origin of LY enhancement and slow emission component from QD addition, which could lead to new discoveries and applications in γ/neutron pulse-shape discrimination. In addition to the radiation detection use, the facile fabrication of stable, uniform QD/polymer nanocomposites might also find great potential in other fields such as in solar concentrators and optoelectronic applications.

Chapter 5. Conclusions and perspectives

5.1 Conclusions

The development of scintillators with low cost and high performance has been an important topic due to their wide applications in research, medicine and national securities. As the performance and cost of conventional scintillators are limited by their intrinsic properties and fabrication requirements, the development of nanocomposite scintillators holds great promises as it might combine advantages from both the organics and inorganics. However, the increased complexity of mixing nanomaterials into a polymer matrix brings challenges from both engineering and science aspects, halting the advancing of this nascent field.

This dissertation is dedicated to the development of both new engineering tools and scientific understandings in the field of nanoparticle-based nanocomposite scintillators. In Chapter 2, a high-yield, single-precursor method has been developed for the synthesis of HfO_2 nanoparticles with uniform size distribution and excellent solubility in low-polarity solvent, with the mechanism of this reaction further explored in Chapter 3. With the development of another facile, one-step protocol for partial surface modification with monomer groups, highly transparent, high-loading nanoparticle/polymer nanocomposite monoliths with HfO_2 nanoparticle loadings of up to 40% by weight can now be synthesized in a reproducible manner, which enables the use of this high-Z, large-band-gap, stable oxide material for nanocomposite scintillators. Using the as-developed protocol, blue-emitting nanocomposite scintillators have been synthesized for the first time, and a

2-mm-thick sample comprising up to 20 wt% nanoparticles, 2% PBD and 0.01% POPOP demonstrates the successful detection of a photopeak with 8% resolution for 662 keV Cs-137 γ radiation, representing a great leap over the previous works. In addition, a systematic investigation into the scintillator performance with varied loadings of nanoparticles leads to the discovery of another important factor affecting the scintillator's light yield, the energy trapping effect by non-emissive nanoparticles. It is found that energy trapping has an even greater influence on light yield compared to the transparency of monoliths, which has been confirmed by another work from Chen *et al.* on the YbF_3-loaded highly transparent nanocomposite monoliths.[126]

This discovery of energy trapping necessitates the study into energy extraction for light yield restoration in nanocomposite scintillators. A revisit to the previous concept of QD nanocomposite scintillators is then made in Chapter 4, where the emissive nature of QD is utilized for the extraction of excitons generated. A partial BMEP-modification protocol of QDs is first developed to endow QDs with the capability to be covalently bonded to the growing polymer chain while retaining most of its original solubility and quantum efficiency. The utilization of these partially modified QDs enables the fabrication of transparent QD/PVT nanocomposite monoliths with a record-high QD loading (T_{550nm} = 65.8% for a 60 wt% QD nanocomposite monolith), laying the foundation for its application in nanocomposite scintillator. Building on the transparent QD nanocomposite monolith, a suitable lower-band-gap organic dye, FBtF, is added to facilitate efficient FRET from QD to dye, which both suppresses the self-absorption of QDs and promotes the extraction of QD-borne excitons to dye sites for photon production. As a result, the light yield of QD nanocomposite scintillators has shown an improvement of up to 10% compared to the control sample with no QD. In addition, the efficient QD-to-FBtF FRET also results in a fast

radioluminescence decay in the nanocomposite scintillator, retaining the advantage of plastic scintillators. Aside from the improved light yield, the ultra-high-loading QD/FBtF/PVT scintillator also has a significantly improved Z due to the high loading of quantum dots, which enables the detection of 662 keV gamma photopeak. In the best demonstration, a 60 wt% CZS QD/2% FBtF/PVT nanocomposite scintillator exhibits a light yield of 9255 photons/MeV and a photopeak resolution of 9.8% under 662 keV Cs-137 γ irradiation, highlighting the great potential of this model system for future high-performance low-cost spectroscopic gamma detectors.

5.2 Perspectives

As demonstrated in this dissertation, nanoparticle-based nanocomposite scintillators, with appropriate structure design and engineering, can incorporate the attractive properties from both inorganic and organic scintillators. For the development of next-generation high-Z, high-light-yield, fast-response, and scalable nanocomposite scintillators, the quantum-dot/polymer nanocomposite system seems to be the most promising option, as both Z and light yield can be improved simultaneously with the addition of quantum dots, while the short decay lifetime of plastics can be retained with an efficient QD-dye FRET. For future development based on this model system, the requirements in the material perspective are listed as follows:

A. The emissive nanoparticles need to have:
    a) A high Z element with substantial weight percentage;
    b) A high photoluminescence quantum yield of preferably at least 80%, even after surface modification;
    c) Small sizes with radius < 4 nm;
    d) Good solubility in monomer solution; and

e) Capability of being copolymerized with the monomer solution.

B. The dye needs to have:

a) Good spectral match with the quantum dot's emission, i.e. strong absorption with molar extinction coefficient > 20,000 $M^{-1} \cdot cm^{-1}$;

b) Large Stokes shift; and

c) A high photoluminescent quantum yield of at least 80%.

Satisfaction of these requirements shall ensure the fabrication of a uniform, high-light-yield, high-Z nanocomposite scintillator. A larger ε_A is especially desirable for ensuring an efficient FRET since quantum dots with a PLQY as high as 80% are not always available. In addition, a high-quantum-efficiency secondary dye can also be employed as a wavelength shifter to reduce self-absorption of the primary dye. However, this shall be of less importance compared to the development of nanoparticles and dyes.

The future development of suitable nanoparticles for this application should draw more attention due to its greater difficulty. Other than the traditional II-VI core/shell quantum dots such as CdS/ZnS or CdSe/CdS, an interesting candidate is the recently developed cesium/organo-lead halide perovskite nanoparticles.[45,46] These nanoparticles have a substantial amount of high-Z constituents, high quantum efficiency, and small size, which makes them a great candidate for nanocomposite scintillators. However, their poor solution stability and sensitivities to moisture and pH change make it problematic for the fabrication of nanocomposites, rendering several preliminary attempts fruitless. New chemistries in the surface stabilization and modification of these nanoparticles need to be explored for its successful utilization, whose success may also have a great impact on a much wider array of applications such as LEDs and solar cells.[152–155]

In addition to the development of materials, it is also important to consider the advanced photodetectors with improved sensitivities into the green/red spectral regions, since most quantum dots with higher Z and good quantum yield tend to emit in the long wavelength. The recently developed silicon photomultiplier (SiPM) is an interesting candidate due to its high quantum efficiency in the green-red region (around 40%), high gain, and fast response.[150,156–158] However, there are also issues regarding its use such as the small detector size and thermal fluctuations. New electronics and accessories will need to be designed and fabricated for its integration with the scintillators.

The energy transfer process and photophysics involved in the nanocomposite scintillator are also important topics for future research. There are several questions remaining from the previous chapters, i.e. how does the capability of generating excitons differ from inorganics to organics, and what is the reason behind the rise of slow-decay component with the addition of quantum dots. Both theoretical and experimental efforts are needed to solve these questions, which might bring new insight to the development of nanocomposite scintillators.

Other than radiation detection, the synthetic and nanocomposite fabricating techniques developed in this dissertation may also find applications in other areas. For example, the synthesis and surface modification protocol for HfO_2 can be extended to the fabrication of high-refractive-index coatings as demonstrated in Chapter 3. In addition, provided a suitable surface modification protocol to render them hydrophilic, the stable, high-Z HfO_2 nanoparticles may also be useful as a biocompatible contrast agent in X-ray computed tomography.[159,160] Moreover, the fabrication

technique for QD/polymer nanocomposites may find immediate application in the development of bulk solar concentrators and LCD color converters.[128,140] Similar philosophies of surface and interface engineering may be applied to the design and construction of a wide range of polymer-based nanocomposites for multi-functionalization and property enhancement. A new era of nanocomposites has begun, and with rigorous design and precise engineering, it will shape our future.

References

(1) Knoll, G. F. *Radiation Detection and Measurement*; 4th ed.; John Wiley & Sons: Hoboken, 2010.

(2) Birks, J. B. *The Theory and Practice of Scintillation Counting*; Pergamon: Oxford, England, 1964.

(3) Grupen, C. *Astroparticle Physics*; Springer Science & Business Media, 2005.

(4) Van Eijk, C. W. E. Inorganic Scintillators in Medical Imaging. *Phys. Med. Biol.* **2002**, *47*, R85–R106.

(5) Siciliano, E. R.; Ely, J. H.; Kouzes, R. T.; Milbrath, B. D.; Schweppe, J. E.; Stromswold, D. C. Comparison of PVT and NaI(Tl) Scintillators for Vehicle Portal Monitor Applications. *Nucl. Instrum. Methods Phys. Res., Sect. A* **2005**, *550*, 647–674.

(6) Clough, R. . High-Energy Radiation and Polymers: A Review of Commercial Processes and Emerging Applications. *Nucl. Instrum. Methods Phys. Res., Sect. B* **2001**, *185*, 8–33.

(7) Lindquist, C. Gamma Knife Radiosurgery. *Semin. Radiat. Oncol.* **1995**, *5*, 197–202.

(8) Atwood, W. B.; Abdo, A. A.; Ackermann, M.; Althouse, W.; Anderson, B.; Axelsson, M.; Baldini, L.; Ballet, J.; Band, D. L.; Barbiellini, G.; *et al.* THE LARGE AREA TELESCOPE ON THE FERMI GAMMA-RAY SPACE TELESCOPE MISSION. *Astrophys. J.* **2009**, *697*, 1071–1102.

(9) Milbrath, B. D.; Peurrung, A. J.; Bliss, M.; Weber, W. J. Radiation Detector Materials: An Overview. *J. Mater. Res.* **2011**, *23*, 2561–2581.

(10) Owens, A. Semiconductor Materials and Radiation Detection. *J. Synchrotron Radiat.* **2006**, *13*, 143–150.

(11) Lee, C.-D.; Hartnett, T.; Tustison, R. Development of Radiation Detection Materials. In *Proc. SPIE*; 2012; Vol. 8373, p. 83730X.

(12) Blasse, G. Scintillator Materials. *Chem. Mater.* **1994**, *6*, 1465–1475.

(13) Hofstadter, R. Alkali Halide Scintillation Counters. *Phys. Rev.* **1948**, *74*, 100–101.

(14) Moses, W. W. Current Trends in Scintillator Detectors and Materials. *Nucl. Instrum. Methods Phys. Res., Sect. A* **2002**, *487*, 123–128.

(15) Yakunin, S.; Sytnyk, M.; Kriegner, D.; Shrestha, S.; Richter, M.; Matt, G. J.; Azimi, H.; Brabec, C. J.; Stangl, J.; Kovalenko, M. V; *et al.* Detection of X-Ray Photons by Solution-Processed Lead Halide Perovskites. *Nat. Photonics* **2015**, *9*, 444–449.

(16) Yakunin, S.; Dirin, D. N.; Shynkarenko, Y.; Morad, V.; Cherniukh, I.; Nazarenko, O.; Kreil, D.; Nauser, T.; Kovalenko, M. V. Detection of Gamma Photons Using Solution-Grown Single Crystals of Hybrid Lead Halide Perovskites. *Nat. Photonics* **2016**, *10*, 585–589.

(17) Derenzo, S. E.; Moses, W. W.; Cahoon, J. L.; Perera, R. C. C.; Litton, J. E. Prospects for New Inorganic Scintillators. *IEEE Trans. Nucl. Sci.* **1990**, *37*, 203–208.

(18) Cherepy, N. J.; Payne, S. A.; Asztalos, S. J.; Hull, G.; Kuntz, J. D.; Niedermayr, T.; Pimputkar, S.; Roberts, J. J.; Sanner, R. D.; Tillotson, T. M.; *et al.* Scintillators With Potential to Supersede Lanthanum Bromide. *IEEE Trans. Nucl. Sci.* **2009**, *56*, 873–880.

(19) van Loef, E. V. D.; Dorenbos, P.; van Eijk, C. W. E.; Krämer, K.; Güdel, H. U. High-Energy-Resolution Scintillator: Ce3+ Activated LaBr3. *Appl. Phys. Lett.* **2001**, *79*, 1573–1575.

(20) Setyawan, W.; Gaume, R. M.; Feigelson, R. S.; Curtarolo, S. Comparative Study of

Nonproportionality and Electronic Band Structures Features in Scintillator Materials. *IEEE Trans. Nucl. Sci.* **2009**, *56*, 2989–2996.

(21) van Loef, E. V. D.; Dorenbos, P.; van Eijk, C. W. E.; Krämer, K. W.; Güdel, H. U. Optical and Scintillation Properties of Pure and Ce3+ Doped GdBr3. *Opt. Commun.* **2001**, *189*, 297–304.

(22) Glodo, J.; Higgins, W. M.; van Loef, E. V. D.; Shah, K. S. GdI3:Ce - A New Gamma and Neutron Scintillator. In *2006 IEEE Nuclear Science Symposium Conference Record*; IEEE, 2006; pp. 1574–1577.

(23) Cherepy, N. J.; Seeley, Z. M.; Payne, S. A.; Beck, P. R.; Swanberg, E. L.; Hunter, S.; Ahle, L.; Fisher, S. E.; Melcher, C.; Wei, H.; *et al.* High Energy Resolution with Transparent Ceramic Garnet Scintillators. In *Proceedings of SPIE*; 2014; Vol. 9213, p. 921302.

(24) Zaitseva, N.; Rupert, B. L.; PaweŁczak, I.; Glenn, A.; Martinez, H. P.; Carman, L.; Faust, M.; Cherepy, N.; Payne, S. Plastic Scintillators with Efficient Neutron/gamma Pulse Shape Discrimination. *Nucl. Instrum. Methods Phys. Res., Sect. A* **2012**, *668*, 88–93.

(25) Salimgareeva, V. N.; Kolesov, S. V. Plastic Scintillators Based on Polymethyl Methacrylate: A Review. *Instruments Exp. Tech.* **2005**, *48*, 273–282.

(26) Lakowicz, J. R. *Principles of Fluorescence Spectroscopy, 3rd Edition, Joseph R. Lakowicz, Editor*; 2006.

(27) Förster-Resonance-Energy Transfer FRET. In *IUPAC Compendium of Chemical Terminology*; 2014; pp. 1–3.

(28) *Highly Efficient OLEDs with Phosphorescent Materials*; Yersin, H., Ed.; Wiley-VCH Verlag GmbH & Co. KGaA: Weinheim, Germany, 2007.

(29) Basile, L. J. Characteristics of Plastic Scintillators. *J. Chem. Phys.* **1957**, *27*, 801–806.

(30) Pawełczak, I. A.; Glenn, A. M.; Martinez, H. P.; Carman, M. L.; Zaitseva, N. P.; Payne, S. A. Boron-Loaded Plastic Scintillator with Neutron-γ Pulse Shape Discrimination Capability. *Nucl. Instrum. Methods Phys. Res., Sect. A* **2014**, *751*, 62–69.

(31) Hyman, M.; Ryan, J. J. Heavy Elements in Plastic Scintillators. *IRE Trans. Nucl. Sci.* **1958**, *5*, 87–90.

(32) Pichat, L.; Pesteil, P.; Clement, J. Solides Fluorescents Non Cristallans Pour Mesures de Radioactivite. *J. Chim. Phys. PHYSICO-CHIMIE Biol.* **1953**, *50*, 26–41.

(33) Sandler, S. R.; Tsou, K. C. Quenching of the Scintillation Process in Plastics by Organometallics 1. *J. Phys. Chem.* **1964**, *68*, 300–304.

(34) Tsou, K. C. Evaluation of Organometallic Compounds for Gamma Detection in Plastic Scintillators. *IEEE Trans. Nucl. Sci.* **1965**, *12*, 28–33.

(35) Adachi, C.; Baldo, M. A.; Thompson, M. E.; Forrest, S. R. Nearly 100% Internal Phosphorescence Efficiency in an Organic Light-Emitting Device. *J. Appl. Phys.* **2001**, *90*, 5048–5051.

(36) D'Andrade, B. W.; Forrest, S. R. White Organic Light-Emitting Devices for Solid-State Lighting. *Adv. Mater.* **2004**, *16*, 1585–1595.

(37) Forrest, S. R. The Road to High Efficiency Organic Light Emitting Devices. *Org. Electron.* **2003**, *4*, 45–48.

(38) Rupert, B. L.; Cherepy, N. J.; Sturm, B. W.; Sanner, R. D.; Payne, S. A. Bismuth-Loaded Plastic Scintillators for Gamma-Ray Spectroscopy. *Europhys. Lett.* **2012**, *97*, 22002.

(39) Feng, P. L.; Mengesha, W.; Anstey, M. R.; Cordaro, J. G. Distance Dependent Quenching and Gamma-Ray Spectroscopy in Tin-Loaded Polystyrene Scintillators. *IEEE Trans. Nucl. Sci.* **2016**, *63*, 407–415.

(40) van Loef, E. V.; Feng, P.; Markosyan, G.; Shirwadkar, U.; Doty, P.; Shah, K. S. High Energy Resolution Plastic Scintillator. In *Proc. SPIE*; 2016; Vol. 63, p. 996803.

(41) van Loef, E.; Markosyan, G.; Shirwadkar, U.; McClish, M.; Shah, K. Gamma-Ray Spectroscopy and Pulse Shape Discrimination with a Plastic Scintillator. *Nucl. Instrum. Methods Phys. Res., Sect. A* **2015**, *788*, 71–72.

(42) Vistovskyy, V. V.; Zhyshkovych, A. V.; Halyatkin, O. O.; Mitina, N. E.; Zaichenko, A. S.; Rodnyi, P. A.; Vasil'ev, A. N.; Gektin, A. V.; Voloshinovskii, A. S. The Luminescence of BaF2 Nanoparticles upon High-Energy Excitation. *J. Appl. Phys.* **2014**, *116*, 54308.

(43) Lauria, A.; Villa, I.; Fasoli, M.; Niederberger, M.; Vedda, A. Multifunctional Role of Rare Earth Doping in Optical Materials: Nonaqueous Sol-Gel Synthesis of Stabilized Cubic HfO2 Luminescent Nanoparticles. *ACS Nano* **2013**, *7*, 7041–7052.

(44) Ye, X.; Collins, J. E.; Kang, Y.; Chen, J.; Chen, D. T. N.; Yodh, A. G.; Murray, C. B. Morphologically Controlled Synthesis of Colloidal Upconversion Nanophosphors and Their Shape-Directed Self-Assembly. *Proc. Natl. Acad. Sci. U. S. A.* **2010**, *107*, 22430–22435.

(45) Protesescu, L.; Yakunin, S.; Bodnarchuk, M. I.; Krieg, F.; Caputo, R.; Hendon, C. H.; Yang, R. X.; Walsh, A.; Kovalenko, M. V. Nanocrystals of Cesium Lead Halide Perovskites (CsPbX 3 , X = Cl, Br, and I): Novel Optoelectronic Materials Showing Bright Emission with Wide Color Gamut. *Nano Lett.* **2015**, *15*, 3692–3696.

(46) Protesescu, L.; Yakunin, S.; Bodnarchuk, M. I.; Bertolotti, F.; Masciocchi, N.; Guagliardi, A.; Kovalenko, M. V. Monodisperse Formamidinium Lead Bromide Nanocrystals with Bright and Stable Green Photoluminescence. *J. Am. Chem. Soc.* **2016**, *138*, 14202–14205.

(47) Mai, H.; Zhang, Y.; Si, R.; Yan, Z.-G.; Sun, L.; You, L.; Yan, C. High-Quality Sodium

Rare-Earth Fluoride Nanocrystals: Controlled Synthesis and Optical Properties. *J. Am. Chem. Soc.* **2006**, *128*, 6426–6436.

(48) Zhang, Y.; Sun, X.; Si, R.; You, L.; Yan, C. Single-Crystalline and Monodisperse LaF3 Triangular Nanoplates from a Single-Source Precursor. *J. Am. Chem. Soc.* **2005**, *127*, 3260–3261.

(49) Wang, X.; Zhuang, J.; Peng, Q.; Li, Y. A General Strategy for Nanocrystal Synthesis. *Nature* **2005**, *437*, 121–124.

(50) Murray, C. B.; Kagan, C. R.; Bawendi, M. G. Synthesis and Characterization of Monodisperse Nanocrystals and Close-Packed Nanocrystal Assemblies. *Annu. Rev. Mater. Sci.* **2000**, *30*, 545–610.

(51) O'Brien, S.; Brus, L.; Murray, C. B. Synthesis of Monodisperse Nanoparticles of Barium Titanate: Toward a Generalized Strategy of Oxide Nanoparticle Synthesis. *J. Am. Chem. Soc.* **2001**, *123*, 12085–12086.

(52) Murray, C. B.; Norris, D. J.; Bawendi, M. G. Synthesis and Characterization of Nearly Monodisperse CdE (E = Sulfur, Selenium, Tellurium) Semiconductor Nanocrystallites. *J. Am. Chem. Soc.* **1993**, *115*, 8706–8715.

(53) Tang, J.; Fabbri, J.; Robinson, R. D.; Zhu, Y.; Herman, I. P.; Steigerwald, M. L.; Brus, L. E. Solid-Solution Nanoparticles: Use of a Nonhydrolytic Sol−Gel Synthesis To Prepare HfO2 and HfxZr1- xO2 Nanocrystals. *Chem. Mater.* **2004**, *16*, 1336–1342.

(54) Peng, X.; Schlamp, M. C.; Kadavanich, A. V.; Alivisatos, A. P. Epitaxial Growth of Highly Luminescent CdSe/CdS Core/Shell Nanocrystals with Photostability and Electronic Accessibility. *J. Am. Chem. Soc.* **1997**, *119*, 7019–7029.

(55) Peng, Z. A.; Peng, X. Formation of High-Quality CdTe, CdSe, and CdS Nanocrystals Using

CdO as Precursor. *J. Am. Chem. Soc.* **2001**, *123*, 183–184.

(56) Bae, W. K.; Nam, M. K.; Char, K.; Lee, S. Gram-Scale One-Pot Synthesis of Highly Luminescent Blue Emitting Cd1− X Znx S/ZnS Nanocrystals. *Chem. Mater.* **2008**, *20*, 5307–5313.

(57) Wang, F.; Liu, X. Recent Advances in the Chemistry of Lanthanide-Doped Upconversion Nanocrystals. *Chem. Soc. Rev.* **2009**, *38*, 976–989.

(58) Balazs, A. C.; Emrick, T.; Russell, T. P. Nanoparticle Polymer Composites: Where Two Small Worlds Meet. *Science* **2006**, *314*, 1107–1110.

(59) Young, R. J.; Lovell, P. A. *Introduction to Polymers*; 3rd ed.; CRC press: Boca Raton, 2011.

(60) Vasil'chenko, V. G.; Solov'Ev, A. S. Properties of Composite Scintillators in Static and Dynamic States. *Instruments Exp. Tech.* **2003**, *46*, 758–764.

(61) Campbell, I. H.; Crone, B. K. Quantum-Dot/Organic Semiconductor Composites for Radiation Detection. *Adv. Mater.* **2006**, *18*, 77–79.

(62) Létant, S. E.; Wang, T.-F. Semiconductor Quantum Dot Scintillation under Gamma-Ray Irradiation. *Nano Lett.* **2006**, *6*, 2877–2880.

(63) Kang, Z.; Zhang, Y.; Menkara, H.; Wagner, B. K.; Summers, C. J.; Lawrence, W.; Nagarkar, V. CdTe Quantum Dots and Polymer Nanocomposites for X-Ray Scintillation and Imaging. *Appl. Phys. Lett.* **2011**, *98*, 181914.

(64) Lawrence, W. G.; Thacker, S.; Palamakumbura, S.; Riley, K. J.; Nagarkar, V. V. Quantum Dot-Organic Polymer Composite Materials for Radiation Detection and Imaging. *IEEE Trans. Nucl. Sci.* **2012**, *59*, 215–221.

(65) McKigney, E. A.; Del Sesto, R. E.; Jacobsohn, L. G.; Santi, P. A.; Muenchausen, R. E.; Ott, K. C.; McCleskey, T. M.; Bennett, B. L.; Smith, J. F.; Cooke, D. W. Nanocomposite

Scintillators for Radiation Detection and Nuclear Spectroscopy. *Nucl. Instrum. Methods Phys. Res., Sect. A* **2007**, *579*, 15–18.

(66) Feller, R. K.; Purdy, G. M.; Ortiz-Acosta, D.; Stange, S.; Li, A.; McKigney, E. A.; Esch, E. I.; Muenchausen, R. E.; Gilbertson, R.; Bacrania, M.; *et al.* Large-Scale Synthesis of CexLa1−xF3 Nanocomposite Scintillator Materials. *J. Mater. Chem.* **2011**, *21*, 5716.

(67) Kang, Z.; Barta, M.; Nadler, J.; Wagner, B.; Rosson, R.; Kahn, B. Synthesis of BaF2:Ce Nanophosphor and Epoxy Encapsulated Transparent Nanocomposite. *J. Lumin.* **2011**, *131*, 2140–2143.

(68) Dujardin, C.; Amans, D.; Belsky, A.; Chaput, F.; Ledoux, G.; Pillonnet, A. Luminescence and Scintillation Properties at the Nanoscale. *IEEE Trans. Nucl. Sci.* **2010**, *57*, 1348–1354.

(69) LeLuyer, C.; Villanueva-Ibañez, M.; Pillonnet, A.; Dujardin, C. HfO 2 :X (X = Eu 3+ , Ce 3+ , Y 3+) Sol Gel Powders for Ultradense Scintillating Materials. *J. Phys. Chem. A* **2008**, *112*, 10152–10155.

(70) Jalabadze, N. V.; Chedia, R.; Kukava, T.; Nadaraia, L. Development of New Technologies for the Manufacturing of Nanocrystalline Scintillation Materials. *IEEE Trans. Nucl. Sci.* **2008**, *55*, 1514–1522.

(71) Cai, W.; Chen, Q.; Cherepy, N.; Dooraghi, A.; Kishpaugh, D.; Chatziioannou, A.; Payne, S.; Xiang, W.; Pei, Q. Synthesis of Bulk-Size Transparent Gadolinium Oxide–polymer Nanocomposites for Gamma Ray Spectroscopy. *J. Mater. Chem. C* **2013**, *1*, 1970.

(72) Aricò, A. S.; Bruce, P.; Scrosati, B.; Tarascon, J.; Van Schalkwijk, W. Nanostructured Materials for Advanced Energy Conversion and Storage Devices. *Nat. Mater.* **2005**, *4*, 366–377.

(73) Yu, Z.; Li, L.; Zhang, Q.; Hu, W.; Pei, Q. Silver Nanowire-Polymer Composite Electrodes

for Efficient Polymer Solar Cells. *Adv. Mater.* **2011**, *23*, 4453–4457.

(74) Koerner, H.; Price, G.; Pearce, N. A.; Alexander, M.; Vaia, R. A. Remotely Actuated Polymer Nanocomposites--Stress-Recovery of Carbon-Nanotube-Filled Thermoplastic Elastomers. *Nat. Mater.* **2004**, *3*, 115–120.

(75) Hu, W.; Zhang, S. N.; Niu, X.; Liu, C.; Pei, Q. An Aluminum Nanoparticle–acrylate Copolymer Nanocomposite as a Dielectric Elastomer with a High Dielectric Constant. *J. Mater. Chem. C* **2014**, *2*, 1658.

(76) Stankovich, S.; Dikin, D. A.; Dommett, G. H. B.; Kohlhaas, K. M.; Zimney, E. J.; Stach, E. A.; Piner, R. D.; Nguyen, S. T.; Ruoff, R. S. Graphene-Based Composite Materials. *Nature* **2006**, *442*, 282–286.

(77) Liang, J.; Li, L.; Tong, K.; Ren, Z.; Hu, W.; Niu, X.; Chen, Y.; Pei, Q. Silver Nanowire Percolation Network Soldered with Graphene Oxide at Room Temperature and Its Application for Fully Stretchable Polymer Light-Emitting Diodes. *ACS Nano* **2014**, *8*, 1590–1600.

(78) Novak, B. M. Hybrid Nanocomposite Materials Between Inorganic Glasses and Organic Polymers. *Adv. Mater.* **1993**, *5*, 422–433.

(79) Li, Y.; Tao, P.; Viswanath, A.; Benicewicz, B. C.; Schadler, L. S. Bimodal Surface Ligand Engineering: The Key to Tunable Nanocomposites. *Langmuir* **2013**, *29*, 1211–1220.

(80) Lee, S.; Shin, H.-J.; Yoon, S.-M.; Yi, D. K.; Choi, J.-Y.; Paik, U. Refractive Index Engineering of Transparent ZrO2–polydimethylsiloxane Nanocomposites. *J. Mater. Chem.* **2008**, *18*, 1751.

(81) Lü, C.; Yang, B. High Refractive Index Organic–inorganic Nanocomposites: Design, Synthesis and Application. *J. Mater. Chem.* **2009**, *19*, 2884.

(82) Wilk, G. D.; Wallace, R. M.; Anthony, J. M. High-κ Gate Dielectrics: Current Status and Materials Properties Considerations. *J. Appl. Phys.* **2001**, *89*, 5243.

(83) Bersch, E.; Rangan, S.; Bartynski, R.; Garfunkel, E.; Vescovo, E. Band Offsets of Ultrathin High-κ Oxide Films with Si. *Phys. Rev. B* **2008**, *78*, 85114.

(84) Callegari, A.; Cartier, E.; Gribelyuk, M.; Okorn-Schmidt, H. F.; Zabel, T. Physical and Electrical Characterization of Hafnium Oxide and Hafnium Silicate Sputtered Films. *J. Appl. Phys.* **2001**, *90*, 6466.

(85) Armelao, L.; Eisenmenger-Sittner, C.; Groenewolt, M.; Gross, S.; Sada, C.; Schubert, U.; Tondello, E.; Zattin, A. Zirconium and Hafnium Oxoclusters as Molecular Building Blocks for Highly Dispersed ZrO2 or HfO2 Nanoparticles in Silica Thin Films. *J. Mater. Chem.* **2005**, *15*, 1838.

(86) Armelao, L.; Bertagnolli, H.; Bleiner, D.; Groenewolt, M.; Gross, S.; Krishnan, V.; Sada, C.; Schubert, U.; Tondello, E.; Zattin, A. Highly Dispersed Mixed Zirconia and Hafnia Nanoparticles in a Silica Matrix: First Example of a ZrO2-HfO2-SiO2 Ternary Oxide System. *Adv. Funct. Mater.* **2007**, *17*, 1671–1681.

(87) Pinna, N.; Garnweitner, G.; Antonietti, M.; Niederberger, M. Non-Aqueous Synthesis of High-Purity Metal Oxide Nanopowders Using an Ether Elimination Process. *Adv. Mater.* **2004**, *16*, 2196–2200.

(88) Buha, J.; Arčon, D.; Niederberger, M.; Djerdj, I. Solvothermal and Surfactant-Free Synthesis of Crystalline Nb(2)O(5), Ta(2)O(5), HfO(2), and Co-Doped HfO(2) Nanoparticles. *Phys. Chem. Chem. Phys.* **2010**, *12*, 15537–15543.

(89) Tirosh, E.; Markovich, G. Control of Defects and Magnetic Properties in Colloidal HfO2 Nanorods. *Adv. Mater.* **2007**, *19*, 2608–2612.

(90) Britvich, G.; Peresypkin, A.; Rykalin, V. I.; Vasil'chenko, V. G.; Kornylovskaya, L. D.; Malinovskaya, S. A.; Skripkina, V. T.; Shershukov, V. M.; Yushko, E. G.; Kulichenko, A. V.; *et al.* Radiation Damage Studies on Polystyrene-Based Scintillators. *Nucl. Instrum. Methods Phys. Res., Sect. A* **1993**, *326*, 483–488.

(91) Sartori, P.; Weidenbruch, M. Reactions of Halides of Group IV Elements with Trifluoroacetic Acid. *Angew. Chem. Int. Ed.* **1964**, *3*, 376–377.

(92) Nielsen, R. H. Hafnium and Hafnium Compounds. *Kirk-Othmer Encyclopedia of Chemical Technology*, 2000, *4*, 1–19.

(93) Stables, C. M.; Sutcliffe, H. Carboxylato Complexes of zirconium(IV) I: Trifluoroacetato Complexes. *J. Less Common Met.* **1986**, *124*, 185–191.

(94) Mourdikoudis, S.; Liz-Marzán, L. M. Oleylamine in Nanoparticle Synthesis. *Chem. Mater.* **2013**, *25*, 1465–1476.

(95) Schöttle, C.; Bockstaller, P.; Gerthsen, D.; Feldmann, C. Tungsten Nanoparticles from Liquid-Ammonia-Based Synthesis. *Chem. Commun.* **2014**, *50*, 4547–4550.

(96) Bulin, A.-L.; Vasil'ev, A.; Belsky, A.; Amans, D.; Ledoux, G.; Dujardin, C. Modelling Energy Deposition in Nanoscintillators to Predict the Efficiency of the X-Ray-Induced Photodynamic Effect. *Nanoscale* **2015**, *7*, 5744–5751.

(97) O'Regan, B.; Grätzel, M. A Low-Cost, High-Efficiency Solar Cell Based on Dye-Sensitized Colloidal TiO2 Films. *Nature* **1991**, *353*, 737–740.

(98) Klimov, V. I.; Mikhailovsky, A. A.; Xu, S.; Malko, A.; Hollingsworth, J. A.; Leatherdale, C. A.; Eisler, H.-J.; Bawendi, M. G. Optical Gain and Stimulated Emission in Nanocrystal Quantum Dots. *Science* **2000**, *290*, 314–317.

(99) Laurent, S.; Forge, D.; Port, M.; Roch, A.; Robic, C.; Vander Elst, L.; Muller, R. N.

Magnetic Iron Oxide Nanoparticles: Synthesis, Stabilization, Vectorization, Physicochemical Characterizations and Biological Applications. *Chem. Rev.* **2008**, *108*, 2064–2110.

(100) Medintz, I. L.; Uyeda, H. T.; Goldman, E. R.; Mattoussi, H. Quantum Dot Bioconjugates for Imaging, Labelling and Sensing. *Nat. Mater.* **2005**, *4*, 435–446.

(101) Sun, S.; Zeng, H. Size-Controlled Synthesis of Magnetite Nanoparticles. *J. Am. Chem. Soc.* **2002**, *124*, 8204–8205.

(102) Park, J.; Joo, J.; Soon, G. K.; Jang, Y.; Hyeon, T. Synthesis of Monodisperse Spherical Nanocrystals. *Angew. Chem. Int. Ed.* **2007**, *46*, 4630–4660.

(103) Liu, C.; Hajagos, T. J.; Kishpaugh, D.; Jin, Y.; Hu, W.; Chen, Q.; Pei, Q. Facile Single-Precursor Synthesis and Surface Modification of Hafnium Oxide Nanoparticles for Nanocomposite γ-Ray Scintillators. *Adv. Funct. Mater.* **2015**, *25*, 4607–4616.

(104) Daniel, M. C.; Astruc, D. Gold Nanoparticles: Assembly, Supramolecular Chemistry, Quantum-Size-Related Properties, and Applications Toward Biology, Catalysis, and Nanotechnology. *Chem. Rev.* **2004**, *104*, 293–346.

(105) Comotti, M.; Li, W.-C.; Spliethoff, B.; Schüth, F. Support Effect in High Activity Gold Catalysts for CO Oxidation. *J. Am. Chem. Soc.* **2006**, *128*, 917–924.

(106) McDonald, S. A.; Konstantatos, G.; Zhang, S.; Cyr, P. W.; Klem, E. J. D.; Levina, L.; Sargent, E. H. Solution-Processed PbS Quantum Dot Infrared Photodetectors and Photovoltaics. *Nat. Mater.* **2005**, *4*, 138–142.

(107) Atwater, H. A.; Polman, A. Plasmonics for Improved Photovoltaic Devices. *Nat. Mater.* **2010**, *9*, 205–213.

(108) Schroeder, R.; Majewski, L. A.; Grell, M. High-Performance Organic Transistors Using

Solution-Processed Nanoparticle-Filled High-K Polymer Gate Insulators. *Adv. Mater.* **2005**, *17*, 1535–1539.

(109) Joo, J.; Yu, T.; Kim, Y. W.; Park, H. M.; Wu, F.; Zhang, J. Z.; Hyeon, T. Multigram Scale Synthesis and Characterization of Monodisperse Tetragonal Zirconia Nanocrystals. *J. Am. Chem. Soc.* **2003**, *125*, 6553–6557.

(110) Garnweitner, G.; Goldenberg, L. M.; Sakhno, O. V.; Antonietti, M.; Niederberger, M.; Stumpe, J. Large-Scale Synthesis of Organophilic Zirconia Nanoparticles and Their Application in Organic-Inorganic Nanocomposites for Efficient Volume Holography. *Small* **2007**, *3*, 1626–1632.

(111) Lee, S.; Cho, I.-S.; Lee, J. H.; Kim, D. H.; Kim, D. W.; Kim, J. Y.; Shin, H.; Lee, J.-K.; Jung, H. S.; Park, N.-G.; *et al.* Two-Step Sol−Gel Method-Based TiO 2 Nanoparticles with Uniform Morphology and Size for Efficient Photo-Energy Conversion Devices. *Chem. Mater.* **2010**, *22*, 1958–1965.

(112) Si, R.; Zhang, Y.; Zhou, H.; Sun, L.; Yan, C. Controlled-Synthesis, Self-Assembly Behavior, and Surface-Dependent Optical Properties of High-Quality Rare-Earth Oxide Nanocrystals. *Chem. Mater.* **2007**, *19*, 18–27.

(113) Tao, P.; Li, Y.; Rungta, A.; Viswanath, A.; Gao, J.; Benicewicz, B. C.; Siegel, R. W.; Schadler, L. S. TiO2 Nanocomposites with High Refractive Index and Transparency. *J. Mater. Chem.* **2011**, *21*, 18623.

(114) Cozzoli, P. D.; Kornowski, A.; Weller, H. Low-Temperature Synthesis of Soluble and Processable Organic-Capped Anatase TiO2 Nanorods. *J. Am. Chem. Soc.* **2003**, *125*, 14539–14548.

(115) Zhao, N.; Pan, D.; Nie, W.; Ji, X. Two-Phase Synthesis of Shape-Controlled Colloidal

Zirconia Nanocrystals and Their Characterization. *J. Am. Chem. Soc.* **2006**, *128*, 10118–10124.

(116) Zhang, Z.; Zhong, X.; Liu, S.; Li, D.; Han, M. Aminolysis Route to Monodisperse Titania Nanorods with Tunable Aspect Ratio. *Angew. Chem.* **2005**, *117*, 3532–3536.

(117) Zhang, X.; Wang, H.; Xu, B. Q. Remarkable Nanosize Effect of Zirconia in Au/ZrO2 Catalyst for CO Oxidation. *J. Phys. Chem. B* **2005**, *109*, 9678–9683.

(118) Gehr, R. J.; Boyd, R. W. Optical Properties of Nanostructured Optical Materials. *Chem. Mater.* **1996**, *8*, 1807–1819.

(119) Rüssel, C. A Pyrolytic Route to Fluoride Glasses. I. Preparation and Thermal Decomposition of Metal Trifluoroacetates. *J. Non. Cryst. Solids* **1993**, *152*, 161–166.

(120) Hench, L. L.; West, J. K. The Sol-Gel Process. *Chem. Rev.* **1990**, *90*, 33–72.

(121) Tao, P.; Li, Y.; Siegel, R. W.; Schadler, L. S. Transparent Dispensible High-Refractive Index ZrO2/epoxy Nanocomposites for LED Encapsulation. *J. Appl. Polym. Sci.* **2013**, *130*, 3785–3793.

(122) Rao, Y.; Chen, S. Molecular Composites Comprising TiO 2 and Their Optical Properties. *Macromolecules* **2008**, *41*, 4838–4844.

(123) Imai, Y.; Terahara, A.; Hakuta, Y.; Matsui, K.; Hayashi, H.; Ueno, N. Transparent Poly(bisphenol A Carbonate)-Based Nanocomposites with High Refractive Index Nanoparticles. *Eur. Polym. J.* **2009**, *45*, 630–638.

(124) Cherepy, N. J.; Sanner, R. D.; Beck, P. R.; Swanberg, E. L.; Tillotson, T. M.; Payne, S. A.; Hurlbut, C. R. Bismuth- and Lithium-Loaded Plastic Scintillators for Gamma and Neutron Detection. *Nucl. Instrum. Methods Phys. Res., Sect. A* **2015**, *778*, 126–132.

(125) Jin, Y.; Kishpaugh, D.; Liu, C.; Hajagos, T. J.; Chen, Q.; Li, L.; Chen, Y.; Pei, Q. Partial

Ligand Exchange as a Critical Approach to the Synthesis of Transparent Ytterbium Fluoride–polymer Nanocomposite Monoliths for Gamma Ray Scintillation. *J. Mater. Chem. C* **2016**, *4*, 3654–3660.

(126) Chen, Y.; Liu, C.; Jin, Y.; Hajagos, T. J.; Kishpaugh, D.; Zhuang, Q.; Pei, Q. Ytterbium Fluoride Loaded Plastic Scintillators for γ-Ray Spectroscopy. In *Proc. SPIE 9968, Hard X-Ray, Gamma-Ray, and Neutron Detector Physics XVIII*; 2016; p. 99680N.

(127) Dai, X.; Zhang, Z.; Jin, Y.; Niu, Y.; Cao, H.; Liang, X.; Chen, L.; Wang, J.; Peng, X. Solution-Processed, High-Performance Light-Emitting Diodes Based on Quantum Dots. *Nature* **2014**, *515*, 96–99.

(128) Shirasaki, Y.; Supran, G. J.; Bawendi, M. G.; Bulović, V. Emergence of Colloidal Quantum-Dot Light-Emitting Technologies. *Nat. Photonics* **2012**, *7*, 13–23.

(129) Yang, Y.; Zheng, Y.; Cao, W.; Titov, A.; Hyvonen, J.; Manders, J. R.; Xue, J.; Holloway, P. H.; Qian, L. High-Efficiency Light-Emitting Devices Based on Quantum Dots with Tailored Nanostructures. *Nat. Photonics* **2015**, *9*, 1–9.

(130) Anikeeva, P. O.; Halpert, J. E.; Bawendi, M. G.; Bulović, V. Quantum Dot Light-Emitting Devices with Electroluminescence Tunable over the Entire Visible Spectrum. *Nano Lett.* **2009**, *9*, 2532–2536.

(131) Klimov, V.; Mikhailovsky, A.; Xu, S.; Malko, A.; Hollingsworth, J.; Leatherdale, C. A.; Eisler, H.; Bawendi, M. G. Optical Gain and Stimulated Emission in Nanocrystal Quantum Dots. *Science* **2000**, *290*, 314–317.

(132) Lee, K. H.; Lee, J. H.; Song, W. S.; Ko, H.; Lee, C.; Lee, J. H.; Yang, H. Highly Efficient, Color-Pure, Color-Stable Blue Quantum Dot Light-Emitting Devices. *ACS Nano* **2013**, *7*, 7295–7302.

(133) Wang, Y.; Leck, K. S.; Ta, V. D.; Chen, R.; Nalla, V.; Gao, Y.; He, T.; Demir, H. V.; Sun, H. Blue Liquid Lasers from Solution of CdZnS/ZnS Ternary Alloy Quantum Dots with Quasi-Continuous Pumping. *Adv. Mater.* **2015**, *27*, 169–175.

(134) Rayevska, O. E.; Grodzyuk, G. Y.; Dzhagan, V. M.; Stroyuk, O. L.; Kuchmiy, S. Y.; Plyusnin, V. F.; Grivin, V. P.; Valakh, M. Y. Synthesis and Characterization of White-Emitting CdS Quantum Dots Stabilized with Polyethylenimine. *J. Phys. Chem. C* **2010**, *114*, 22478–22486.

(135) Bao, J.; Bawendi, M. G. A Colloidal Quantum Dot Spectrometer. *Nature* **2015**, *523*, 67–70.

(136) Konstantatos, G.; Howard, I.; Fischer, A.; Hoogland, S.; Clifford, J.; Klem, E.; Levina, L.; Sargent, E. H. Ultrasensitive Solution-Cast Quantum Dot Photodetectors. *Nature* **2006**, *442*, 180–183.

(137) Clapp, A. R.; Medintz, I. L.; Mauro, J. M.; Fisher, B. R.; Bawendi, M. G.; Mattoussi, H. Fluorescence Resonance Energy Transfer Between Quantum Dot Donors and Dye-Labeled Protein Acceptors. *J. Am. Chem. Soc.* **2004**, *126*, 301–310.

(138) Chan, W. C. W.; Nie, S. Quantum Dot Bioconjugates for Ultrasensitive Nonisotopic Detection. *Science* **1998**, *281*, 2016–2018.

(139) Resch-Genger, U.; Grabolle, M.; Cavaliere-Jaricot, S.; Nitschke, R.; Nann, T. Quantum Dots versus Organic Dyes as Fluorescent Labels. *Nat. Methods* **2008**, *5*, 763–775.

(140) Meinardi, F.; McDaniel, H.; Carulli, F.; Colombo, A.; Velizhanin, K. a.; Makarov, N. S.; Simonutti, R.; Klimov, V. I.; Brovelli, S. Highly Efficient Large-Area Colourless Luminescent Solar Concentrators Using Heavy-Metal-Free Colloidal Quantum Dots. *Nat. Nanotechnol.* **2015**, *10*, 878–885.

(141) Nozik, A. J. Quantum Dot Solar Cells. *Physica E Low Dimens. Syst. Nanostruct.* **2002**, *14*,

115–120.

(142) Kamat, P. V. Quantum Dot Solar Cells. Semiconductor Nanocrystals as Light Harvesters†. *J. Phys. Chem. C* **2008**, *112*, 18737–18753.

(143) Chen, Q. Polymer Composites for Radiation Scintillation, 2012.

(144) Kishpaugh, D.; Hajagos, T. J.; Liu, C.; Chen, Q.; Pei, Q. Applications of Fluorene Moiety Materials to Improved Plastic Green Scintillators. Manuscript submitted.

(145) Brouwer, A. M. Standards for Photoluminescence Quantum Yield Measurements in Solution (IUPAC Technical Report). *Pure Appl. Chem.* **2011**, *83*, 2213–2228.

(146) Lakowicz, J. R. *Principles of Fluorescence Spectroscopy*; Springer: New York, 2006.

(147) *IUPAC Compendium of Chemical Terminology*; McNaught, A.; Wilkinson, A., Eds.; 2nd ed.; Blackwell Scientific Publications: Oxford, England, 1997.

(148) Swenberg, C. E.; Stacy, W. T. Influence of Resonance Transfer and Exciton Diffusion on Luminescence Decay. *Phys. Status Solidi* **1969**, *36*, 717–722.

(149) Hajagos, T. J.; Kishpaugh, D.; Pei, Q. Pulse Shape Discrimination Properties of Plastic Scintillators Incorporating a Rationally Designed Highly Soluble and Polymerizable Derivative of 9, 10-Diphenylanthracene. *Nucl. Instrum. Methods Phys. Res., Sect. A* **2016**, *825*, 40–50.

(150) Grodzicka, M.; Moszynski, M.; Szczesniak, T.; Kapusta, M.; Szawlowski, M.; Wolski, D. Energy Resolution of Scintillation Detectors with SiPM Light Readout. *IEEE Nucl. Sci. Symp. Conf. Rec.* **2010**, 1940–1948.

(151) Lee, K. H.; Lee, J. H.; Kang, H. D.; Han, C. Y.; Bae, S. M.; Lee, Y.; Hwang, J. Y.; Yang, H. Highly Fluorescence-Stable Blue CdZnS/ZnS Quantum Dots against Degradable Environmental Conditions. *J. Alloys Compd.* **2014**, *610*, 511–516.

(152) Dou, L.; Yang, Y. (Micheal); You, J.; Hong, Z.; Chang, W.-H.; Li, G.; Yang, Y. Solution-Processed Hybrid Perovskite Photodetectors with High Detectivity. *Nat. Commun.* **2014**, *5*, 5404.

(153) Tang, J.; Kemp, K. W.; Hoogland, S.; Jeong, K. S.; Liu, H.; Levina, L.; Furukawa, M.; Wang, X.; Debnath, R.; Cha, D.; *et al.* Colloidal-Quantum-Dot Photovoltaics Using Atomic-Ligand Passivation. *Nat. Mater.* **2011**, *10*, 765–771.

(154) Gong, X.; Yang, Z.; Walters, G.; Comin, R.; Ning, Z.; Beauregard, E.; Adinolfi, V.; Voznyy, O.; Sargent, E. H. Highly Efficient Quantum Dot near-Infrared Light-Emitting Diodes. *Nat. Photonics* **2016**, *10*, 253–257.

(155) Tan, Z.-K.; Moghaddam, R. S.; Lai, M. L.; Docampo, P.; Higler, R.; Deschler, F.; Price, M.; Sadhanala, A.; Pazos, L. M.; Credgington, D.; *et al.* Bright Light-Emitting Diodes Based on Organometal Halide Perovskite. *Nat. Nanotechnol.* **2014**, *9*, 687–692.

(156) Buzhan, P.; Dolgoshein, B.; Filatov, L.; Ilyin, A.; Kantzerov, V.; Kaplin, V.; Karakash, A.; Kayumov, F.; Klemin, S.; Popova, E.; *et al.* Silicon Photomultiplier and Its Possible Applications. *Nucl. Instrum. Methods Phys. Res., Sect. A* **2003**, *504*, 48–52.

(157) Dolgoshein, B.; Balagura, V.; Buzhan, P.; Danilov, M.; Filatov, L.; Garutti, E.; Groll, M.; Ilyin, A.; Kantserov, V.; Kaplin, V.; *et al.* Status Report on Silicon Photomultiplier Development and Its Applications. *Nucl. Instrum. Methods Phys. Res., Sect. A* **2006**, *563*, 368–376.

(158) Frach, T.; Prescher, G.; Degenhardt, C.; de Gruyter, R.; Schmitz, A.; Ballizany, R. The Digital Silicon Photomultiplier; Principle of Operation and Intrinsic Detector Performance. In *2009 IEEE Nuclear Science Symposium Conference Record (NSS/MIC)*; IEEE, 2009; pp. 1959–1965.

(159) Lee, N.; Choi, S. H.; Hyeon, T. Nano-Sized CT Contrast Agents. *Adv. Mater.* **2013**, *25*, 2641–2660.

(160) Liu, Y.; Ai, K.; Lu, L. Nanoparticulate X-Ray Computed Tomography Contrast Agents: From Design Validation to in Vivo Applications. *Acc. Chem. Res.* **2012**, *45*, 1817–1827.